Theoretical Study on Electron States Floating in Internal Space of Condensed Matter Based on First-Principle Calculations

Yu-ichiro Matsushita

Abstract

We report first-principles electronic-structure calculations that clarify the floating nature of electron states in covalent semiconductors. It is found that wave functions of several conduction- and valence-band states, including the conduction-band minima, do not distribute near atomic sites, as was taken for granted, but *float* in interstitial channels in most semiconductors. The floating states have a nearly-free-electron(NFE)-like character, and extend in the channels broadly without atomic-orbital characters. The electrostatic potential at the channels and the directions and shapes of the interstitial channels depend on the crystal symmetry so that mysterious variation of the energy gaps in silicon carbide (SiC) polytypes is naturally explained by considering the floating nature. In addition, we have found that the floating states are closely related to the anisotropy in effective masses in SiC.

It has been found that most conduction-band minima have floating nature. The existence of the floating state comes from the internal space in the crystal structures, and non-spherical charge distribution.

The substantial band-gap variation in SiC has been analyzed by an empirical parameter "hexagonality" for a half century. Yet, we have clarified that the parameter "hexagonality" is a misleading parameter. Instead, we have found that a new parameter "channel length", which represents the spatial extension of the floating state, is essential in describing the band-gap variation in SiC.

In addition, we have performed the linear-combination-of-atomic-orbitals (LCAO) calculations and compared the results with those calculated by the plane-wave-basis set. It is found that the floating characters in the electron states are difficult to be pursued in the LCAO calculations. We have also examined the floating states in pressurized sp^3-bonded materials.

We have also found that the energy bands with floating character manifest different behavior from other bands with atomic-orbital character under the pressurized circumstances.

Acknowledgements

I would like to express my sincere gratitude to Professor Atsushi Oshiyama for continual guidance, encouragement and supervising the present thesis patiently. I am pleased to acknowledge useful discussions with Professor Kenji Shiraishi, Dr. Katsumasa Kamiya, Dr. Yoshitaka Fujimoto, and Dr. Yoshihiro Gohda. Thanks are extended to Dr. Tetsuo Hatakeyama for fruitful discussion and showing experimental data. I am also pleased to acknowledge for enjoying my school life with Professor Jun-ichi Iwata, Dr. Kazuyuki Uchida, Dr. Shinnosuke Furuya, Dr. Kenichi Koizumi, Dr. Zhixin Guo, Dr. Keisuke Sawada, Mr. Mitsuru Nishikawa, Mr. Shinya Kyogoku, Mr. Yoshihide Yoshimura, Mr. Shota Suda, Mr. Sho Hirota, Mr. Batnyam Enkhtaivan, Mr. Yuuki Sugihara, Mr. Shota Hagino, and Miss. Sayoko Shimizu. Thanks are extended to all the members of group of Professor Masatoshi Imada, Professor Naoto Nagaosa, Professor Nobuyasu Itoh, Professor Yukitoshi Motome, Professor Ryotaro Arita, and Professor Synge Todo for great research life.

Last but not least, I wish to thank my parents and old friends for many years of encouragements.

Contents

1

Introduction

1.1 Limitation of the Si-based technology

One of the most prominent fields developed in the 20th century is undoubtedly electronics. Electronics is widely exploited in information processing, telecommunications, computers and power supply. Electronics has made our lives happier and richer. Electronics becomes essential part of our lives, and is continuing to have great effects on human society in the future. The progress of the electronics has been mostly attributable to the electrical engineering based on silicon semiconductors. Silicon is today, and will be the dominant material in the semiconductor industry; Si is a material with properties suited to a wide range of applications. Silicon is abundant, and large high-quality (>99.9%) single crystals can be produced at an economical cost. In addition, silicon electronic devices withstand the high temperatures and electrical powers without becoming dysfunctional due to avalanche breakdown. In fact, silicon devices work well even at around 100 °C. These prominent properties make silicon the core of modern electronic devices.

Yet, Si is never an all-round material. With the development of the electronics, electronic devices have been widely used in various places, e.g., electrical power plant, transformer station, automobile, and rocket. Under the circumstances, requests for electronics become more multifaceted: e.g., in some places more high-power device, or high frequency device are demanded, and tough device under severe environments (e.g., higher temperature up to hundreds degrees Celsius, and radiological threat) in other places. Such requirements come not only from industries, but also from the

society. Now, modern society faces a lot of urgent issues, related to geoenvironmental and energy problem. There has been great expectations for electronics to overcome the problems. The responsibility of the electronics is continuing to increase in the future. Si devices are soon reaching its performance limits. Within the Si technology, drastic development can not be expected.

1.2 SiC: A promising material

Silicon carbide (SiC) is a promising material for high-power, high-temperature, and high-frequency electronic devices. Although its outstanding technologically potential has been recognized for several decades, the applications have been greatly hindered by problems related to bulk crystal growth. SiC is not a material normally found in nature. The earliest reported production of the silicon carbide is by Acheson in 1891. SiC is one of the oldest semiconductors. The SiC crystal which is made by Acheson method still contains a lot of impurities, and is difficult for practical applications as a semiconductor. The first growth of high pure SiC crystal has been reported by Lely in 1955. Various properties of the SiC have been studied in the 1960s, and has attracted great attention from semiconductor researchers due to its outstanding thermal stability. There are further several breakthroughs, e.g., improved Lely method by Tairov (1), step-controlled epitaxial method by Matsunami (2, 3), and repeated A-face growth (RAF) method (4). SiC bulk crystal growth technology has recently achieved drastic improvement and enabled the growth of large high-quality single crystals.

SiC is a sp^3-bonded covalent-semiconductor material with a wide band gap. The bond length is 0.189 nm, which is a value intermediate between that of silicon, 0.235 nm, and of diamond, 0.154 nm. The cohesive energy of Si-C is 12.58 eV per pair of atoms, much bigger than that in silicon bulk, 9.28 eV (5). Therefore, SiC is a hard material next to the diamond. These marvelous properties provide a clear path to high efficient power-electronics (3). The wide band gap enables SiC to show very high breakdown fields and also high current densities, about ten times higher than that of Si or GaAs (6) (See Table. 1.1). The large saturation velocity, more than 2 times of Si bulk, makes SiC high power device at high frequencies. The energies of optical phonons in SiC are as high as 100-120 meV (7), which leads to a high saturated electron drift velocity (8) and high thermal conductivity (9). The smaller on-resistance and faster switching of

Table 1.1: Comparison of physical properties among SiC (4*H*-SiC), Si, GaAs, GaN, and diamond.

properties	4*H*-SiC	Si	GaAs	GaN	diamond
Band gap (eV)	3.26	1.12	1.42	3.42	5.47
Mobility (cm^2/Vs)	1000	1350	8500	1500	2000
Breakdown field (MV/cm)	2.8	0.3	0.4	3	8
Saturation Drift (cm/s)	2.2×10^7	1.0×10^7	1.0×10^7	2.4×10^7	2.5×10^7
Thermal conductivity (W/cmK)	4.9	1.5	0.46	1.3	20

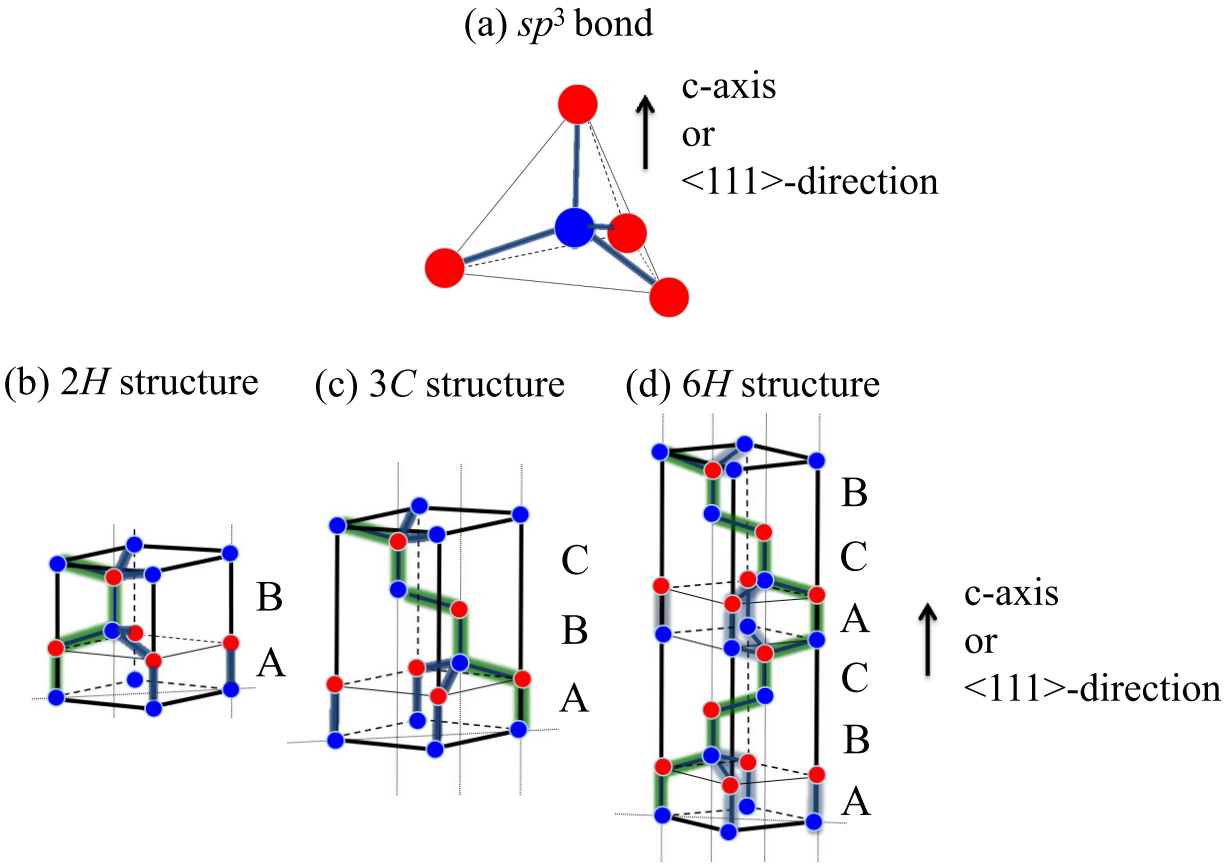

Figure 1.1: Sketches for the sp^3-bond unit (a), the unit cell for the $2H$-SiC (b), for the $3C$-SiC (c), and for the $6H$-SiC (d). In the figures, the blue and the red balls depict Si, and C atoms, respectively. Each stacking sequence is also specified.

SiC helps to minimize energy loss and heat generation, and further its higher thermal conductivity enables more efficient removal of waste heat energy from the active device. Because heat energy radiation efficiency increases greatly with increasing temperature difference between the device and the cooling ambient, the ability of SiC to operate at high junction temperatures permits much more efficient cooling to take place, so that heat sinks and other device-cooling hardware (i.e., fan cooling, liquid cooling, air conditioning, heat radiators, etc.) typically needed to keep high-power devices from overheating can be made much smaller or even eliminated. Due to the strong chemical stability of SiC, the operation temperature of SiC is expected to increase up to around 600 °C. Compared with that of Si bulk, 120 °C, it is a prominent advantage for automotive industries and in aerospace, for example.

From a crystallographic point of view, SiC is the most famous material for showing polytypes. SiC exists in hundreds of different structures called polytypes (10). The polytypes of SiC makes it difficult to grow single-phase material. The selective crystal growth of SiC has been under intense studies(3, 11, 12, 13, 14, 15). In sp^3-bonded covalent semiconductors, each atom is bonded with its four nearest neighbor atoms [See Fig. 1.1(a)]. The zincblende and the diamond structures with cubic symmetry and the wurtzite structure with hexagonal symmetry are the typical two examples. When tetrahedron units [Fig. 1.1(a)] are piled next to one another along the $\langle 111 \rangle$ direction or c-axis, the crystal stricture looks alternating layers of three bonds (bilayer) and one bond (vertical bond). A simple way to discriminate different polytypes is to use a silicon-carbon bilayer by a new building unit, and label each crystal structure as its stacking sequence. The zincblende structure is represented by the stacking sequence of ABC and the wurtzite by AB. The stacking sequence is not limited to the above two cases. Hence there are dozens of polytypes labeled by the periodicity of the stacking sequence n and the symmetry (cubic or hexagonal) such as $2H$ (wurtzite), $3C$ (zinblende), $4H$, and $6H$ [Fig. 1.1(b-d)].

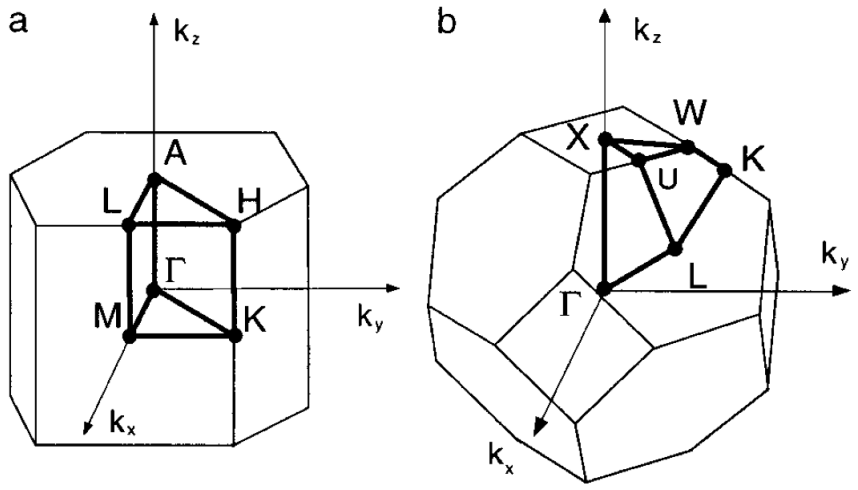

Figure 1.2: Brillouin zones of a) hexagonal and b) face-centered cubic lattice. (Ref. (16))

As for the energy-band structures, it is known that SiC is a semiconductor. Fig. 1.2 shows the first Brilloiun Zones for the cubic and hexagonal structures. Fig. 1.3 shows

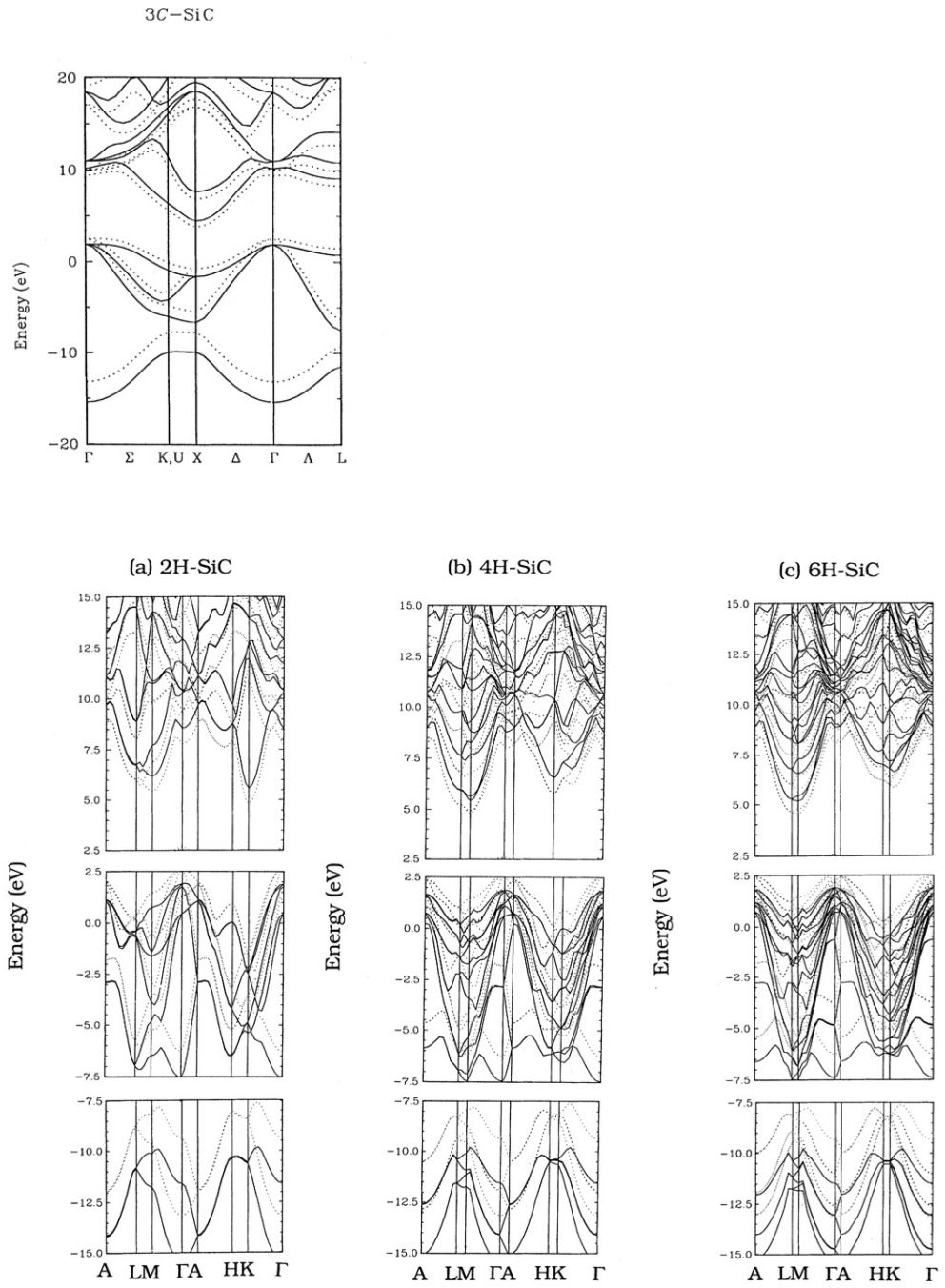

Figure 1.3: The band structure for the $3C$-SiC (upper panel), for the $2H$-SiC (b), for the $4H$-SiC (c), and for the $6H$-SiC (d) within the DFT-LDA (See Sec. 2.4.1) (dotted lines) and after inclusion of quasi-particle (QP) corrections (Solid lines). The band gaps are estimated to be 1.30eV by the LDA, and 2.60 eV by the QP for the $3C$, 2.13 eV by the LDA, and 3.65 eV by the QP for the $2H$, 2.19 eV by the LDA, and 3.54 eV by the QP for the $4H$, and 1.98 eV by the LDA, and 3.24 eV by the QP for the $6H$. (Ref. (17))

Table 1.2: Comparison of physical properties in SiC polytypes.

Properties	2H-SiC	3C-SiC	4H-SiC	6H-SiC
Stacking sequence	AB	ABC	ABCB	ABCACB
Lattice constants (Å)	a=3.09 c=10.08	4.36	a=3.09 c=10.08	a=3.09 c=15.12
Band gap (eV)	3.33	2.23	3.26	3.02
Thermal conductivity (W/cmK)		4.9	4.9	4.9
Mobility (Ref. (18))			$\mu_{[11\bar{2}0]}/\mu_{[0001]}$: 0.83	$\mu_{[0001]}/\mu_{[1\bar{1}00]}$: 6.2
Effective mass (Ref. (16))		$m_{\|\|X-\Gamma}$: 0.67 $m_{\perp X-\Gamma}$: 0.22 − 0.25	$m_{M-\Gamma}$: 0.30 − 0.58 m_{M-L} : 0.33 − 0.48	$m_{M-\Gamma}$: 0.24 − 0.42 m_{M-L} : .1.7 − 2.0

the band structures of the 3C-, 2H-, 4H-, and 6H-SiC resulted from the density-functional-theory (DFT) (See Sec. 2.3), and after inclusion of quasi-particle self-energy correction, called GW method (17). All available calculations and experiments show that the tops of the valence bands for all the four polytypes of SiC considered here are at the center of the Brillouin Zone (Γ-point), while the minima of the conduction bands are located off center. These semiconductors have indirect band gaps. The values for the band gaps: 3.33 eV for the 2H, 3.25 eV for the 4H, 3.023 eV for the 6H, 2.461 eV for the 3C, were experimentally determined (19, 20, 21) [Table. 1.2]. It is remarkable that the band gap varies by about 40 % in spite that the local atomic structures are identical to each other. The currently accepted locations of the conduction band minima are at X-point for the 3C, K-point for the 2H, M-point for the 4H, and between M- and L-point for the 6H [Fig. 1.3]. Although it is difficult to measure these minima directly in experiments, these assignments are consistent with the band calculations.

As for the band-gap variation, Choyke argued in his pioneering works that the band-gap variation is understood by the analyses using an empirical parameter "hexagonality" a half century ago. A bilayer sandwiched by the two same stacking indexes is called a hexagonal layer (h), and the other is a cubic layer (k). The parameter "hexagonality" is the percentage of the hexagonal layers in the stacking sequence of the unit

cell (21). Therefore, the hexagonality in the $3C$ structure is 0%, and that in the $2H$ is 100%. Thus the parameter "hexagonality" represents how the stacking sequence is different from that of the cubic stacking. The band-gap variation has been argued to be linear with the hexagonality. Yet, the relations between band-gap variation and the hexagonality have not been validated from underlying physics. In addition, it is noteworthy that the linear relation has been examined for only seven polytypes. In order to examine the validity of the parameter, more samplings are certainly needed. The understanding of the electronic properties would be quite limited and inadequate only in the empirical discussion.

The conduction band structures as a function of the wave vector $\mathbf{k}_i$ along a specified direction i near a conduction-band minimum $\mathbf{k}_{\min}$ can be approximated by a quadratic form

$$E(\mathbf{k}_i) = E_0 + \frac{\hbar^2(\mathbf{k}_i - \mathbf{k}_{\min})^2}{2m^*}, \tag{1.1}$$

where E_0 is the band energy at the conduction-band minimum, and m^* is the effective mass along that direction. The effective masses at the conduction-band minima have been also studied. Experimentally, the effective mass is measured by means of Hall mobility measurement (22, 23, 24, 25), infrared Faraday rotation measurement (26), photoluminescence (27), cyclotron resonance (28, 29), infrared absorption spectrum (30, 31). These measurements reveals that the effective mass in the $6H$-SiC exhibits quite large anisotropy [Table 1.2]: the effective mass along the c-axis is 6.2 times larger than that in the plane perpendicular to the c-axis. On the other hand, particularly the optically detected cyclotron resonance measurements have also been performed for $3C$- and $4H$-SiC to find no such anisotropy of effective mass [Table. 1.2]. The reason for the anisotropy is still unclear. In addition, the studies for the anisotropy in effective mass of hole is limited, and the values are different to each other.

1.3 Atomic-orbital character and nearly-free-electron (NFE) state in condensed matter

Atoms comprise condensed matter in which electron states generally have their own atomic-orbital character and produce various physical and chemical properties. Therefore, our understanding of condensed matter has been based on atomic orbital picture.

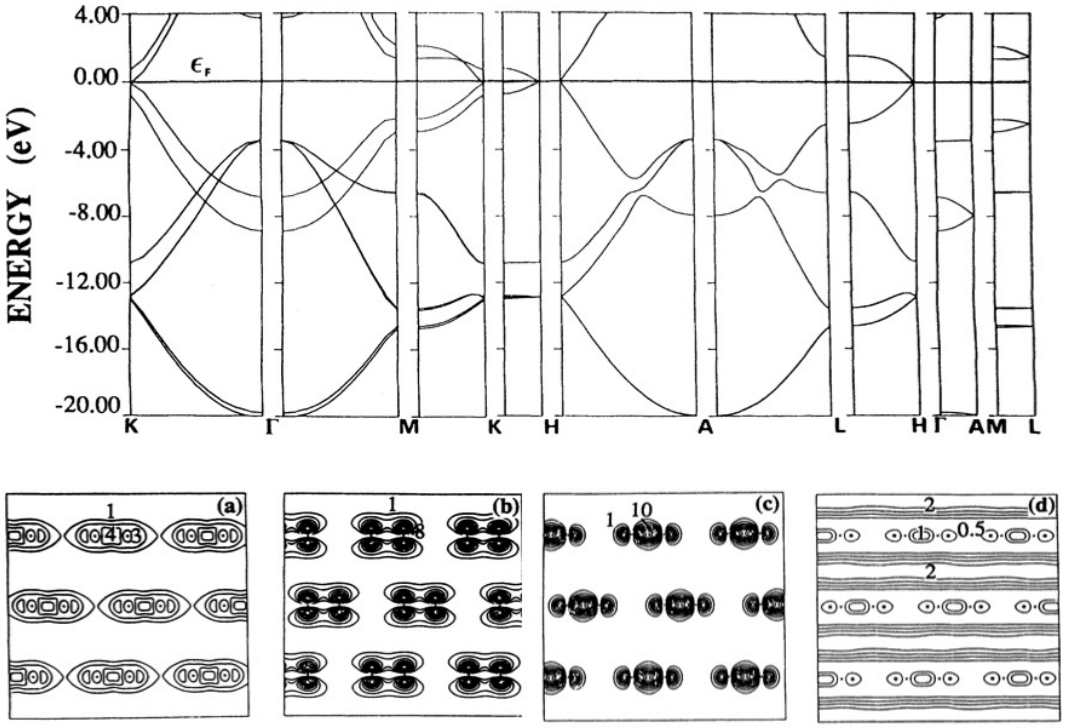

Figure 1.4: Upper panel: Ab-initio band structure of graphite along different lines in Brillouin Zone. Lower panels: Charge-density distributions of some typical wave functions at the Γ point of the Brillouin Zone: (a) second band, (b) fourth band, (c) eighth band, and (d) ninth band. The ninth orbital (d) distributes not near atomic sites, but extends in interlayer space broadly with nearly-free-electron (NFE) character. All these density are presented in electron/unit cell. (Ref. (32))

The set of atomic orbitals, however, does *not* constitute a complete set to describe electron states in condensed matter, even if we sum up the high-energy-atomic orbitals. This mathematical fact raises an interesting question: whether electron stases without atomic-orbital characters exist in usual condensed matter? The answer comes to be known partially. Some examples have been discovered in spacious matter. Interlayer states in graphite (33) or intra- and inter-tube states in carbon nanotubes (34) are such examples, where the corresponding wave functions distribute not near atomic sites but in internal space, thus, *floating* in matter (See Fig. 1.4). These floating states are usually unoccupied but appear near Fermi levels or fundamental energy gaps and play crucial roles in excitation spectra (35, 36) and ground-state properties (37), including occurrence of superconductivity (38, 39).

It has been recognized that there is no room to allow such floating states in usual condensed matter. However, we have found in this thesis that certain electron states of the conduction- and valence-bands in covalent semiconductors ranging from silicon to III-V compounds float in internal channels. Shapes of floating electron clouds depend on symmetry of the crystal and explain drastic and mysterious variation of the energy gaps and the effective masses in several polytypes of compound semiconductors.

1.4 Our aim

As mentioned above in Sec. 1.2, the most mysterious and interesting characteristics in SiC is that SiC exhibits various properties depending on the polytypes in spite of their structural similarity. In this thesis, we focus on mainly two material properties: substantial band-gap variation in polytypes, and anisotropy in effective mass. We have performed theoretical calculations based on the density-functional-theory (DFT) (40, 41) to answer the following issues. First our purpose is to clarify the mechanism of the substantial band-gap variation in SiC, and whether the mysterious band-gap variation is common to other sp^3-bonded materials: e.g., Si, diamond, AlN, BN, GaN. Second our aim is to clarify the mechanism of the anisotropy in effective mass of electrons in SiC, and investigate whether the effective mass of holes exhibits anisotropy or not.

1.5 Organization of the present thesis

In Chapter 2, we first describe the density -functional theory (DFT), which is a powerful method to obtain the total energies and the electronic structures of real materials. This chapter introduces the Born-Oppenheimer approximation, the fundamental theorem of the DFT, the generalized gradient approximation (GGA), and pseudopotential method, which we have adopted in this study. Though the GGA in the DFT has shown a fantastic ability to understand and even predict material properties, the energy gaps are underestimated substantially as is characteristic of GGA. We refer to the problem in this chapter.

We show the calculated results to clarify the substantial band-gap variation in SiC polytypes in Chapter 3. We have first determined the structural parameters, such as lattice constants and total energies for each polytype of the six materials. The calculated electronic band structures are also presented. Next, we are devoted to our finding, which is the most important point in this thesis, that peculiar electron states with nearly-free-electron (NFE)-like character, which we call floating state, are ubiquitous in most sp^3-bonded materials. The floating states distribute not near atomic sites, but extend in internal space, called channels. We have succeeded to explain the mechanism of substantial band-gap variation naturally by considering the floating state. We have also investigated the capability of the LCAO calculations in describing the floating nature in this chapter.

We discuss why the energy level of floating state is lower than the vacuum level in Chapter 4. We have found that non-spherical electron distribution plays important roles in lowering the energy level of the floating state substantially. In addition, We have also found that the energy bands with floating character manifest different behavior from other bands with atomic-orbital character under the pressurized circumstances.

Chapter 5 is devoted to show that a new parameter channel length, which represents the spatial extension of the floating state, is an essential parameter in describing the band-gap variation. We have also found that the anisotropy in effective mass of electrons is closely related to the shapes of the channels.

Chapter 6 presents that the spontaneous polarization induced by the hexagonal layers makes hole localized at the interface between the channel region and the hexagonal stacking region, thus showing anisotropy in effective mass of hole. We have also

investigated the spontaneous polarization effects on the band gap.

2

Density Functional Theory (DFT)

First-principles calculations are the theoretical method to treat the quantum many-body system based on the principles of the quantum theory. The final goal of the condensed matter physics is to solve the quantum many-body problem. Its Hamiltonian is as follows in the CGS units:

$$\hat{H} = T_e + T_n + U, \text{ and } U = U_{ee} + U_{en} + U_{nn}, \tag{2.1}$$

where

$$\begin{aligned} T_e = \sum_i \frac{p_i^2}{2m},\ T_n = \sum_I \frac{P_I^2}{2M_I},\ U_{ee} = \frac{1}{2}\sum_{i\neq j} \frac{e^2}{|\mathbf{r}_i - \mathbf{r}_j|}, \\ U_{nn} = \frac{1}{2}\sum_{I\neq J} \frac{Z^2e^2}{|\mathbf{R}_I - \mathbf{R}_J|},\ U_{en} = -\frac{1}{2}\sum_{i,I} \frac{Ze^2}{|\mathbf{r}_i - \mathbf{R}_I|}, \end{aligned} \tag{2.2}$$

where the m, M_I, Z, p_i, P_I, $\mathbf{r}_i$, and $\mathbf{R}_I$ represent the mass of an electron, the mass of a nucleus, the atomic number, the momentum of the electron, the momentum of the nucleus, the position of the electron, and the position of the nucleus, respectively.

2.1 Frozen-phonon approximation

Condensed matter is composed of tremendous number of nuclei and electrons, and they are interacting with each other. Therefore, to know all their behaviors is quite difficult or impossible. Yet, by utilizing the fact that the mass of a nucleus is much heavier than

that of electrons, it is known that an efficient approximation, called frozen phonon approximation, is applicable to the system. To solve the Hamiltonian, consider an extreme case where the mass of the nucleus is infinite. In this situation, it is found that the kinetic energy of the nucleus is negligible, and nuclei are fixed at a configuration $\{\mathbf{R}_I\}$. The Hamiltonian is much simpler than the previous one, because the nuclei coordinate $\{\mathbf{R}_I\}$ are regarded as just parameters. As long as this approximation is applicable, we can separate the degree of freedom of the electrons from that of nuclei. The Schrödinger equation to solve becomes,

$$[T_e + U_{\mathbf{R}}(\mathbf{r})]\psi_{\mathbf{R}}(\mathbf{r}) = \epsilon_{\mathbf{R}}\psi_{\mathbf{R}}(\mathbf{r}), \tag{2.3}$$

and

$$U_{\mathbf{R}}(\mathbf{r}) = U_{ee} + U_{en} + U_{nn}, \tag{2.4}$$

where $\mathbf{r}$ ($\mathbf{R}$) represents a set of positions of the electrons (nuclei). In the equations, atomic configuration $\{\mathbf{R}_I\}$ are fixed, and the subscript $\mathbf{R}$ in the potential $U_{\mathbf{R}}$ means this explicitly. Remark that the variables $\{\mathbf{R}\}$ are not quantum operators, but just parameters.

Above case is an extreme situation. In real systems, the mass of the nucleus is much larger than that of electron, but it is not infinite. We should estimate the error in neglecting the kinetic energy of the nuclei. The electrostatic potential for electrons from nuclei is the sum of the potential from each nucleus. The potential from each nucleus depends on the distance from the nucleus. Therefore, we rewrite the wave function $\Psi_0(\{\mathbf{r}_i\}, \{\mathbf{R}_I\})$ to $\Psi_0(\mathbf{r}_i - \mathbf{R}_I)$. Therefore, the expectation values of the $\nabla^2_{\mathbf{R}}$ and $\nabla^2_{\mathbf{r}}$ yields the same value, and the kinetic energy of the nuclei is smaller than that of electrons by the order $m/M \approx 10^{-3}$. The neglected term in Eq. (2.3) is still found to be small with an error of 10^{-3}.

2.2 Schrödinger-Ritz variational principles

In this section, we derive a variational formalism of the Schrödinger equation for the ground state. Let E_0, $\Psi_0(\{\mathbf{r}_i\}, \{\mathbf{R}_I\})$ be an energy and the wave function of the ground state of the considered Hamiltonian $\hat{H}$.

$$\hat{H}\Psi_0(\{\mathbf{r}_i\}, \{\mathbf{R}_I\}) = E_0\Psi_0(\{\mathbf{r}_i\}, \{\mathbf{R}_I\}). \tag{2.5}$$

Define an energy functional of a wave function as follow:

$$E[\Psi] \equiv \frac{\langle \Psi | H | \Psi \rangle}{\langle \Psi | \Psi \rangle}. \tag{2.6}$$

The energy functional yields the ground state energy when $\Psi = \Psi_0$, and increases for any variation of the wave function from Ψ_0:

$$E[\Psi] \geq E_0. \tag{2.7}$$

That is, we can derive a variational formalism of the Schrödinger equation for the ground state with respect to the wave function:

$$E_0 = \mathrm{Min}_{\Psi} E[\Psi]. \tag{2.8}$$

Yet, remark that we must vary the wave function in the restrictions of antisymmetric relations. If not, the energy functional gives lower energy than the ground state energy.

2.3 Density functional theory (DFT)

From the above sections, we focus on solving the simpler Hamiltonian, Eq. (2.3), with the nuclei being fixed at some configuration. The simpler Hamiltonian, however, is still quite difficult to solve, because the number of the concerned electrons is Avogadro constant, $\approx 10^{23}$. The huge number of electrons are interacting with each other. In addition, we must take account of the statistics of Fermions. Some efficient approximations, and methods to solve the Schrödinger equation are known. One of the most famous approximations without any experimental values is the density functional theory (DFT) (40, 41), which we have adopted in this study.

Professor Walter Kohn was awarded, with professor John Pople, the Nobel Prize in chemistry in 1998 for his creative studies, that is the formulation of the DFT. His outstanding works start from a simple question: Is it possible to reconstruct quantum theory, based on the density, not the wave function. The idea is very ambitious because the density is a function of the 3-dimensional spacious coordinates, while the wave function is that of the $3N$-dimensional coordinates, where the variable N represents the number of electrons. He has succeeded to verify his hypothesis, thus, gives powerful tool for theoretical calculations in condensed matter physics, and quantum chemistry. In this section, we review the basic idea of the DFT.

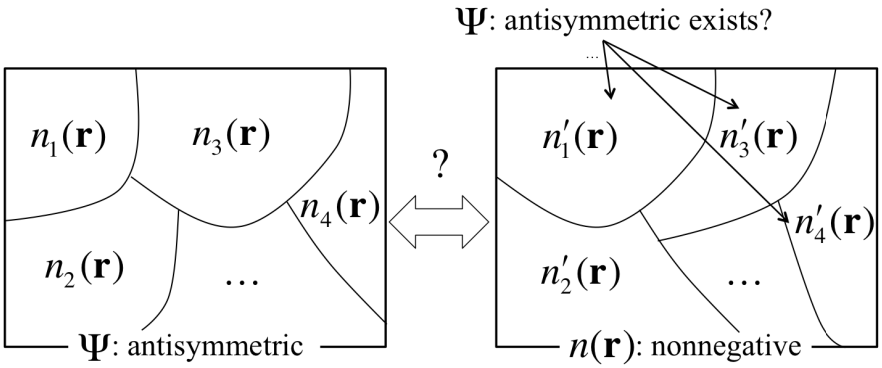

Figure 2.1: The figures show the variational space with respect to the wave function (left) and electron density (right). The equivalence between these two space is non-trivial.

2.3.1 Hohenberg-Kohn theorem and n-representability

In this section, we derive the Hohenberg-Kohn theorem. We can rewrite the Eq. (2.8) as follows:

$$\begin{aligned}
E_0 &= \mathrm{Min}_{\Psi} \langle \Psi | H | \Psi \rangle \\
&= \mathrm{Min}_{\Psi} \langle \Psi | T_e + U_{ee} + U_{en} | \Psi \rangle \\
&= \mathrm{Min}_{\Psi} \{ \langle \Psi | T_e + U_{ee} | \Psi \rangle + \langle \Psi | U_{en} | \Psi \rangle \} \\
&= \mathrm{Min}_{n(\mathbf{r})} \left[\mathrm{Min}_{\{\Psi \text{ which gives } n(\mathbf{r})\}} \{ \langle \Psi | T_e + U_{ee} | \Psi \rangle + \langle \Psi | U_{en} | \Psi \rangle \} \right] \\
&= \mathrm{Min}_{n(\mathbf{r})} \left[\mathrm{Min}_{\{\Psi \text{ which gives } n(\mathbf{r})\}} \{ \langle \Psi | T_e + U_{ee} | \Psi \rangle \} + \int V_{\mathrm{ext}}(\mathbf{r}) n(\mathbf{r}) d\mathbf{r} \right] \\
&\equiv \mathrm{Min}_{n(\mathbf{r})} \left[F[n(\mathbf{r})] + \int V_{\mathrm{ext}}(\mathbf{r}) n(\mathbf{r}) d\mathbf{r} \right], \qquad (2.9)
\end{aligned}$$

where the $F[n(\mathbf{r})]$ is a universal functional, which does not depend on the external potential V_{ext}, e.g., atom positions nor atom species. On the last line, we define the $F[n(\mathbf{r})]$ as $\mathrm{Min}_{\{\Psi \text{ which gives } n(\mathbf{r})\}} \{ \langle \Psi | T_e + U_{ee} | \Psi \rangle \}$. Once the $F[n(\mathbf{r})]$ is obtained, $E^{\mathrm{tot}}_{\mathrm{ground}}[n(\mathbf{r})]$ of the system we are interested in is obtained by variation with respect to electron density $n(\mathbf{r})$. However, there are two important problems: one is that the variational space of the electron density $n(\mathbf{r})$ on the fourth line of the Eq. (2.9), and the other is that the exact form of $F[n(\mathbf{r})]$ is unknown. The latter is discussed in Sec.2.4 in more detail.

The former problem is, in other words, whether the variation, Min_{Ψ}, is equal to the two-step variation, $\mathrm{Min}_{n(\mathbf{r})}\mathrm{Min}_{\{\Psi \text{ which gives } n(\mathbf{r})\}}$ [See fig.2.1]? To prove the equivalence, we rewrite the variation Min_{Ψ} as follow:

$$\mathrm{Min}_{\Psi} = \mathrm{Min}_{\{n(\mathbf{r})|\text{ corresponding } \Psi \text{ exists}\}}\mathrm{Min}_{\{\Psi \text{ which gives } n(\mathbf{r})\}} \tag{2.10}$$

There is evidence that, for any nonnegative density $n(\mathbf{r})$, antisymmetric orbitals whose squared norm yields the density exists (n-representability) (42, 43). Therefore, $\mathrm{Min}_{\{n(\mathbf{r})|\text{ corresponding } \Psi \text{ exists}\}} = \mathrm{Min}_{\{n(\mathbf{r})\}}$, thus the Eq.(2.9) is proved.

2.3.2 Kohn-Sham equaion

Above, we have mentioned the mind of the DFT. In this section, we show a practical procedure of DFT calculations. By assuming that the electron density is expanded by Kohn-Sham (one-electron) orbitals $\phi_i(\mathbf{r})$, it is written as

$$n(\mathbf{r}) = \sum_{i \leq \epsilon_F} |\phi_i(\mathbf{r})|^2, \tag{2.11}$$

where the ϵ_F represents the Fermi energy. Here, we divide the universal functional, $F[n(\mathbf{r})]$, to three parts as follows:

$$F[n(\mathbf{r})] \equiv T_s[n(\mathbf{r})] + \frac{e^2}{2}\int\int \frac{n(\mathbf{r})n(\mathbf{r}')}{|\mathbf{r}-\mathbf{r}'|}d\mathbf{r}d\mathbf{r}' + E_{\mathrm{xc}}[n(\mathbf{r})], \tag{2.12}$$

where $T_s[n(\mathbf{r})]$ represents the kinetic energy of the non-interacting virtual system yielding the electron density $n(\mathbf{r})$, the second term represents the electron-electron Coulomb energy, and the third term is called the exchange-correlation energy representing all the other quantum many-body energies. With these preparations, we determine the Kohn-Sham orbitals variationally to give the minimum total energy with the Lagrange multipliers. Then, a series of equations, called Kohn-Sham equation, are derived:

$$\{-\frac{1}{2}\nabla^2 + V_{\mathrm{eff}}(\mathbf{r})\}\phi_i(\mathbf{r}) = \epsilon_i\phi_i(\mathbf{r}) \tag{2.13}$$

$$n(\mathbf{r}) = \sum_{i \leq \epsilon_F} |\phi_i(\mathbf{r})|^2 \tag{2.14}$$

$$V_{\mathrm{eff}}(\mathbf{r}) = V_{\mathrm{ext}}(\mathbf{r}) + V_{\mathrm{Hartree}}(\mathbf{r}) + V_{\mathrm{xc}}(\mathbf{r}) \tag{2.15}$$

where V_{ext}, V_{Hartree}, and V_{xc} are the potential energy from the nuclei, the potential energy from the electron-electron Hartree Coulomb repulsion, and the exchange-correlation potential derived from the exchange-correlation energy. ϵ_i is the Lagrange

multiplier. Therefore, a many-body problem is mapped to a one-body problem with an effective potential $V_{\text{eff}}(\mathbf{r})$ in which the quantum many-body effects are incorporated in the exchange-correlation potential:

$$V_{\text{xc}}(\mathbf{r}) \equiv \frac{\delta E_{\text{xc}}[n(\mathbf{r})]}{\delta n(\mathbf{r})}. \tag{2.16}$$

Remark that the effective potential in the Kohn-Sham equation depends on the electron density or the Kohn-Sham orbitals. Therefore, we have to solve the Kohn-Sham equation self-consistently. In the practical application of the DFT, the procedure is represented in the Fig. 2.2. We solve the Kohn-Sham equation until the input effective potential accords with the updated potential.

2.4 Approximations for exchange-correlation energy, E_{xc}

2.4.1 Local-density approximation (LDA)

As mentioned above, we have transformed the many-body-interacting problem to a simple one-body problem, called Kohn-Sham equation. However, we neither know the exact functional of the $E_{\text{xc}}[n]$, nor $V_{\text{xc}}[n(\mathbf{r})]$. Furthermore, the DFT scheme does not provide a recipe for the $E_{\text{xc}}[n]$ and $V_{\text{xc}}[n(\mathbf{r})]$, thus we need some approximation for them. We introduce a drastic approximation, called the local-density approximation (LDA) (44), such as

$$E_{\text{xc}} = \int \epsilon_{\text{xc}}^{\text{unif}}(n(\mathbf{r}))n(\mathbf{r})d\mathbf{r}, \tag{2.17}$$

where the $\epsilon_{\text{xc}}^{\text{unif}}(n)$ is the exchange-correlation energy per electron of the uniform electron gas with electron density n. If the spatial gradient of the electron density is small, the approximation is expected to be justified. In fact, it is shown that the approximation is justified in

$$\{\frac{\nabla n(\mathbf{r})}{6k_F(\mathbf{r})n(\mathbf{r})}\} \ll 1 \tag{2.18}$$

(45). Therefore, the exchange-correlation potential V_{xc}(r) is derived as follow:

$$V_{\text{xc}}(\mathbf{r}) = \epsilon_{\text{xc}}^{\text{unif}}(n(\mathbf{r})) + n(\mathbf{r})\frac{d\epsilon_{\text{xc}}(n)}{dn}. \tag{2.19}$$

The remained problem is the $\epsilon_{\text{xc}}^{\text{unif}}(n)$. Many-body systems are too difficult to solve exactly, even in the simple systems such as the uniform electron gas. Yet, the quantum Monte Carlo (QMC) calculations by Ceperley and Alder (46), and more recent works have provided essentially exact results for the uniform electron gas.

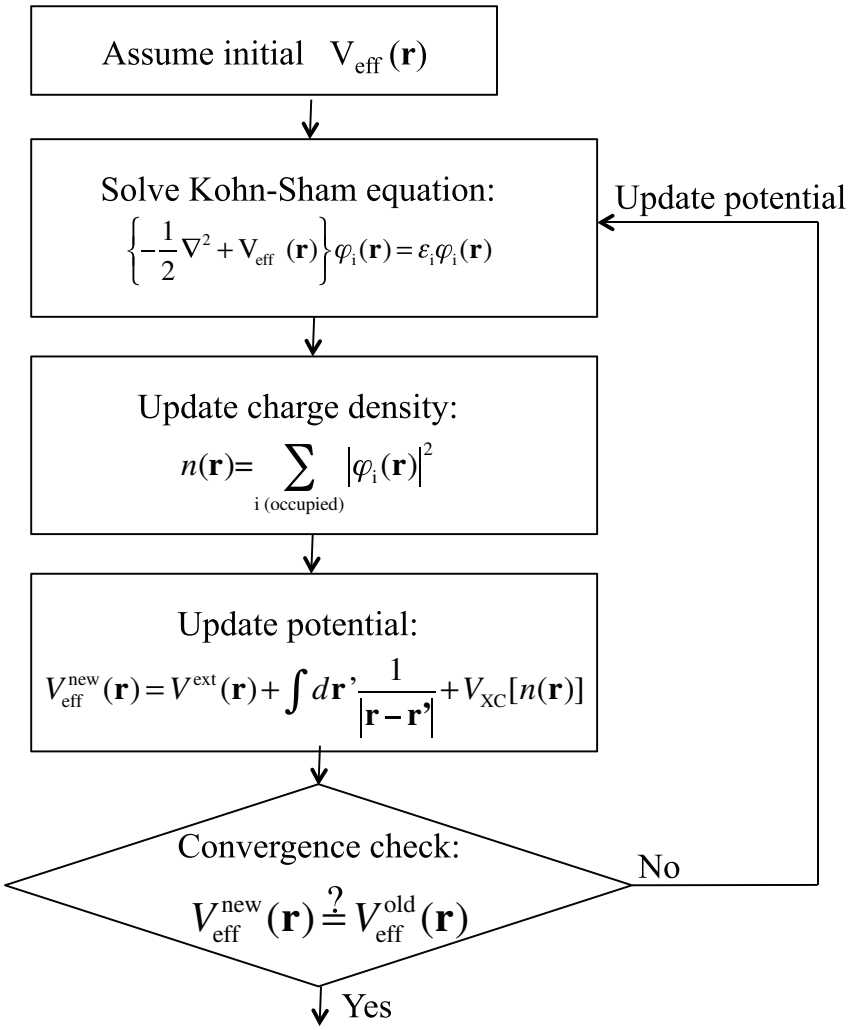

Figure 2.2: Schematic flowchart of the self-consistent field (SCF) loop. We have to solve the Kohn-Sham equation self-consistently, because the effective potential in the Kohn-Sham equation depends on the electron density or the Kohn-Sham orbitals. First, we assume an initial effective potential. Then, we solve the Kohn-Sham equation to get the electron density. The procedure is repeated until the updated potential accords with the previous potential.

2.4.2 Generalized-gradient approximation (GGA)

The LDA in the DFT has shown fantastic ability to understand and even predict material properties in spite of its relatively simple treatment of the exchange-correlation energy $E_{\rm xc}[n]$ as a functional of the electron density $n(\mathbf{r})$; e.g., for many materials, lattice and elastic constants are generally reproduced. The deviations from experimental values are within less than 1%-2% and several percent, respectively, in the LDA. Yet the LDA fails to describe some properties, including ground-state magnetic orderings even for bulk iron and for some transition-metal oxides. It also tends to overestimate the bonding strength, leading to an absolute error of molecular atomization energies. Some of the limitations of the LDA are remedied by the generalized-gradient approximation (GGA) (47, 48), in which the exchange-correlation energy is expressed in terms of not only the electron density but also its gradient. The molecular atomization energies are calculated with the error of several tenths of an electron volt, and the ground state of the bulk iron is correctly predicted to be a ferromagnetic body-center phase. The prevailing functional form of the GGA (PBE) generally provides better accuracy for structural properties of a variety of solids and activation energies in chemical reactions than the LDA does.

2.5 Psuedo-potential Method

We reviewed the theoretical framework of the DFT in the sections above. In practical applications to the real systems, we should choose a basis-function set to describe the wave function and the potential of the system. Usually the plane-wave-basis set is often used as a basis set, because of easy controllability of the accuracy with the number of plane waves, and easy estimation of differential and integral operators. Yet, a severe problem arises, what we call "variational collapse problem", in expanding the wave function with plane waves as follow: $\psi_{n\mathbf{k}}(\mathbf{r}) = e^{i\mathbf{k}\cdot\mathbf{r}} \sum_{|\mathbf{G}|\leq k_{\rm max}} \alpha_{\mathbf{G}} e^{i\mathbf{G}\cdot\mathbf{r}}$, where $k_{\rm max}$ represents the cutoff radius in the k-space.

2.5.1 Variational collapse problem

For simplicity, we consider the case of Silicon (Z=14) bulk. The lattice constant of Si is $a = 5.43$Å$= 10.26 a_{\rm B}$, and the unit cell is face-centered cubic with volume $\Omega = a^3/4$. The radius of $1s$ orbital of the silicon atom, a_{1s}, is $a_{1s} \approx a_{\rm B}/Z$, and the needed cutoff

radius in the k-space is $k_{\max} \approx 2\pi/a_{1s} = 2\pi Z/a_{\mathrm{B}}$. The number of the reciprocal vectors included within the sphere with the radius $k_{\max}$ is estimated as $Z^3(a/a_{\mathrm{B}})^3 \approx 10^6$. Therefore, the dimension of the Hamiltonian including the $1s$ orbital is $10^6 \times 10^6$. For the heavier atoms, larger number of basis functions are needed. The diagonalisation of the Hamiltonian is impossible.

2.5.2 Need of pseudo-potential method

As we see above subsection, the calculation cost of the practical application of the DFT to extended systems is still expensive. In particular, when we treat localized orbitals such as core electrons, large number of plane-wave basis are needed to describe such states. The number of the plane-wave basis is bigger and bigger, the diagonalisation of the Hamiltonian matrix needs more and more time. In addition, the core states are tightly bounded states and unchanged under the change of environments, thus expected to have little effect on most of the physical and chemical properties. The fundamental idea of a pseudo-potential is the replacement of the strong Coulomb potential of the nucleus and the effects of the tightly bounded core electrons by an effective ionic potential acting on the valence electrons. In more strict sense, the pseudo-potential method is to make a Hamiltonian including the pseudo-ion potential to reproduce the same phase shift for the scattering problem of the real system.

First, we perform the DFT calculation for an isolated atom. Suppose that the nucleus has a positive charge $+Ze$. After the calculation, we get the Kohn-Sham energy and orbitals of core electrons, $\{\epsilon_c\}$ and $\{\phi_c\}$, and valence electrons, $\{\epsilon_v\}$ and $\{\phi_v\}$ of an isolated atom:

$$[T_e + V^{\mathrm{all}}(\mathbf{r})]\,|\phi_i\rangle = \epsilon_i\,|\phi_i\rangle\,. \tag{2.20}$$

Then, we consider a Kohn-Sham equation as follows:

$$[T_e + V^{\mathrm{all}}(\mathbf{r}) + V_R(\mathbf{r})]\,|\phi_{\mathrm{ps}}\rangle = \epsilon_{\mathrm{ps}}\,|\phi_{\mathrm{ps}}\rangle\,, \tag{2.21}$$

and

$$V_R(\mathbf{r})\,|\phi_{\mathrm{ps}}\rangle = \sum_c |\phi_c\rangle\,\langle\phi_c|F|\phi_{\mathrm{ps}}\rangle\,, \tag{2.22}$$

where F is an arbitrary operator. Then, we can derive the $\{\phi_v\}$, and $\{\epsilon_v\}$ from the eigenfunction $\{\phi_{\mathrm{ps}}\}$, and $\{\epsilon_{\mathrm{ps}}\}$ in the following procedures:

$$\epsilon_{\mathrm{ps}} = \epsilon_v, \tag{2.23}$$

and

$$|\phi_v\rangle = |\phi_{\rm ps}\rangle - \sum_c |\phi_c\rangle \langle\phi_c|\phi_{\rm ps}\rangle \,. \tag{2.24}$$

Proof)
First, we give a proof of $\epsilon_{\rm ps} = \epsilon_v$. We operate $\langle\phi_v|$ on Eq. (2.21), then we derive

$$\epsilon_v \langle\phi_v|\phi_{\rm ps}\rangle = \epsilon_{\rm ps} \langle\phi_v|\phi_{\rm ps}\rangle \,, \tag{2.25}$$

because of $\langle\phi_v| V_R = 0$. Therefore, we can derive $\epsilon_{\rm ps} = \epsilon_v$, unless the $\phi_{\rm ps}$ is perpendicular to all the $\{\phi_v\}$. Usually, we exclude the possibility using the degree of freedom of the arbitrary operator, F.

Next, we give a proof of the second relation, Eq. (2.24). When the relation $\epsilon_{\rm ps} = \epsilon_v$ holds, we show that the defined wave function $|\phi'_v\rangle$ in the right hand side of Eq. (2.24) is an eigen function of the Eq. (2.20).

$$\begin{aligned}
[T_e + V^{\rm all} - \epsilon_v] \left|\phi'_v\right\rangle &= -V_R |\phi_{\rm ps}\rangle - \sum_c (\epsilon_c - \epsilon_v) |\phi_c\rangle \langle\phi_c|\phi_{\rm ps}\rangle \\
&= -V_R |\phi_{\rm ps}\rangle - \sum_c |\phi_c\rangle \langle\phi_c| T_e + V^{\rm all} - \epsilon_v |\phi_{\rm ps}\rangle \\
&= -\sum_c |\phi_c\rangle \langle\phi_c|F|\phi_{\rm ps}\rangle + \sum_{cc'} |\phi_c\rangle \langle\phi_c|\phi_{c'}\rangle \langle\phi_{c'}|F|\phi_{\rm ps}\rangle \\
&= 0.
\end{aligned} \tag{2.26}$$

□

Therefore, we can get the $\{\phi_v\}$ and $\{\epsilon_v\}$ from the Eq. (2.21), instead of the Eq. (2.20). There are some advantages in the Eq. (2.21): we do not have to treat the Hamiltonian including core-electron orbitals anymore. The potential from the core electrons are included in the effective potential $V^{\rm all}(\mathbf{r}) + V_R(\mathbf{r})$, and we call the potential "pseudo-potential". Here, we show an example of pseudo-potential of silicon atom at $F = \epsilon - \epsilon_c$ (50). We estimate the behavior of the pseudo-potential as follow:

$$\begin{aligned}
V_{\rm ps} |\phi_{\rm ps}\rangle &= V^{\rm all}(\mathbf{r}) |\phi_{\rm ps}\rangle + \sum_c |\phi_c\rangle \langle\phi_c| (\epsilon - \epsilon_c) |\phi_{\rm ps}\rangle \\
&= V^{\rm all}(\mathbf{r}) |\phi_{\rm ps}\rangle - \sum_c |\phi_c\rangle \langle\phi_c| H - \epsilon |\phi_{\rm ps}\rangle \\
&\approx V^{\rm all}(\mathbf{r}) |\phi_{\rm ps}\rangle - \sum_c |\phi_c\rangle \langle\phi_c| V^{\rm all} |\phi_{\rm ps}\rangle \,.
\end{aligned} \tag{2.27}$$

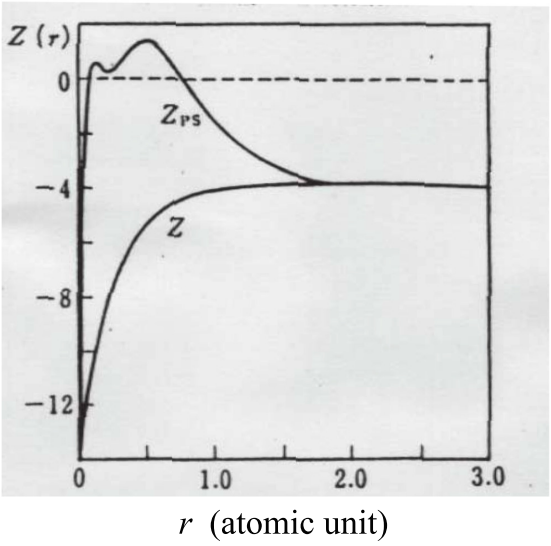

Figure 2.3: Pseudopotential of silicon atom. Comparison between the ion potential, $V(r) = \frac{Z(r)}{r}$, and pseudo-potential, $V_{\rm ps} = \frac{Z_{\rm ps}(r)}{r}$, from the Si^{+4} ion for the s-state.

Here, we have assumed that the potential energy is large enough to ignore the kinetic energy and eigenvalue in the neighborhood of nucleus. In that region, the steep potential from the nucleus is cancelled out considerably by the second term. In fact, it is clearly seen in Fig. 2.3 that the pseudo-potential becomes shallow potential than the bare-ion potential around the nucleus.

We use the pseudo-potential, which is made from the calculations of an isolated atom, even in the calculations of extended systems. Thus, the "transferability" is based on an idea that core electrons are not affected by the environments. Remark that such a pseudo-potential can be determined arbitrarily due to the arbitrary operator, F. Then, we usually impose three conditions on the pseudo-potential to reduce the calculation cost and to retain the transferability to different environments: (i) The pseudo-wave function $\phi_{\rm ps}$ has no nodes within a core radius r_c. (ii) $\phi_{\rm ps}(\mathbf{r})$ is equal to $\phi_v(\mathbf{r})$ outside the core radius r_c. (iii) The pseudo-potential $V_{\rm ps}$ gives the same phase shift as the real potential $V^{\rm all}$ in the neighborhood of, not only at, the eigenvalue.

2.5.3 Normconserving pseudo-potential

It is well known that the requirement (iii) is satisfied by "Norm conserving" (51, 52) condition. The Norm-conseriving condition is defined as follow:

$$\int_{r<r_c} |\phi_{ps}(\mathbf{r})|^2 = \int_{r<r_c} |\phi_v(\mathbf{r})|^2. \tag{2.28}$$

Remark that pseudo-potential $V_{\rm ps}$ is a nonlocal operator; $V_{\rm ps} = V^{\rm all}(\mathbf{r}) + \sum_c |\phi_c\rangle \langle\phi_c| \hat{F}$. We rewrite the $\phi_c(\mathbf{r})$ as $\phi_c(\mathbf{r}) = R_c(r)Y_{lm}(\theta,\phi)$, where $R_c(r)$ and $Y_{lm}(\theta,\phi)$ represent the radial function and spherical harmonic function of the core electron, respectively. Then we rewrite the pseudo-potential as follow:

$$\begin{aligned}
v_l^{\rm ion}(\mathbf{r}) &= \sum_{l,m}^{\infty} |lm\rangle\, v^{\rm ion}_{\rm nonlocal,l}(\mathbf{r})\, \langle lm| \\
&= \sum_{l=0,m}^{l_{max}-1} |lm\rangle\, v^{\rm ion}_{\rm nonlocal,l}(\mathbf{r})\, \langle lm| + \sum_{l=l_{\rm max},m}^{\infty} |lm\rangle\, v^{\rm ion}_{\rm nonlocal,l}(\mathbf{r})\, \langle lm| \\
&\simeq \sum_{l=0,m}^{l_{\rm max}-1} |lm\rangle\, v^{\rm ion}_{\rm nonlocal,l}(\mathbf{r})\, \langle lm| + v^{\rm ion}_{\rm local}(\mathbf{r}) \sum_{l=l_{\rm max},m}^{\rm infty} |lm\rangle\, \langle lm| \\
&= v^{\rm ion}_{\rm local}(\mathbf{r}) - v^{\rm ion}_{\rm local}(\mathbf{r}) \sum_{l=0,m}^{l_{\rm max}-1} |lm\rangle\, \langle lm| + \sum_{l=0,m}^{l_{\rm max}-1} |lm\rangle\, v^{\rm ion}_{\rm nonlocal,l}(\mathbf{r})\, \langle lm| \\
&= v^{\rm ion}_{\rm local}(\mathbf{r}) + \sum_{l=0,m}^{l_{\rm max}-1} |lm\rangle\, (v^{\rm ion}_{\rm nonlocal,l}(\mathbf{r}) - v^{\rm ion}_{\rm local}(\mathbf{r}))\, \langle lm| \\
&= v^{\rm ion}_{\rm local}(\mathbf{r}) + \sum_{l=0,m}^{l_{\rm max}-1} |lm\rangle\, v'^{\rm ion}_{\rm nonlocal,l}(\mathbf{r})\, \langle lm|\,,
\end{aligned}$$

where $|lm\rangle$ represents the spherical harmonic function, $v^{\rm ion}_{\rm nonlocal,l}(\mathbf{r})$ represents a pseudo-potential acting on an electron having the angular momentum l, $v^{\rm ion}_{\rm local,l}(\mathbf{r})$ represents a pseudo-potential acting on an electron having the angular momentum more than $l_{\rm max}$, $v'^{\rm ion}_{\rm nonlocal,l}(\mathbf{r})$ represents a remained pseudo-potential after removing the $v^{\rm ion}_{\rm local}(\mathbf{r})$ component from the $v^{\rm ion}_{\rm nonlocal,l}(\mathbf{r})$. In this way, a pseudo-potential is composed of the local part $v^{\rm ion}_{\rm local,l}(\mathbf{r})$ and nonlocal part $v^{\rm ion}_{\rm nonlocal,l}(\mathbf{r})$.

2.6 Underestimation of band gaps in LDA/GGA

In this section, we discuss a well-known problem in the LDA/GGA, that the LDA/GGA underestimates energy gaps in semiconductors and insulators. For example, silicon(Si)

is a semiconductor with band gap of 1.17 eV, but the calculated band gap by the GGA is 0.61 eV, thus showing 48 % underestimation. You might think that band gap is a quantity related to excited states. The DFT is only accurate for ground state properties, hence the error in the band gap does not matter. The idea, however, is wrong. The band gap is a well-defined ground-state property. Band gap, $\epsilon_{\rm gap}$, is formally defined as follow:

$$\begin{aligned} \epsilon_{\rm gap} &\equiv (E[N+1]-E[N])-(E[N]-E[N-1]) \\ &= -A+I, \end{aligned} \tag{2.29}$$

where $E[N]$ is the total energy of the N-electron system, A represents the electron affinity, and I represents the ionization energy. Therefore, the underestimation of the band gaps calculated by the LDA/GGA is an error inherent in the approximations.

Failures of the LDA/GGA are occasionally discussed in terms of the self-interaction error (SIE)(53, 54). An electron is under the electrostatic potential due to other electrons. Yet the expression of the electrostatic potential in the LDA/GGA includes the spurious interaction with the electron itself. When we consider the Hartree-Fock (HF) exchange potential with Kohn-Sham orbitals, this spurious self-interaction is cancelled by a term in the exchange potential. In the (semi)local expression of the exchange potential in the LDA(GGA), however, this cancellation is incomplete so that each electron is affected by the self-interaction. Several schemes to correct SIE are proposed and their capabilities have been examined for molecular systems(55, 56, 57, 58).

The SIE affects the band gaps substantially. In the DFT with the exact exchange-correlation energy, the band gap is expressed as the difference between the highest occupied Kohn-Sham level $\varepsilon_{N+1}(N+1)$ of the $(N+1)$-electron system and its counterpart of the N-electron system $\varepsilon_N(N)$: i.e., $\Delta E_{\rm g}=\varepsilon_{N+1}(N+1)-\varepsilon_N(N)$.(59, 60, 61, 62) When we introduce a fractional electron system with $N+f$ electrons as a mixed state of real integer-electron systems, then the total energy $E(N+f)$ becomes linear for $0<f<1$ and shows discontinuity at the integer value N for finite-gap systems. Using Janak theorem(63) which relates the Kohn-Sham level to the derivative of the total energy as $\varepsilon_{N+1}(N+f)=\partial E(N+f)/\partial f$, the linearity of $E(N+f)$ leads to the constant $\varepsilon_{N+1}(N+f)$ as a function of f. In the (semi)local approximations, however, the Kohn-Sham level $\varepsilon_{N+1}(N+f)$ $[\varepsilon_N(N-f)]$ increases (decreases) with increasing f due

to the self-interaction, leading to the concave shape of $E(N+f)$. This may cause an underestimate of the energy gap.(58, 64, 65)

The HF approximation (HFA) is free from the self-interaction. Yet the calculated band gaps in HFA are substantially overestimated due to the lack of the correlation energy. Hence the hybrid functionals combining LDA or GGA with HFA may be effective to break the limitation of the semilocal approximations. Recently several hybrid functionals have got a lot of attention as a post-LDA/GGA. Here we show three hybrid functionals: PBE0 (Perdew-Burke-Ernzerhof parameter-free) (48), HSE (Heyd-Sucseria-Ernzerhof) (66), and LC (long-range corrected) (68) functionals.

The PBE0 hybrid functional is given by

$$E_{\rm xc} = E_{\rm xc}^{\rm PBE} + \frac{1}{4}(E_{\rm x}^{\rm HF} - E_{\rm x}^{\rm PBE}), \tag{2.30}$$

leading to the mixing of 25 % HF exchange and 75 % PBE exchange, where we adopt the PBE(47) as GGA functional.

Heyd, Sucseria, and Ernzerhof have proposed(66) a different hybrid functional in which the long-range part of the HF-exchange energy is treated by the semilocal approximation in the DFT and the short-range part is calculated exactly. The actual procedure is conveniently done by splitting the Coulomb potential as

$$\frac{1}{r} = \frac{{\rm erfc}(\omega r)}{r} + \frac{{\rm erf}(\omega r)}{r}, \tag{2.31}$$

and applying the first term only, i.e., the screened Coulomb potential, to the HF-exchange energy. The second term to the exchange energy is calculated with the GGA. Adopting the mixing ratio in PBE0, then the HSE hybrid functional becomes

$$E_{\rm xc}^{\rm HSE} = E_{\rm xc}^{\rm PBE} + \frac{1}{4}(E_{\rm x}^{\rm HF,SR} - E_{\rm x}^{\rm PBE,SR}). \tag{2.32}$$

$E_{\rm X}^{\rm HF,SR}$ is the Fock-type double integral with the screened Coulomb potential.

The HSE functional partly removes SIE by incorporating the HF-exchange energy in the PBE functional. Yet the cancellation of the Hartree potential and the exchange potential is absent in the long-range part. This may cause erroneous description of, e.g., the Rydberg states in isolated polyatomic systems or properties of charge-transfer systems. To remedy this point, application of the long-range part of the Coulomb

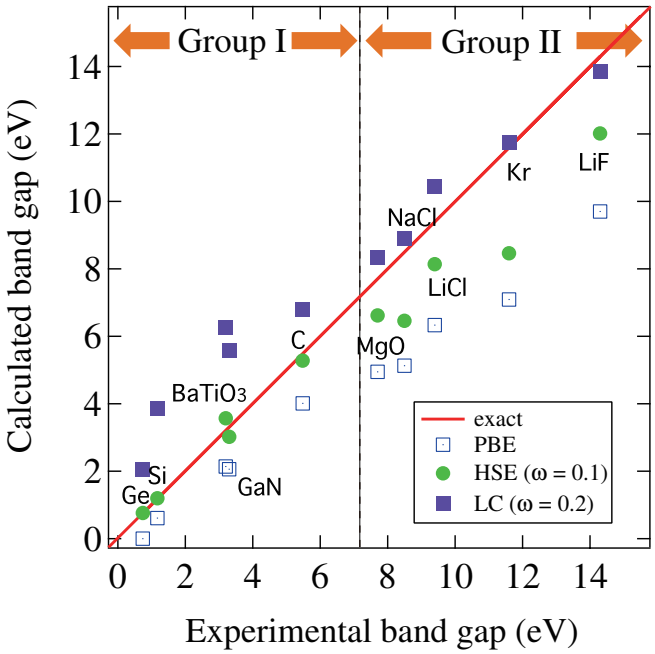

Figure 2.4: Calculated band gaps obtained from different exchange-correlation functionals: PBE (blank squares), HSE with ω=0.1 a_B^{-1} (green dots), and LC with ω=0.2 a_B^{-1} (purple squares), plotted against experimental band gaps. Group I consists of materials having the experimental gap less than 7 eV, while Group II is composed of materials with the gap more than 7 eV. (Ref. (69))

potential to the HF-exchange energy is necessary (67). The long-range corrected (LC) functional has been proposed based on this viewpoint (68), being expressed as

$$E_{\rm xc}^{\rm LC} = E_{\rm xc}^{\rm PBE} + (E_{\rm x}^{\rm HF,LR} - E_{\rm x}^{\rm PBE,LR}), \tag{2.33}$$

with $E_{\rm X}^{\rm HF,LR}$ being the Fock-type double integral with the long-range part of the Coulomb potential [the second term of Eq. (2.31)].

Figure 2.4 is a summary of calculated band gaps by the PBE(GGA), HSE and LC functionals. For the HSE and LC, the calculated results with the ω values: $\omega = 0.1$ $a_{\rm B}^{-1}$ for the HSE and $\omega = 0.2$ $a_{\rm B}^{-1}$ for the LC. It is clearly shown that the calculated band gaps by the hybrid functionals, PBE0, HSE and LC, are in better agreement with the experimental values than the PBE (GGA) approximation, indicating the promising possibility of the hybrid functionals. It is clearly seen that the HSE is a good approximation for relatively small-gap materials and that the LC is a good approximation for

relatively large-gap materials.

We discuss which functional is appropriate for this study in Sec. 3.2.

2.7 Parameters in this study

In this section, we describe our calculation details. We used in this study the plane-wave-basis-set total-energy band-structure calculation code, TAPP(70, 71, 72), and the linearlized-combination-of-atomic orbital (LCAO) calculation code, OpenMX (73, 74). Our calculations have been performed in the generalized gradient approximations (GGA) (47, 48) in the density functional theory (DFT) (40, 41). Nuclei and core electrons are simulated by either norm-conserving(49) pseudo-potentials in the TAPP code.

We generate norm-conserving pseudo-potential to simulate nuclei and core electrons, following a recipe by Troullier and Matins.(49) The core radius r_c is an essential parameter to determine transferability of the generated pseudo-potential. We have examined r_c dependence of the calculated structural properties of benchmark materials and adopted the pseudo-potentials generated with the following core radii in this paper: 0.85 Å for Si $3s$, and 1.16 Å for Si $3p$, 1.06 Å for Ga $4s$ and $4p$, and 1.48 Å for Ga $4d$, 0.64 Å for N $2s$ and $2p$, 0.85 Å for C $2s$ and $2p$, 1.06 Å for Al $3s$, $3p$, and $3d$, 0.847 Å for B $2s$ and $2p$.

3

Floating states in sp^3-bonded materials

In Sec. 3.1, we provide the calculational results of structural parameters, such as lattice constants and total energies for each polytype of the six materials: SiC, AlN, BN, GaN, diamond, and Si. Sec. 3.2 presents the results for electronic band structures for the obtained structures. In Sec. 3.3, the mechanism of the band-gap variations is discussed in detail. In that section, we have found a peculiar electron state, which we call floating state. We have clarified the mechanism of substantial band-gap variation by considering the floating state. In Sec. 3.4, we discuss why floating states are ubiquitous in sp^3-bonded materials. Sec. 3.5 is devoted to examine capability of the linear-combination-of-atomic-orbital (LCAO) calculations in describing floating states.

3.1 Determination of structural parameters

In this section, we focus on three polytypes, called $2H$, $3C$, and $6H$, of each material to reveal correlation between their structures and electronic properties.

The parameters used in this study are followings: Appropriate choice of cutoff energies $E_{\rm cut}$ in the plane-wave-basis set, which is related to hardness of the adopted norm-conserving pseudo-potentials, is a principal ingredient to assure the accuracy of the results. We have examined convergence of structural properties and band gaps with respect to $E_{\rm cut}$ and reached the following well converged values with $E_{\rm cut}$ for each material: the cut-off energy in the plane-wave-basis set is chosen to be 49 Ryd except

for 64 Ryd for AlN and 81 Ryd for BN to assure the accuracy in the total-energy of 16 meV per molecular unit and that in the band gap of 10 meV. The remaining important ingredient to assure our assessment is the sampling **k** points for the BZ integration. We have adopted a unit cell of the $6H$ structure even for $2H$ and $3C$ structures to facilitate the comparison among the polytypes. We have adopted the scheme by Monkhorst and Pack in which BZ is divided by equally spaced mesh. After careful examination, we have found that 10×10×2 sampling **k** points are enough to assure the accuracy of the total energies and energy bands in the six materials. A structural optimization of internal atomic coordinates has been performed using Hellmann-Feynman forces in the unit cell. Our criterion for optimizing the internal coordinates is that the maximum force acting on each atom should be less than 10^{-3} Ht/bohr.

At first, we have theoretically determined lattice constants in the hexagonal plane and along the stacking direction, a and c in the GGA. The obtained a and the ratio c/na of each polytype are listed in Table 3.1, where n represents the number of bilayers. The differences of c/na among the polytypes are found to be extremely small, meaning the distortion along the c-axis is quite small. Our calculated lattice constants agree with experimental data available with an error of at most 2 %. Table 3.1 also shows the calculated total energy differences (ΔE) among the polytypes for SiC, AlN, BN, GaN, Si, and C using the calculated structural parameters. The table includes some polytypes not observed yet, .e.g, 6H-AlN. Yet, it is likely that these polytypes are synthesized since the total energy difference is small, being in the range of 50 meV or less per molecular unit. The most energetically favorable polytype in SiC is the $6H$ followed by the $3C$ with the energy increase of 1.2 meV per SiC molecular unit. It is said that $4H$ is also one of the most energetically favorable polytypes. Yet, the $6H$ structure is a often observed polytype in experiments, and our calculations show quite small difference in total energy than that of $4H$ polytype by 0.1 meV. Then we discuss the $6H$ polytype in this study. The least energetically favorable polytype is $2H$ whose total energy is higher than $6H$ by 7.1 meV per SiC. The obtained total energies are consistent with the experimental facts that $3C$-SiC and $6H$-SiC polytypes are only synthesized by Molecular Beam Epitaxy (MBE). We have found that, compared with other materials, SiC exhibits smaller energy difference among polytypes. As for the other materials, most stable structure of each material is $2H$-AlN, $2H$-BN, $2H$-GaN, $3C$-Si, and $3C$-C,

respectively. The most stable structures in other materials are commonly observed in experiments.

3.2 Electronic band structures

Fig. 3.1 shows calculated electronic energy bands for polytypes of the six materials. Remark that we have adopted a unit cell of the $6H$ structure even for $2H$ and $3C$ structures to facilitate the comparison among the polytypes. From the figures, the valence bands of the three polytypes resemble each other in each material. The tiny differences come from the difference of the symmetries by which degenerate states in the high-symmetry structure split in the low-symmetry structure. The valence-band top is located at Γ point in all the polytypes in all the materials. In contrast, the conduction bands are qualitatively different among polytypes in spite of their structural similarity in the local atomic arrangement. In the SiC polytypes, the conduction-band minimum (CBM) is located at K point in the $2H$-structure, whereas it is at M point in the $3C$-, and $6H$-structure. The X point in the cubic Brillouin zone (BZ) is folded on the M point in the hexagonal BZ. Furthermore, the lowest conduction band in the $3C$ structure is isolated and shifts downwards substantially, making the band gap narrower by 0.7 - 0.9 eV than those in the $6H$ and $2H$ polytypes. The calculated energy bands for other compounds clearly show the same feature as in SiC, i.e., the CBM in the $3C$-AlN, $3C$-BN is located at M point, whereas that in the $2H$-BN, and $2H$-diamond is located at the K point.

The calculated and experimental band gaps for the polytypes are given in Table 3.2. Overall features of the calculated band gaps are in accord with the experimental values. As discussed in Sec. 2.6, it is clearly seen that the GGA underestimates energy gaps by about 50% because of the shortcoming inherent in the GGA. If necessary, the quantitative description of the energy gaps is possible using more sophisticated schemes of the GW (84, 85, 86) for quasiparticle-self energy or HSE functional (66, 69, 87, 88, 89, 90, 91) for the exchange-correlation energy. Yet, the relative difference in the energy gap calculated by the GGA among the polytypes is well reproduced, i.e., calculated results show the band gap of the $3C$-SiC is smaller than that of the $2H$-SiC by 0.936 eV, which corresponds to the experimental one, 0.93 eV. Therefore, in this

Table 3.1: Calculated hexagonal lattice constant a and ratio c/na for different polytypes labeled as either nH or nC ($n = 3$) of the various sp^3-bonded semiconductors. Calculated total energies per molecular unit are also shown. The values are relative to the energy of the corresponding most stable structure. Hexagonality H (explained in Sec. 1.2) is also listed.

Materials	a [Å]		c/na		ΔE [meV]	H (%)
	this work	Expt.	this work	Expt.		
2H-SiC	3.085	3.076 (Ref. (75))	0.8217	0.8205 (Ref. (75))	7.1	100
3C-SiC	3.091	3.083 (Ref. (76))	0.8165	0.8165 (Ref. (76))	1.2	0
6H-SiC	3.091	3.081 (Ref. (77))	0.8180	0.8179 (Ref. (77))	0	33
2H-AlN	3.117	3.110 (Ref. (78))	0.8103	0.8005 (Ref. (78))	0	100
3C-AlN	3.112	3.090 (Ref. (79))	0.8165	0.8165 (Ref. (79))	41.9	0
6H-AlN	3.112	–	0.8148	–	28.4	33
2H-BN	2.556	2.553 (Ref. (80))	0.8252	0.8265 (Ref. (80))	35.5	100
3C-BN	2.561	2.557 (Ref. (80))	0.8165	0.8165 (Ref. (80))	0	0
6H-BN	2.556	2.500 (Ref. (81))	0.8203	0.8293 (Ref. (81))	9.6	33
2H-GaN	3.255	3.189 (Ref. (82))	0.8156	0.8130 (Ref. (82))	0	100
3C-GaN	3.255	3.175 (Ref. (83))	0.8165	0.8165 (Ref. (83))	15.3	0
6H-GaN	3.255	–	0.8159	–	9.5	33
2H-Si	3.853	–	0.8238	–	22.3	100
3C-Si	3.863	3.863 (Ref. (83))	0.8165	0.8165 (Ref. (83))	0	0
6H-Si	3.858	–	0.8193	–	4.0	33
2H-C	2.503	–	0.832	–	50.9	100
3C-C	2.514	2.519 (Ref. (83))	0.8165	0.8165 (Ref. (83))	0	0
6H-C	2.508	–	0.8230	–	12.8	33

study, we have adopted the GGA, which is verified to be accurate even quantitatively to study the variation of the band gap among the polytypes.

From the Table 3.2, it has been found that the large band-gap variation is not limited to the SiC polytypes. For AlN and BN, the energy gap decreases substantially in the $3C$ structures by 0.9 eV and 0.8 eV, respectively. In the case of AlN, the CBM at M point shifts downwards substantially, so that the transition between the direct gap in the most stable $2H$-structure and the indirect gap in the metastable $3C$-structure takes place. This result gives good agreement with the observed experimental fact. In contrast, for the diamond polytypes, the band-gap decrease occurs not at the $3C$-structure, but at the $2H$-structure: the energy gap varies from 4.521 eV in the $6H$-structure to 3.406 eV in the $2H$-structure.

3.3 Floating states and band-gap variation

In this section, we show the microscopic mechanism of the band-gap variation. We have found that peculiar electron states having a NFE-like character play important roles in the band-gap variation. The peculiar electron states float in interstitial channels in most semiconductors. The directions and shapes of the interstitial channels depend on the crystal symmetry so that mysterious variation of the energy gaps in SiC polytypes is naturally explained by considering the floating nature. We show the floating states in the $3C$ structures in Sec. 3.3.1, and in the $2H$ structures in Sec. 3.3.2.

3.3.1 Floating states in $3C$ structure

Figures 3.2 (a) and (b) show the Kohn-Sham (KS) orbital at the CBM of the $3C$-SiC on $(0\bar{1}1)$, and (110) plane, respectively, obtained in the GGA calculations. Surprisingly, the orbital distributes not near atomic sites but extends, or $floats$, in channels along $\langle 110 \rangle$ direction. The orbital changes its sign along the $\langle 110 \rangle$ channel with the periodicity of $\sqrt{2}a_0$ (a_0: lattice constant) and has nodes on the atomic plane containing Si atoms, thus avoiding atomic sites and distributing solely in the internal space. By examining the irreducible representation at M point, it is found that this phase variation of the KS orbital is allowed only at M point in the hexagonal BZ.

Figure 3.2(c) shows the contribution from the kinetic-energy,

$$\varepsilon_{\rm kin} = \langle \varphi_i | -\nabla^2/2 | \varphi_i \rangle, \tag{3.1}$$

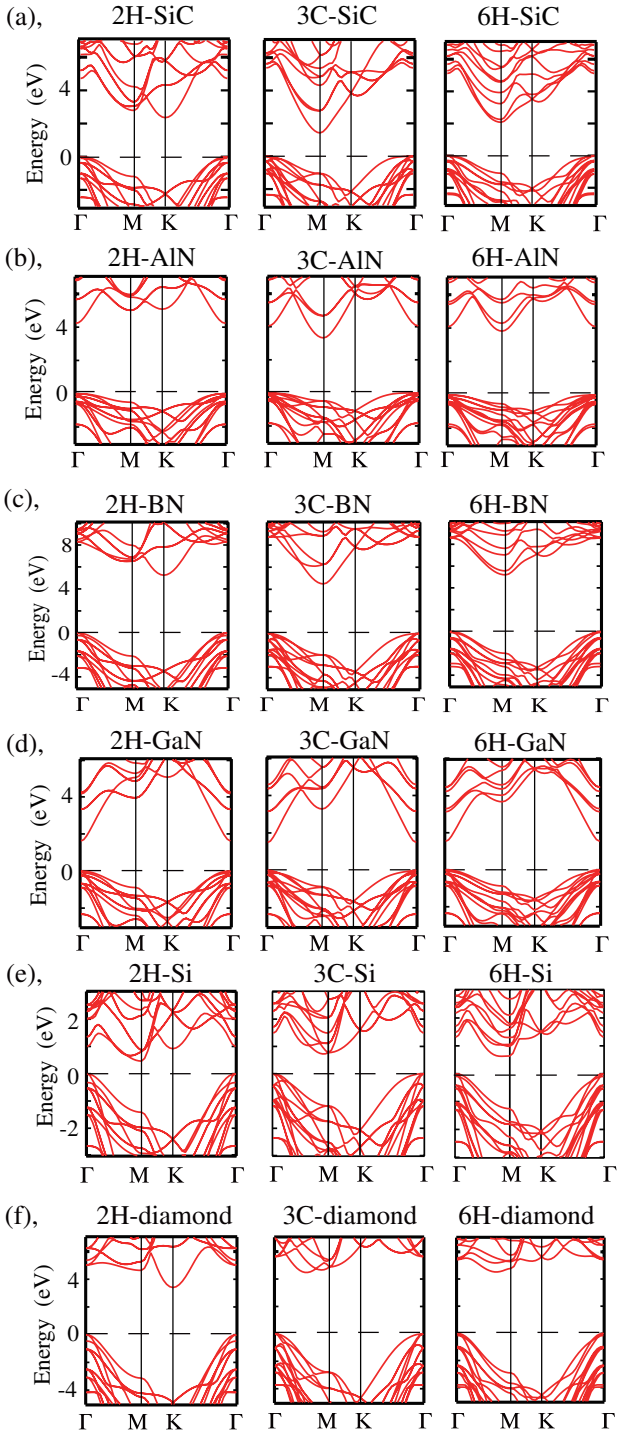

Figure 3.1: Band structures calculated by the GGA. The energy of the valence-band top is set 0. In these calculations, we adopted supercell calculations, so that the number of electrons is equal to each other for easy comparison and they have the same Bullirouin zone. Note that $3C$ structures are also calculated in the hexagonal supercell, thus the X point in cubic cell being folded to M point.

Table 3.2: Calculated, ϵ_{gap}, and experimental, $\epsilon_{\text{expt.}}$, energy gaps of the $2H$, $3C$ and $6H$ structures for various sp^3-bonded semiconductors. Hexagonality is also listed. Experimental data are taken for SiC from Ref. (92), for $2H$-AlN from Ref. (93), for $3C$-AlN from Ref. (94), for $3C$-BN from Ref. (95), for GaN, Si, and diamond from Ref. (83).

Materials	ϵ_{gap} (eV)	$\epsilon_{\text{expt.}}$ (eV)	H (%)
$2H$-SiC	2.355 (indirect)	3.33 (indirect)	100
$3C$-SiC	1.419 (indirect)	2.40 (indirect)	0
$6H$-SiC	2.077 (indirect)	3.10 (indirect)	33
$2H$-AlN	4.233 (indirect)	6.23 (direct)	100
$3C$-AlN	3.328 (indirect)	5.34 (indirect)	0
$6H$-AlN	3.817 (indirect)	–	33
$2H$-BN	5.251 (indirect)	–	100
$3C$-BN	4.487 (indirect)	6.4 (indirect)	0
$6H$-BN	5.190 (indirect)	–	33
$2H$-GaN	1.622 (direct)	3.28 (direct)	100
$3C$-GaN	1.489 (direct)	3.47 (direct)	0
$6H$-GaN	1.533 (indirect)	–	33
$2H$-Si	0.477 (indirect)	–	100
$3C$-Si	0.660 (indirect)	1.17 (indirect)	0
$6H$-Si	0.639 (indirect)	–	33
$2H$-diamond	3.406 (indirect)	–	100
$3C$-diamond	4.246 (indirect)	5.48 (indirect)	0
$6H$-diamond	4.521 (indirect)	–	33

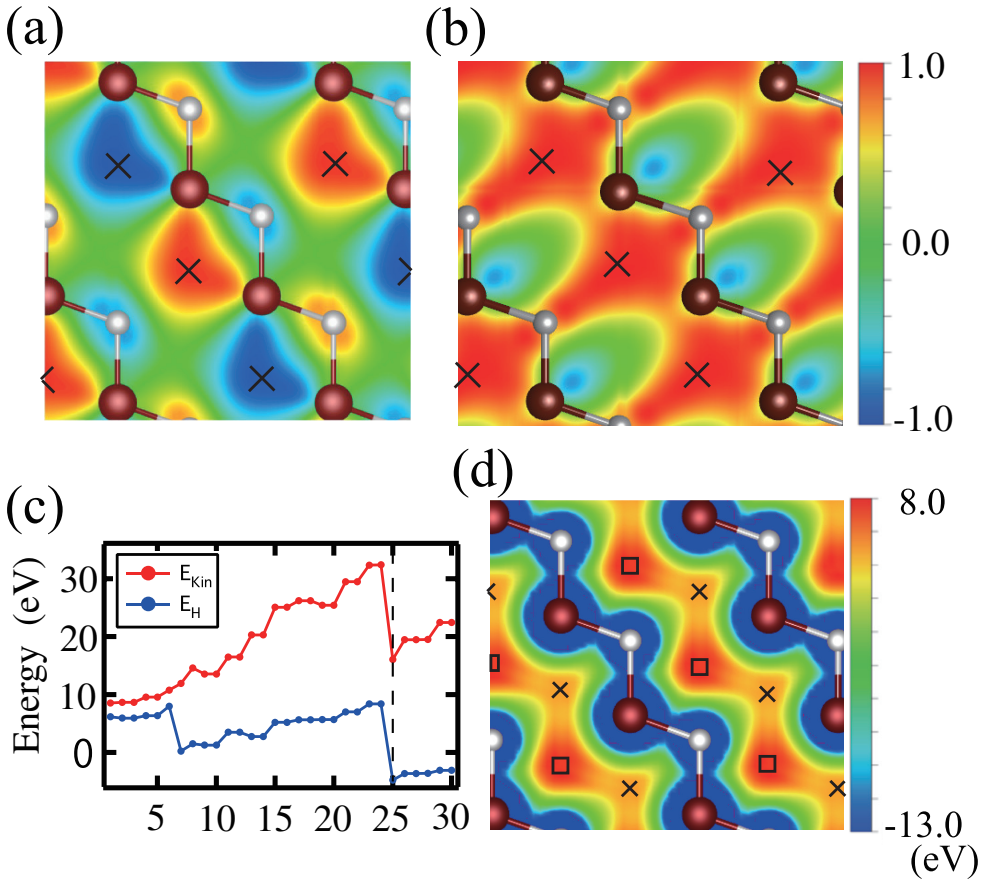

Figure 3.2: (a), (b) Contour plots of the calculated Kohn-Sham(KS) orbital of the conduction band minimum at M point in the $3C$-SiC on $(0\bar{1}1)$ and (110) plane, respectively. The M point which we discuss corresponds to $X = (0, 0, 2\pi/a_0)$ in cubic BZ. (c) Energy analyses of KS orbitals in $3C$-SiC. The kinetic-energy contribution, $\varepsilon_{\rm kin} = \langle\varphi_i| - \nabla^2/2|\varphi_i\rangle$, and the Hartree-energy contribution, $\varepsilon_{\rm H} = \langle\varphi_i| \int \rho(\mathbf{r}')/|\mathbf{r} - \mathbf{r}'|d\mathbf{r}'|\varphi_i\rangle$, to the orbital energies of each KS state for M point in $3C$-SiC. The abscissa represents the ith KS state from the valence-band bottom and the 25th state is the conduction-band minimum. (d), Contour plots of the effective potential in the KS equation. The brown and white balls depict Si atoms and C atoms, respectively. In these contour plots, the mark 'X' represents the tetrahedral (T_d) interstitial sites surrounded by Si atoms, and the mark square represents the T_d interstitial sites surrounded by carbon atoms.

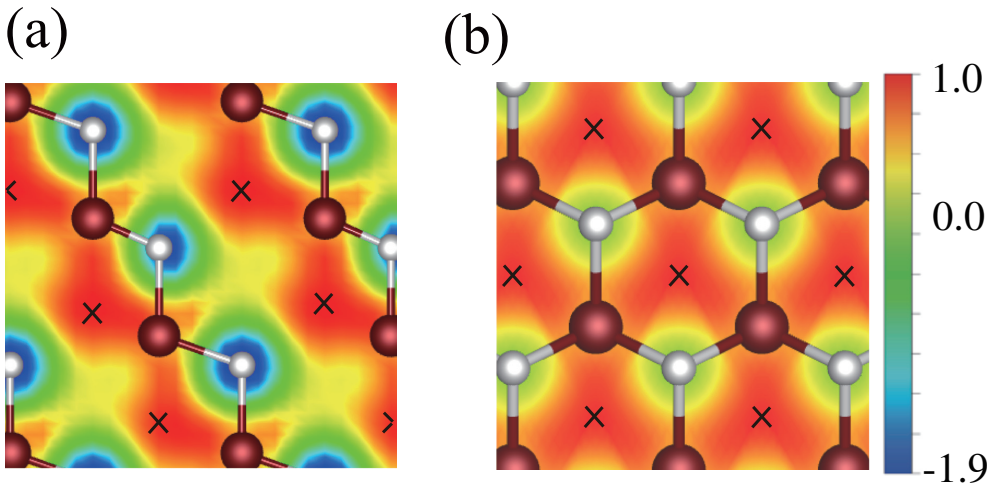

Figure 3.3: Contour plots of the calculated Kohn-Sham(KS) orbital of the fourth-lowest-conduction-band minimum at Γ point in the 3*C*-SiC on (110) (a) and (111) (b) plane. In these contour plots, the brown and white balls depict Si atoms and C atoms, respectively. The mark 'X' represents the tetrahedral (T_d) interstitial sites surrounded by Si atoms.

and that from the Hartree-energy,

$$\varepsilon_{\mathrm{H}} = \langle\varphi_i| \int \rho(\mathbf{r}')/|\mathbf{r}-\mathbf{r}'|d\mathbf{r}'|\varphi_i\rangle, \tag{3.2}$$

to the orbital energy of each KS state at M point in the 3*C*-SiC. It is clear that the floating state gains the kinetic energy and the Hartree energy, compared with other states. The kinetic-energy gain obviously comes from the extended orbital distribution in the ⟨110⟩ channel. The Hartree-energy gain, on the other hand, comes from ionic character of SiC. The electronegativity of C, 2.55, is larger than that of Si, 1.90, causing the electron transfer from Si to C in SiC. Our calculations indeed show that the electrostatic potential at the tetrahedral (T_d) interstitial site surrounded by 4 Si atoms is lower than that at another T_d site surrounded by 4 C atoms by 2.56 eV (See Fig. 3.2(d)). The floating state has the maximum amplitude at the Si-surrounded T_d sites, thus floating in the ⟨110⟩ channel. These energy gains cause the band-gap narrowing at M point.

The floating-state orbital with its sign unchanged along the ⟨110⟩ channel is also possible. Such in-phase state is allowed, however, not at M point but at Γ point. Furthermore, the in-phase orbital has amplitudes inevitably at atomic sites, thus mixing

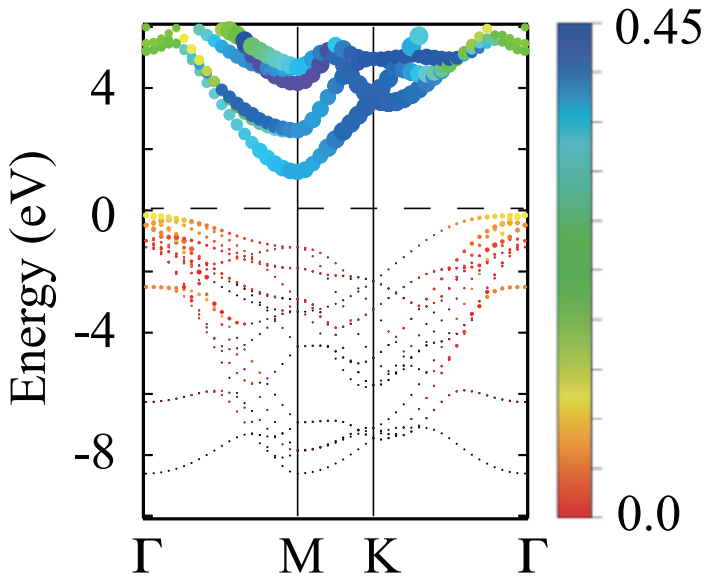

Figure 3.4: Component of wave function outside the s- and p-atomic orbitals in the $3C$-SiC. The residual norm is represented by the color and the size of the dots. The energy of the valence-band top is set 0. The residual norm is defined as Eq. (3.3) in the text.

with mainly s-character orbitals. We have indeed found such hybridized states at Γ point as shown in Fig. 3.3(a) and (b): The fourth lowest conduction-band at Γ which is the lowest conduction-band state at L point in the original cubic BZ is the anti-bonding state of the in-phase floating state and s orbitals of C. This mixing with atomic orbitals makes the resultant hybridized state shift upwards due to the kinetic- and Hartree-energy increase.

In order to identify the floating electron bands, it is useful to calculate the residual norm of the wave function after projecting it to the s- and p-atomic orbitals. The quantity is calculated in the following procedure. Remark that atomic orbitals centered on different lattice sites are not orthogonal. Therefore, from the pseudo-atomic orbitals ϕ_s^{isolated} and ϕ_p^{isolated} of isolated silicon and carbon atoms, we have composed orthonormal basis set $\{\phi_i^{\text{atom}}\}$ with the Gram-Schmidt orthonormalization. Then we have calculated the squared residual norm, which is defined as follows:

$$\left| |\phi_{n\mathbf{k}}\rangle - \sum_i |\phi_i^{\text{atom}}\rangle \langle \phi_i^{\text{atom}} | \phi_{n\mathbf{k}}\rangle \right|^2 \tag{3.3}$$

for each k point, and each band n. Figure 3.4 shows the calculated squared norm of the residual components for the $3C$-SiC. It is clearly shown that the valence bands are well described in the linear combination of the atomic s- and p-orbitals. The squared norm of the residual wave function at the valence-band top is only 0.09. On the other hand, as for the electron state at the CBM, the residual norm is as much as 0.33. It is clear that the floating state is difficult to be described by the s-, and p-atomic orbitals only. Yet, it is also found that the 66% component of the CBM is explained by the atomic orbitals. More detailed discussions are in Sec. 3.5.1. Furthermore, it is also clearly seen in Fig. 3.4 that the wave function of the CBM at K point has also floating nature; i.e., 0.37. It extends along the $[1\bar{1}0]$, $[10\bar{1}]$, and $[01\bar{1}]$ channels on (111) plane and mixes with C atomic orbitals (See Figure 3.5). Fig. 3.5(d) shows that the kinetic-energy and the Hartree-energy gains for the floating states at K point are 6.8 eV and 9.1 eV, respectively, compared with the valence-band top state, which is of usual atomic-orbital character.

The existence of floating states is expected in other sp^3-bonded compound semiconductors, $3C$-AlN, $3C$-BN, and $3C$-GaN. Fig. 3.6 shows the KS orbitals at the CBM at M and Γ point in these materials. The KS orbitals distribute broadly around the T_d interstitial sites and the cation sites, exhibiting the floating character. These characteristics are similar to those of the floating states existing in the $3C$-SiC.

Below we discuss why large band-gap decrease does not occur in $2H$ and $6H$ structures of compound semiconductors. We explain the reasons by considering the channel length and charge transfer. As mentioned above, in the $3C$ structures, the $\langle 110 \rangle$ channels play important roles in the variations in energy gaps. A similar structural feature is observed in $6H$ structure. There is a channel with the length of about $7a_0/2\sqrt{2}$ along $\langle \bar{2}201 \rangle$ which is slanted relative to [0001] direction. At the hexagonal-stacking layer, the slanted channels are closed. Hexagonal-stacking layers play as a wall of the channels, thus interrupting the floating character of electrons in the slated channels. Due to the limited length in the channel, the kinetic energy gain is smaller than in $3C$ structure and the energy gap in $6H$ structure become wider [Fig. 3.1]. We have indeed found that the KS orbital of the CBM at M point in $6H$-SiC floats in this channel [Fig. 3.7]. The contour plots (a) and (b) show that the floating state at M point distributes in the finite-length slanted $\langle 2\bar{2}01 \rangle$ channels broadly. The contour plots (c) and (d) show

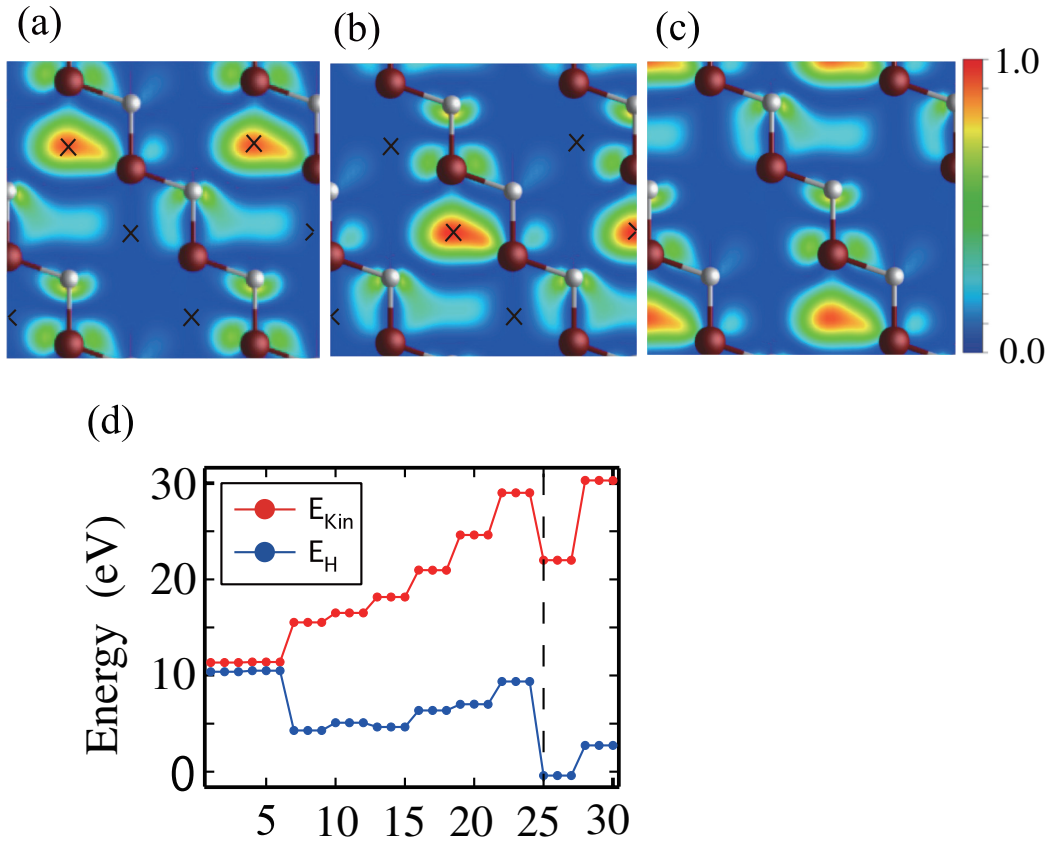

Figure 3.5: Contour plots of Kohn-Sham (KS) orbitals in 3C-SiC (a), (b), and (c). Contour plots of squared KS orbitals at the conduction-band minimum (CBM) at K point are shown on (110) plane. The CBM state is triply degenerate since we use a unit cell being three times longer along (111) direction. Burgundy and white balls depict Si and C atoms, respectively. Each state distributes in three channels along $[1\bar{1}0]$, $[10\bar{1}]$, and $[01\bar{1}]$ directions, thus floating in (111) plane. Atomic orbitals of C atoms contribute to this state with different phases. (d): Energy analyses of KS orbitals in 3C-SiC. The kinetic-energy contribution, $\varepsilon_{\rm kin} = \langle\varphi_i| - \nabla^2/2|\varphi_i\rangle$, and the Hartree-energy contribution, $\varepsilon_{\rm H} = \langle\varphi_i| \int \rho(\mathbf{r}')/|\mathbf{r} - \mathbf{r}'|d\mathbf{r}'|\varphi_i\rangle$, to the orbital energies of each KS state for M point in 3C-SiC. The abscissa represents the ith KS state from the valence-band bottom and the 25th state is the CBM.

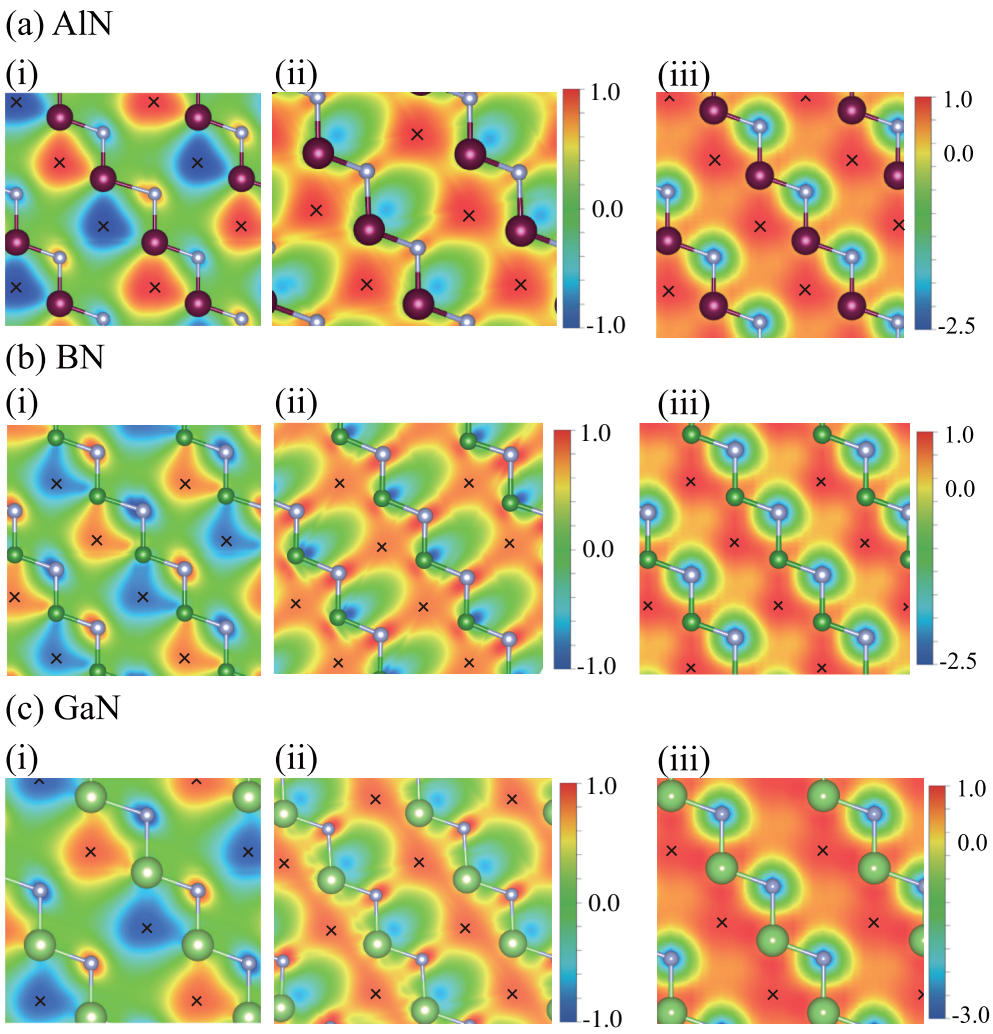

Figure 3.6: Contour plots of the calculated Kohn-Sham (KS) orbitals of the conduction-band minimum at M (left and central panels) and Γ point (right panel) for the $3C$-AlN (a), $3C$-BN (b), and $3C$-GaN (c) on $(0\bar{1}1)$ (left, right panel) and (110) (central panel) plane. The M point which we discuss corresponds to $X = (0, 0, 2\pi/a_0)$ in cubic BZ. The mark 'X' depicts the tetrahedral (T_d) interstitial sites surrounded by cations. In Fig. (a), purple(large) and white(small) balls depict aluminum and nitrogen atoms, respectively. In Fig. (b), green and white balls are boron and nitrogen atoms, respectively, in Fig. (c), green and white is gallium and nitrogen atoms, respectively.

the floating state at K point. The floating state clearly extends the horizontal channels broadly. They resemble the corresponding KS orbitals in $3C$-SiC. The relations between the channel length and band gap is discussed in Sec. 5.1 in more details.

Next we refer to the case of the $2H$ structure. As mentioned above, charge transfer plays important roles in the substantial band-gap decrease in the $3C$ structures. Due to the electron transfer from silicon to carbon, the $\langle 110 \rangle$ channels are surrounded by positive Si atoms, and cause the energy level of the floating state lower. In contrast, in the $2H$-structure such a cation-surrounded channel is absent. The internal space surrounded by cations overlaps considerably with that by anions in the $2H$ structure [Fig. 3.8]. The cation-surrounded interstitial site is very close to the anion-surrounded one with the separation of $1/3$ d, where d is the bond length between silicon and carbon atoms. In fact, the electrostatic potential at the cation-surrounded interstitial sites is almost the same as that at anion-surrounded ones within 0.1 eV. Therefore, in the $2H$ structures, charge transfer doesn't cause the substantial band-gap shift.

Next we discuss why the elementary semiconductors do not exhibit the energy-gap decreases in the $3C$ polytype. There is no charge transfer in the $3C$-Si and $3C$-diamond. This means that these systems lack one reason for the decrease of energy gap. Yet, even in elemental semiconductors, the floating states exist although they are not necessarily at the CBM. We have examined cubic Si and C and indeed found the floating states. For $3C$-Si, Fig. 3.9(a) shows the KS orbital of the CBM at M point (X point in cubic BZ). We have found this state has the bonding character of the floating and the atomic-orbital states. From the tight-binding picture, the CBM at M point is the anti-bonding state of the s orbital and the neighboring p orbital extending along $\langle 001 \rangle$ direction. This state is mixed with the floating state and thus the KS orbital distributes in the $\langle 110 \rangle$ channel. The KS orbital of the valence-band-bottom state at Γ is shown in Fig. 3.9(b). Basically it is the bonding state of s orbitals, but extends in the interstitial region substantially: The calculated amplitude at the interstitial T_d site is 23 % of the maximum amplitude in sharp contrast with the valence-band-top state which is the bonding state of p orbitals with the amplitude at T_d site being about 1 % of the maximum value. Hence the valence-band-bottom state is obviously the bonding state between s orbitals and the floating state. The KS orbital of the anti-bonding counterpart which is located at 7.81 eV above the valence-band top, i.e., above the vacuum level, is shown in Fig. 3.9(c), clearly exhibiting the floating character.

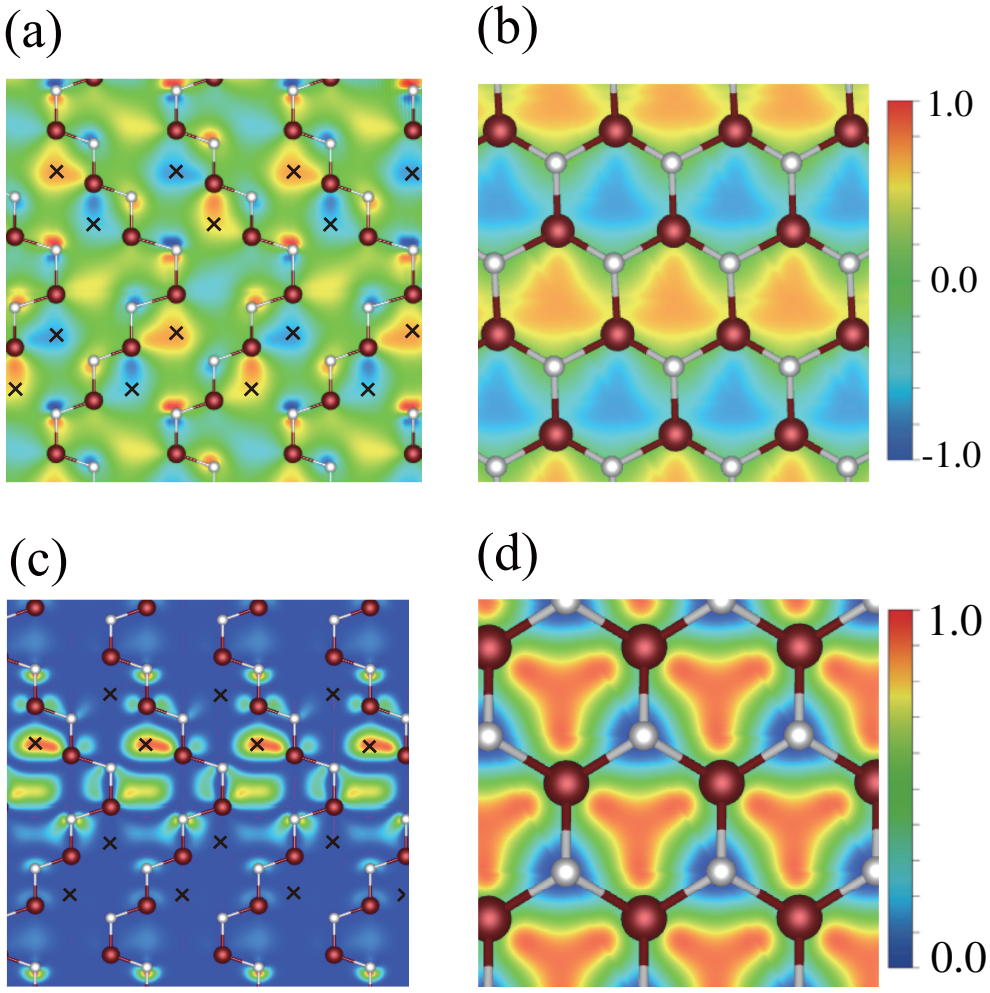

Figure 3.7: Contour plots of the calculated Kohn-Sham (KS) orbitals of the conduction-band minimum at M point [(a) and (b)], and at K point [(c) and (d)] for 6H-SiC on (11$\bar{2}$0) [(a) and (c)] and (0001) [(b) and (d)] plane. The brown and white balls depict Si atoms and C atoms, respectively. The mark 'X' represents the tetrahedral (T_d) interstitial sites surrounded by Si atoms.

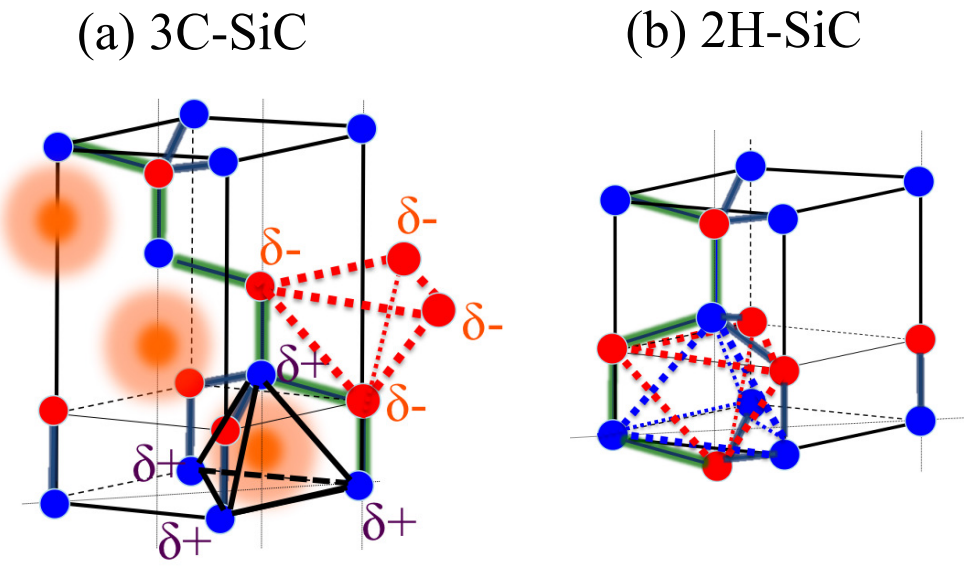

Figure 3.8: Sketches of two tetrahedral (T_d) interstitial sites in the 3C-polytypes (a), and the 2H-polytypes (b): One is surrounded by 4 cations and the other is by 4 anions. The blue balls represent cations, and the red ones anions. In the 3C-polytype (a), the cation-surrounded interstitial site is spatially separated from the anion one. On the other hand, they overlap each other in the 2H-polytype.

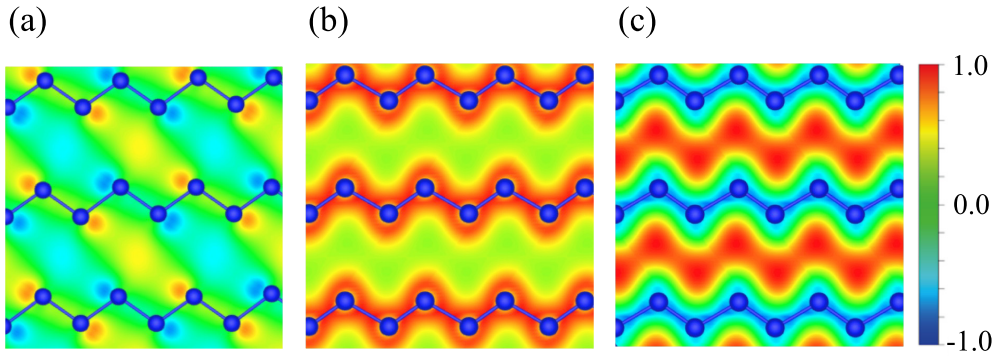

Figure 3.9: Contour plots of the KS orbitals in 3C-Si. (a) Contour plot on (110) plane of the conduction-band minimum at M. The *sp* orbitals mixed with the floating state distributed in ⟨110⟩ channel. (b) Contour plot on (110) plane of the valence-band minimum state at Γ. The state is mainly of *s* bonding character but extends in the interstitial channel region. (c) Contour plot on (110) plane of the conduction-band state at Γ located at 7.81 eV above the valence-band top.

3.3.2 Floating states in $2H$ structure

The floating state at M point in the $3C$-polytypes distributes along the $\langle 110 \rangle$ channel which is slanted relative to [111] direction. In the $2H$ structure, such a slanted channel is absent. Instead, there are channels along $\langle 11\bar{2}0 \rangle$ and $\langle 0001 \rangle$ directions. We find that the CBM at K point in the $2H$ structure floats in the $\langle 11\bar{2}0 \rangle$ channel (Fig. 3.10(a)). This floating state distributes solely in the $\langle 11\bar{2}0 \rangle$ channel with its phase changing consecutively by $\exp(i2\pi/3)$, thus avoiding the atomic sites on (0001) planes. It is also found that the floating state distributes closer to the planes of positively-charged Si atoms to gain the electrostatic energy. The phase change of the floating orbital along this channel is compatible with the symmetry of the Bloch state at K point. Analyses of the KS orbital energies shown in Fig. 3.10(b) clearly show that the energy gain comes from the kinetic- and the Hartree-energy parts. Fig. 3.10(c) shows that the residual norm of the wave function without s- and p-atomic orbitals [Eq. 3.3]. A similar tendency is seen in the figure as that in the $3C$-SiC. It is clearly shown that the valence bands are well described in the linear combination of the atomic s- and p-orbitals. The residual norm of the wave function at the valence-band top is only 0.08. On the other hand, as for the CBM, the residual norm is as much as 0.40. Yet, it is found that the 60% component of the CBM is explained by the atomic orbitals. More detailed discussions are in Sec. 3.5.2. According to the result, the wave function of the CBM at M point has also floating nature; i.e., 0.35.

Diamond polytypes show substantial band-gap decrease in the $2H$ structure, not in the $3C$ structure. We have expected the existence of floating state in them, and have investigated the mechanism. Fig. 3.11(a), (b) and (c) show the KS orbital at the CBM of the $2H$-diamond. The KS orbital also distributes not near atomic sites, but $floats$ in internal space. Fig. 3.11(d) shows the residual norm of wave function after the projection to the s-, and p-atomic orbitals. As much as 0.37 are floating character at the CBM in the $2H$-diamond, while it is only 0.04 at the valence-band top. This fact shows that this KS orbital at the CBM does not consist of atomic orbitals too. The maximum amplitude is at the axis of the $\langle 0001 \rangle$ channels, and the floating state distributes in the horizontal channels. We have found that the floating state induces band-gap variations also in this system. In order to clarify the reason for energy gain of the floating state, we show the energy analyses of KS orbitals at K point in the

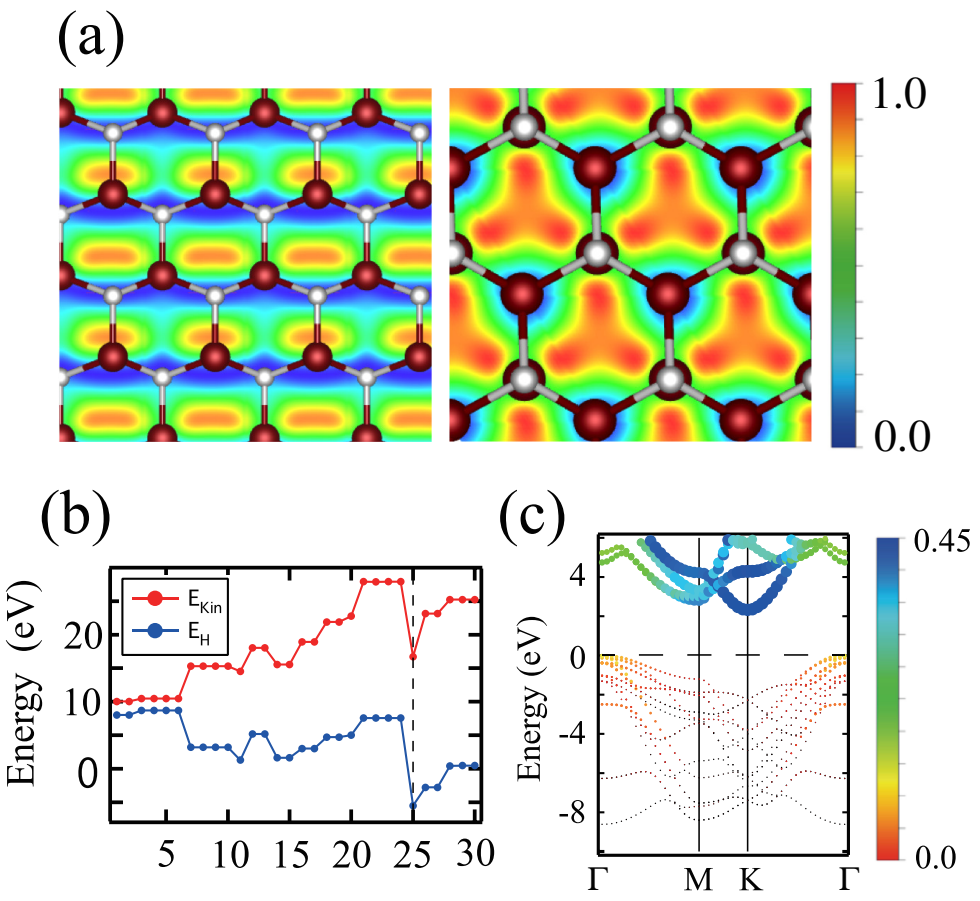

Figure 3.10: Kohn-Sham(KS) orbital of the conduction-band minimum (CBM) at K point of $2H$-SiC. The burgundy and the white balls depict Si and C atoms, respectively. The contour plot of the squared KS orbital on $(1\bar{1}00)$ plane is shown (a). Energy Analyses of KS orbitals in the $2H$-SiC (b). The kinetic-energy contribution $\varepsilon_{\rm kin} = \langle\varphi_i| - \nabla^2/2|\varphi_i\rangle$ and the Hartree-energy contribution $\varepsilon_{\rm H} = \langle\varphi_i| \int \rho(\mathbf{r}')/|\mathbf{r} - \mathbf{r}'|d\mathbf{r}'|\varphi_i\rangle$ to the orbital energy of each KS state for K point in the $2H$-SiC. The abscissa represents the i-th KS state from the valence-band bottom and the 25-th state is the CBM. (c)The residual norm in the $2H$-SiC is represented by the color and the size of the dots. The residual norm is defined as Eq. (3.3) in the text.

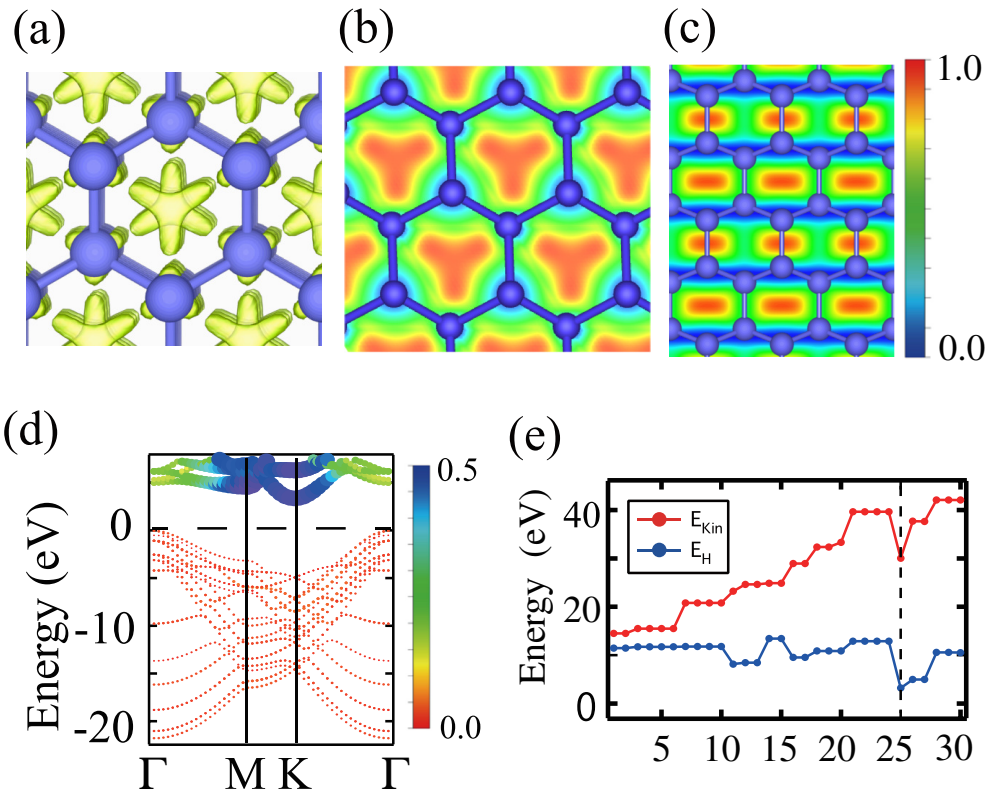

Figure 3.11: Isosurface (a) at its value of 90% of maximum value and contour plots (b)(c) of the calculated Kohn-Sham (KS) orbital at the conduction band minimum at K point in the $2H$-diamond on (0001) and $(1\bar{1}00)$ plane, respectively. The blue balls depict C atoms. (d)The residual norm is represented by the color and the size of the dots. The residual norm is defined as Eq. 3.3 in the text. (e)Energy analyses of KS orbitals in $2H$-diamond. The kinetic-energy contribution ϵ_{kin} and the Hartree-energy contribution ϵ_{H} to the orbital energy of each KS state for K point. The abscissa represents the ith KS state from the valence-band bottom and the 25th state is the conduction-band minimum.

Fig. 3.11(e). According to the figure, there is a similar tendency to that of the $3C$-SiC. Floating state reveals the kinetic energy gain by spreading in the channels broadly. Another energy gain is Coulomb energy gain, because the floating state distributes far from atomic nuclei, where many electrons distribute. In addition, we have found that the electrostatic potential from the ions energy gain plays important roles in the decrease of the energy gap in the $2H$-diamond.

There are structural difference around the interstitial sites between the $3C$ and $2H$ structure. In fact, the interstitial site in $2H$ structure is surrounded by six nearest neighbor atoms, and six next nearest neighbor atoms. In contrast, interstitial site in the $3C$ polytype is surrounded by four nearest neighbor, and three next neighbor atoms. That is, in the $2H$ polytypes, the number of neighbor atoms around the interstitial sites is large compared with other polytypes. This structural difference makes the electro-static potential at the interstitial sites in the $2H$ structure lower than that in the $3C$ by 0.589 eV in diamond. That value corresponds to the band-gap variation in the $2H$ polytype, 0.8 eV. The relation between the number of neighbor atoms and the electro-static potential is discussed in detail in Sec. 4.1.

We then expect that the existence of the floating states is common to the $2H$ polytypes in most covalent semiconductors. We have therefore examined $2H$-SiC, $2H$-AlN, $2H$-BN, $2H$-GaN and $2H$-Si. Fig. 3.12 shows the CBM at K point for them. We clearly see the floating states. In-phase floating state also exists at the CBM of Γ point in $2H$-AlN, and $2H$-GaN [Fig. 3.13]. Due to the stronger ionicity in III-V compound semiconductors, the extension of the KS orbital to the cation sites makes the energy of the CBM at Γ point lower in AlN and GaN. Owing to the competition with the electrostatic energy gain from the cation tetrahedron which makes the energy of the floating state at M-point low, the transition between the direct gap in $2H$ structure and the indirect gap in $3C$ structure takes place for AlN.

3.4 Packing efficiency and floating state

It is thought that there is no space to allow "floating" states in condensed matter. Yet, the appearance of the conduction-band states which float in particular channels in sp^3-bonded materials is a consequence of the existence of the internal space. It is noteworthy that the packing efficiency, p, of the sp^3-bonded structure is 0.34, being extremely small

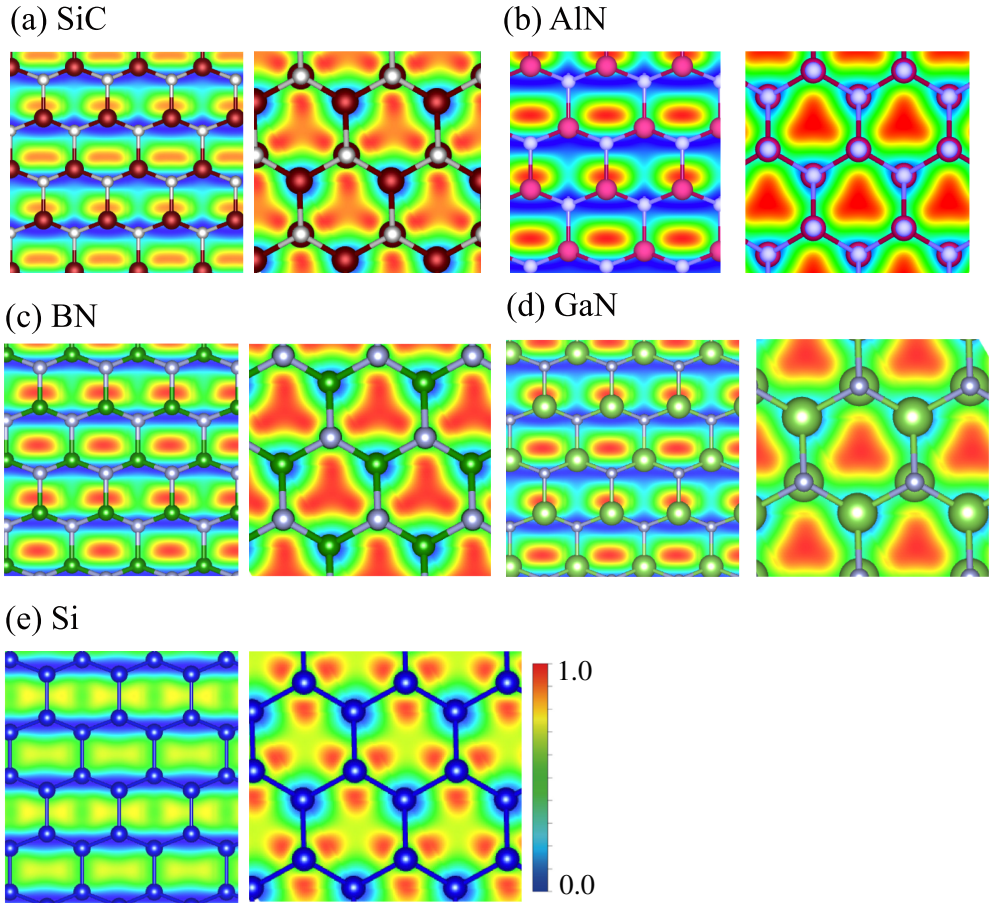

Figure 3.12: Contour plots of the calculated Kohn-Sham(KS) orbitals of the conduction-band minimum at K point for $2H$-SiC (a), $2H$-AlN (b), $2H$-BN (c), $2H$-GaN (d), and $2H$-Si on $(1\bar{1}00)$ (left panel) and (0001) (right panel) plane. In Fig. (a), the brown and white balls depict silicon and carbon atoms, in Fig. (b), the pink and sky blue balls are aluminum and nitrogen atoms, in Fig. (c), green and white balls are boron and nitrogen atoms, in Fig. (d), green and white are gallium and nitrogen atoms, respectively, and in Fig. (e), the blue balls are silicon atoms.

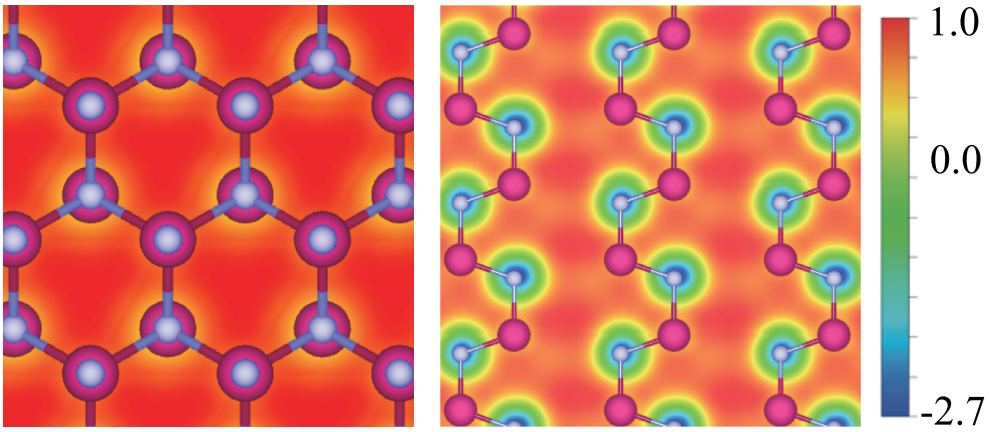

Figure 3.13: Contour plots of the calculated Kohn-Sham(KS) orbital at the conduction-band minimum at Γ point in the 2H-AlN on (0001)(left panel) and (11$\bar{2}$0)(right panel) plane, respectively. The pink and sky blue balls depict aluminum and nitrogen atoms, respectively.

compared with other crystal structures: $p = 0.52$ for simple cubic, $p = 0.68$ for body-centered cubic, $p = 0.74$ for face-centered cubic and p =0.74 for hexagonal close-packed structures, respectively. It has been concluded that the existence of the floating states is common to most sp^3-covalent semiconductors. In addition, the difference in the electro-negativity between the constituent atoms causes particular T_d interstitial sites energetically favorable.

3.5 Comparison with LCAO calculations

The focus of this section is on the capability of describing the floating states by LCAO calculations. LCAO calculation is one of the simplest and most widely used schemes to analyze the electron states. The spirit is based on an idea that electrons generally have their own atomic-orbital characters even in the condensed matter and thus produce various physical and chemical properties. Thus, LCAO calculation uses atomic orbital as a basis function to describe the electron states. Therefore, it is thought that relatively small basis set is enough to provide reasonable results. In sp^3-bonded materials, however, floating state is ubiquitous in conduction bands, as described above. It is nontrivial whether the LCAO calculations describe the floating states or not. We have

investigated the capability of the LCAO calculations in describing the floating nature in this section.

3.5.1 Floating states in $3C$ polytype calculated by LCAO basis sets

We have used OpenMX code to perform LCAO calculations. In the OpenMX code (73, 74), the LCAO basis are generated by introducing a cutoff radius at which the potential well cut the tail of the atomic orbitals. In this scheme, the accuracy of the results is determined by two important parameters: a cutoff radius and the number of basis orbitals. The cutoff radius represents the spread of basis orbitals, which implys a larger cutoff radius and larger number of basis orbitals provide more accurate results. We have performed the LCAO calculations, changing the number of basis orbitals. We have used two kinds of cutoff radii in this work: (i) larger cutoff radii, and (ii) smaller ones. (i) The larger cutoff radii for Si is 4.76 (Å), and for C is 5.29 (Å), (ii) smaller ones for Si is 2.91 (Å), and for C is 2.65 (Å). The number of basis orbitals is the following: (a) the minimum basis set: $3s$, and $3p$ of Si, and $2s$, and $2p$ of C, (b) the more accurate basis set: $3s$, $3p$, and $3d$ of Si, and $2s$, and $2p$ of C, and (c) the most accurate basis set: $3s$, $3p$, $3d$, $4s$, $4p$, $4d$, and $4f$, $5s$, and $5p$ of Si, and $2s$, $2p$, $3s$, $3p$, $3d$, $4s$, and $4p$ of C. Other calculation conditions are the same as those in the plane-wave-basis-set calculations.

Table 3.3 shows the total energies, $E_{\rm tot}$, calculated by the LCAO basis sets. In the LCAO calculations, KS orbitals are expanded by the atomic orbitals, and the total energy behaves under the variation principle. In fact, the convergence of total energy with respect to the number of basis orbitals gives an indicator, representing the calculation accuracy. From the table, larger-cutoff radii and larger number of basis orbitals give more accurate results as we expect.

Fig. 3.14 shows the calculated band structures and KS orbital of the CBM at M point with the larger cutoff radii. From the figures, the valence bands resemble each other, regardless of the number of basis orbitals. In contrast, the conduction bands are changed sensitively depending on the number of basis orbitals.

From the Figure 3.14(a), the CBM shifts upward by 2.01 eV compared with Fig. 3.14(0), indicating the incompleteness of the atomic-orbital basis. The KS orbital at the CBM is quite different from the plane-wave-basis one. It is understood clearly that the orbital in Fig. 3.14(a) consists of the anti-bonding orbitals of carbon-s and silicone-p_z orbitals.

Table 3.3: Total energies, $E_{\rm tot}$, calculated by the LCAO basis sets for 3C-SiC in unit of eV per molecular unit.

Index	basis sets	$E_{\rm tot}$ (eV)
	larger cutoff radii	
(a)	Si-3s, 3p, C-2s, -2p	-269.013
(b)	Si-3s, -3p, -3d, C-2s, -2p	-270.592
(c)	Si-3s, -3p, -3d, -4s, -4p, -4d, -4f, -5s, -5p, C-2s, -2p, -3s, -3p, -3d, -4s, and -4p	-271.142
	smaller cutoff radii	
(a)	Si-3s, 3p, C-2s, -2p	-268.621
(b)	Si-3s, -3p, -3d, C-2s, -2p	-269.157
(c)	Si-3s, -3p, -3d, -4s, -4p, -4d, -4f, -5s, -5p, C-2s, -2p, -3s, -3p, -3d, -4s, and -4p	-271.086

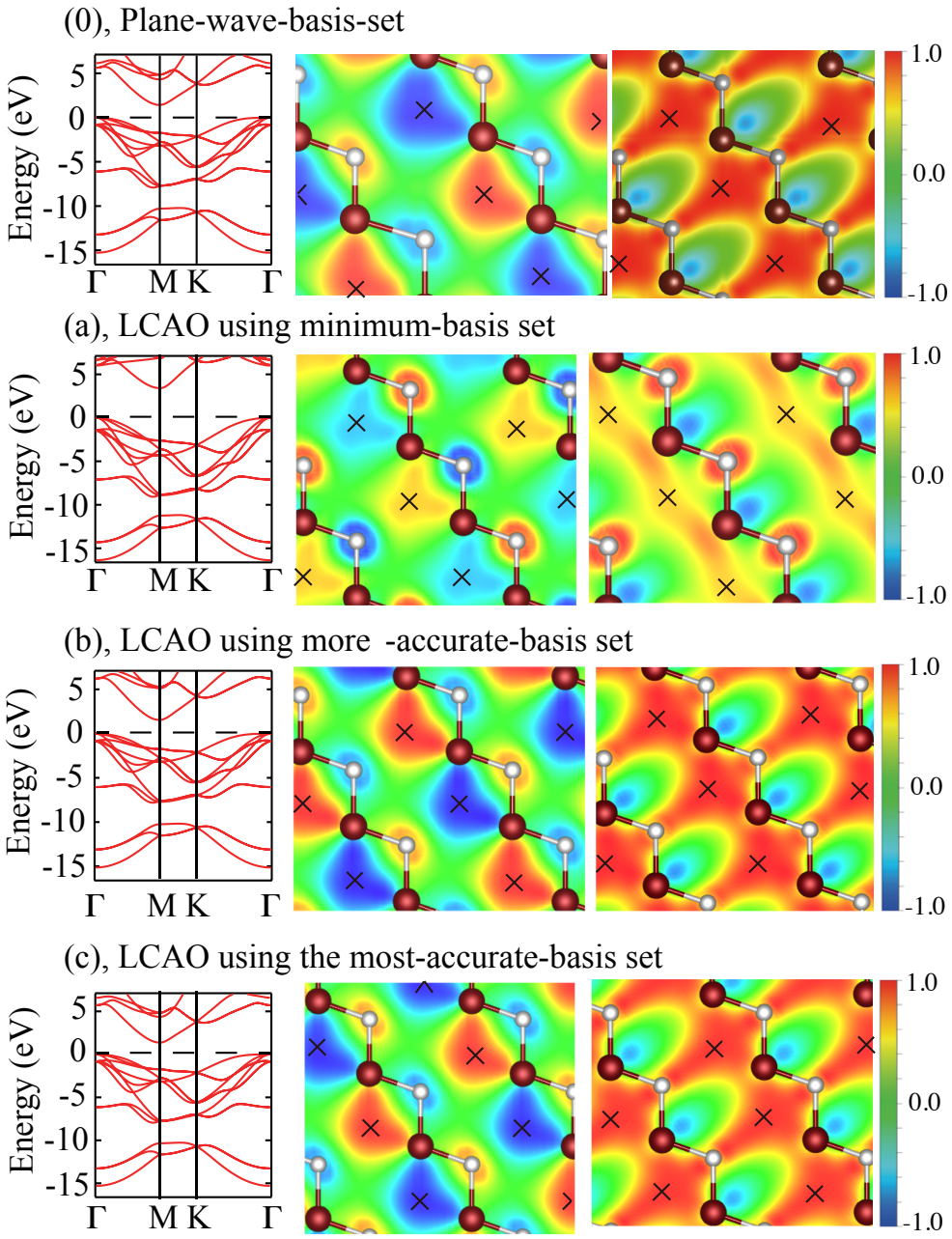

Figure 3.14: Energy bands and the Kohn-Sham(KS) orbitals at the conduction-band minimum of the 3C-SiC by plane-wave-basis set Fig.(0) and by the LCAO basis sets (a)(b)(c) with larger cutoff radii (see text) on $(0\bar{1}1)$ (left) and (110) (right) plane, respectively. The brown and white balls depict Si atoms and C atoms, respectively. The mark 'X' represents the tetrahedral (T_d) interstitial sites surrounded by Si atoms.

The result is consistent with a result by tight-binding model, in which the tail of the p orbitals extend to the interstitial region. The maximum amplitude is, however, at the carbon atomic sites in contrast with Fig. 3.14(0) where the maximum amplitude of the state obtained in the plane-wave-basis set is at the tetrahedral, T_d, interstitial sites. In the LCAO result, the amplitude at the T_d site is 62.3 % of the amplitude at the atomic sites. As mentioned in the Sec.3.3.1, the 66% of the KS orbital at the CBM is atomic orbital component, and the LCAO results seem to resemble the plane-wave-basis one. If we use more extended atomic orbitals as basis functions, then the floating nature may be reproduced.

We also present the LCAO results increasing the number of basis orbitals in Fig. 3.14(b), and (c). The energy gaps in Fig. 3.14(b), (c) are 1.56 eV, and 1.38 eV, respectively. This shows that even the LCAO calculation including Si-3d orbitals as a basis set is still insufficient. The energy level of Si-3d orbital is much higher than that of Si-3p orbital by 8.33eV. The KS orbital at the CBM resembles that by the plane-wave-basis set in (b) and (c). These results reproduce the location of the maximum amplitudes properly. Yet, this shows that we need to use more atomic orbitals as a basis set than our simple expectation, when we perform the LCAO calculations for sp^3-bonded materials.

3.5.2 Floating states in $2H$ polytype calculated by LCAO basis sets

As shown above, floating states exist also in the $2H$ polytypes. Therefore, we have also performed the LCAO calculations for the $2H$-SiC, and the $2H$-diamond with the OpenMX code.

We have performed the LCAO calculations, changing the cutoff radii, and the number of basis orbitals. The cutoff radii used in this work are followings: For the calculations of $2H$-SiC, the same as those of the $3C$-SiC above. For $2H$-diamond, the larger cutoff radius for C is 5.29 (Å), and smaller one for C is 2.65 (Å). The number of basis orbitals is following: (a) the minimum basis set: C-2s, and -2p, (b) the more accurate basis set: C-2s, -2p, -3s, -3p, and -3d, and (c) the most accurate basis set: C-2s, -2p, -3s, -3p, -3d, -4s, -4p, and -4d.

Table 3.4 shows the calculated total energy. It is found that the minimum basis set yields 1.077 (1.222) eV higher total energy in each cutoff radii, compared with the most accurate basis set. For the larger cutoff radii, it is clearly seen that the total energy is improved by using the basis set including more high-energy Si-3d orbitals as a basis

Table 3.4: Total energies, $E_{\rm tot}$, calculated by the LCAO basis sets for 2H-SiC in unit of eV per molecular unit.

Index	basis sets	$E_{\rm tot}$ (eV)
	larger cutoff radii	
(a)	Si-3s, 3p, C-2s, -2p	−134.490
(b)	Si-3s, -3p, -3d, C-2s, -2p	−135.296
(c)	Si-3s, -3p, -3d, -4s, -4p, -4d, -4f, -5s, -5p, C-2s, -2p, -3s, -3p, -3d, -4s, and -4p	−135.567
	smaller cutoff radii	
(a)	Si-3s, 3p, C-2s, -2p	−134.317
(b)	Si-3s, -3p, -3d, C-2s, -2p	−134.601
(c)	Si-3s, -3p, -3d, -4s, -4p, -4d, -4f, -5s, -5p, C-2s, -2p, -3s, -3p, -3d, -4s, and -4p	−135.539

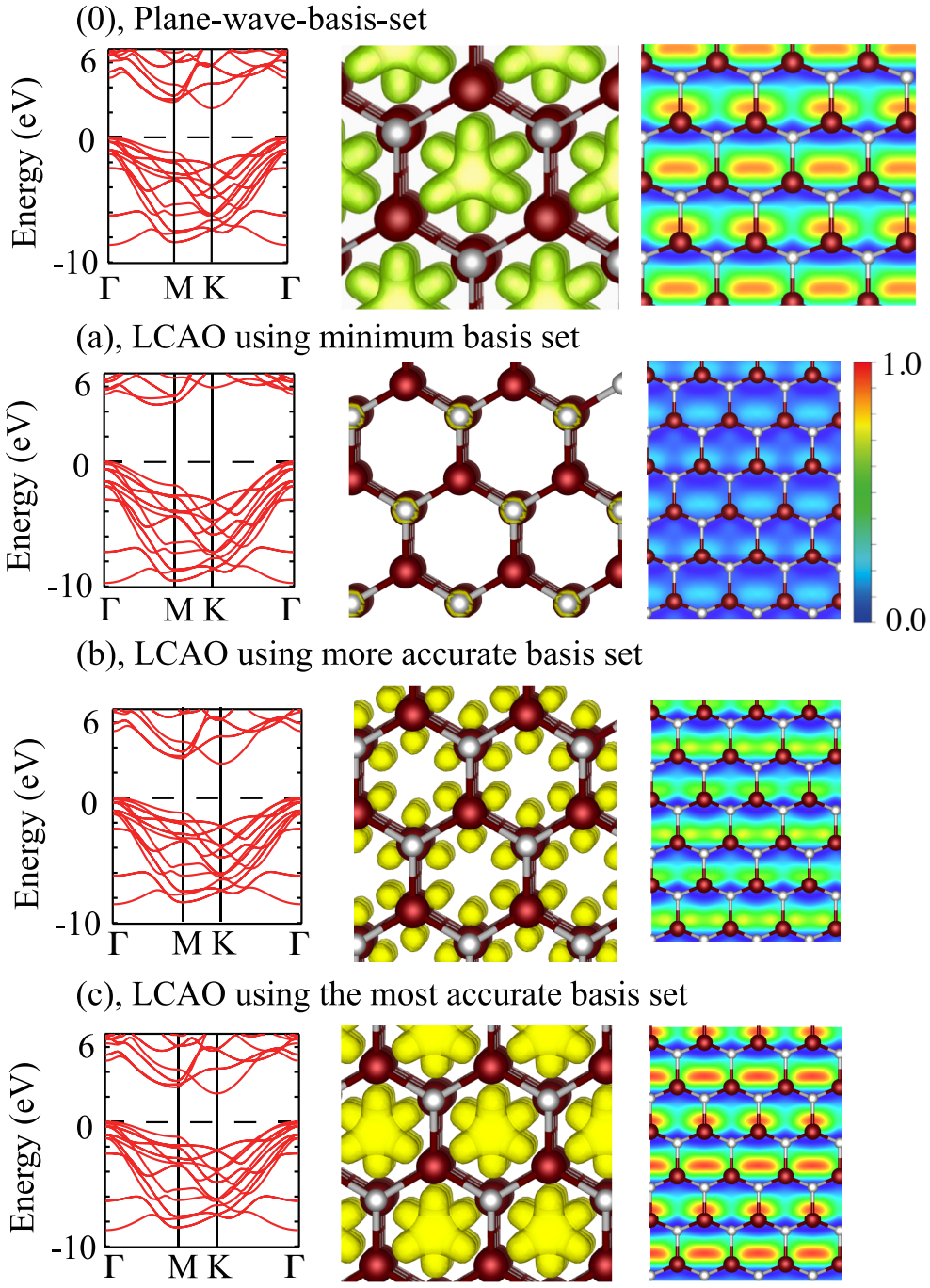

Figure 3.15: Energy bands and squared Kohn-Sham(KS) orbital of the 2H-SiC calculated in the GGA by plane-wave-basis set Fig.(0) and by the LCAO basis sets (a)(b)(c) with larger cutoff radii (see text). In the central panel, isovalue surface of the KS orbital at the conduction-band minimum viewed from the [0001] direction at its value of 80% of the maximum amplitude, and in the right panel, contour plot of the same orbital on the $(1\bar{1}00)$ plane.The brown and white balls depict Si atoms and C atoms, respectively.

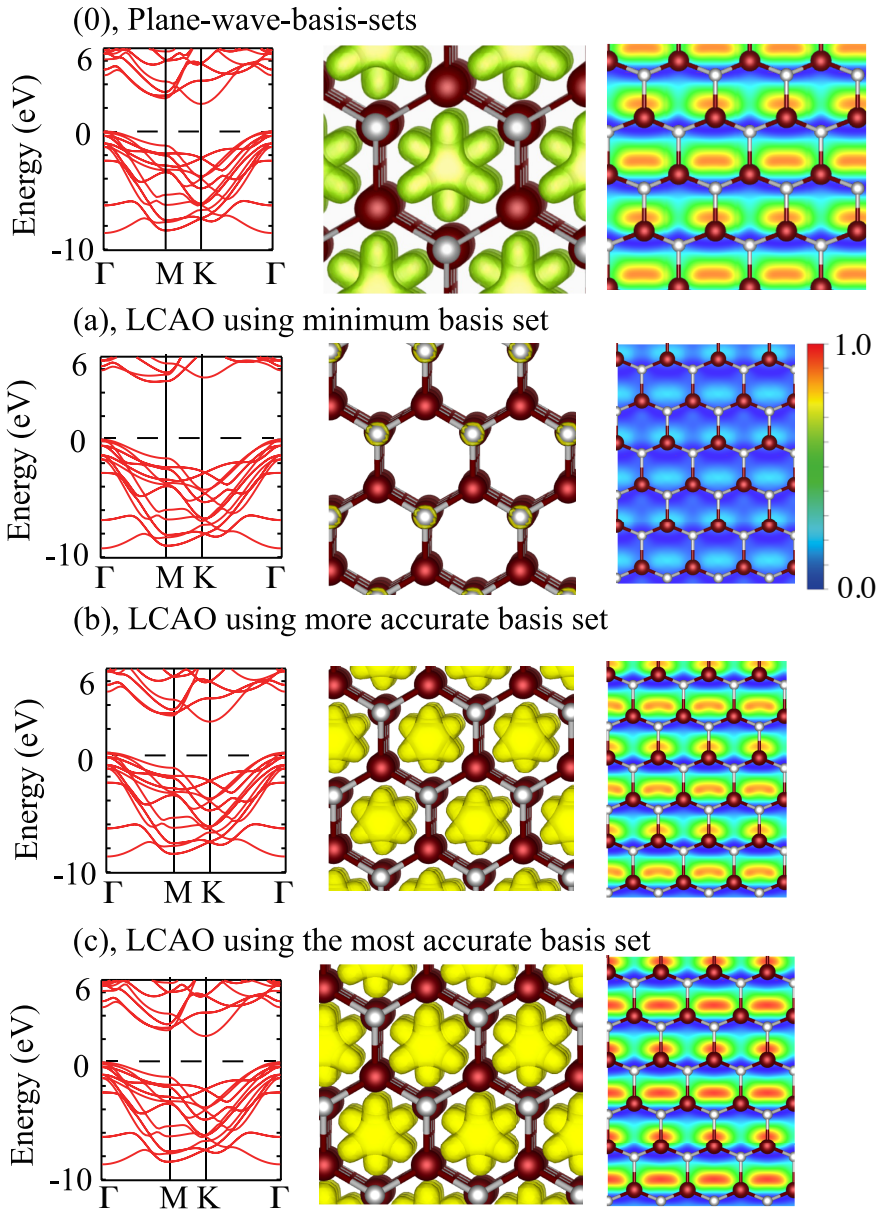

Figure 3.16: Energy bands and squared Kohn-Sham(KS) orbital of the 2H-SiC calculated in the GGA by plane-wave-basis set Fig.(0) and by the LCAO basis sets (a)(b)(c) with smaller cutoff radii (see text). In the central panel, isovalue surface of the KS orbital at the conduction-band minimum viewed from the [0001] direction at its value of 80% of the maximum amplitude, and in the right panel, contour plot of the same orbital on the $(1\bar{1}00)$ plane.The brown and white balls depict Si atoms and C atoms, respectively.

set. On the other hand, as for the smaller cutoff basis set, including the Si-3d orbitals as a basis set is still poor to describe the total energy, i.e., 0.938 eV higher than the most accurate basis set.

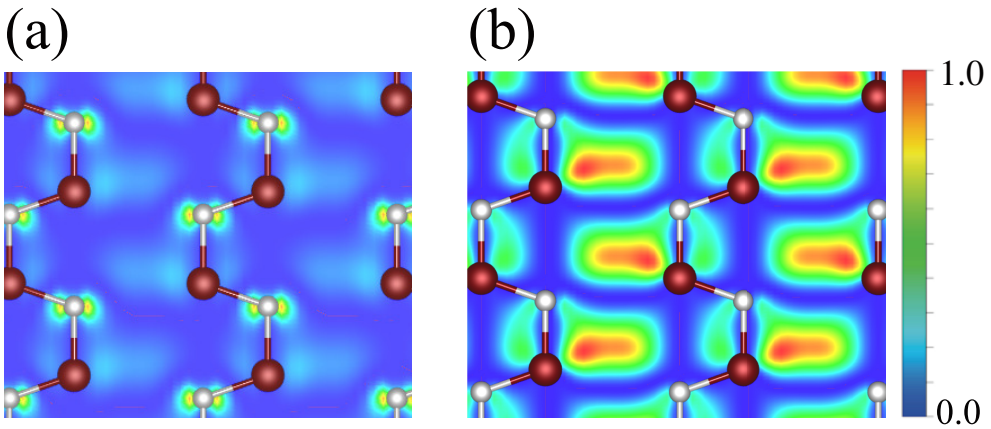

Figure 3.17: Contour plots of squared Kohn-Sham(KS) orbitals of the 2H-SiC by LCAO basis sets (a) with larger cutoff radii, and by plane-wave-basis set (b). In theses panels, contour plots of the squared KS orbital at the conduction-band minimum on the $(11\bar{2}0)$ plane. The brown and white balls depict Si atoms and C atoms, respectively.

Fig. 3.15 shows the calculated band structures using the larger cutoff radii, and Fig. 3.16 using the smaller cutoff radii. For the larger cutoff radii, it is found that valence bands resemble each other. On the other hand, as for the minimum basis set (Fig. 3.15(a)), qualitative features of the conduction bands are substantially different from those obtained with the plane-wave basis set as shown in Fig. 3.15(0): The CBM is at some point between Γ and M in the LCAO basis, whereas it is at K point in the plane-wave basis. The band gap in the LCAO is 2.207 eV higher than that by the plane-wave-basis set. The floating nature of the state which is clearly shown in the center and right panels of Fig. 3.15(0) obtained in the plane-wave-basis-set calculations are totally lacking in this LCAO-basis-set calculations. In a tight-binding model, the conduction-band bottom at K point is the anti-bonding state of p orbitals extending in the (0001) plane. The squared KS orbitals shown in the center and right panels of (a) are in accord with this picture. The wave function at lowest-conduction band at K point has the maximum amplitude at the carbon sites, showing no floating character. This atomic-orbital nature is clearly seen in Fig. 3.17 where the contour plots of the

same orbital on the $(11\bar{2}00)$ plane obtained in LCAO calculations are shown. In the LCAO calculations, the CBM consists of 57.4 % of Si-3p, and 42.5 % of C-2p. On the other hand, the floating state distributes closer to the planes of positively-charged Si atoms to gain the electrostatic energy [Fig. 3.17(b)].

Even if we include the Si-3d atomic orbitals as a basis set (b), the band gap is 3.134 eV, much larger by 0.779 eV. The KS orbital at the CBM at K point extends to the interstitial sites to some extent, but still the maximum amplitude is at atomic sites, silicon sites. Using the most accurate basis set (c), it is found that the wave function looks like the plane-wave one. It is found that floating nature is quite difficult to produce by the conventional LCAO calculation. The band gap is 2.34 eV, in good agreement with the value by the plane-wave-basis set, 2.355 eV. In the case of smaller cutoff radii, the minimum basis set is poor to describe the band structure as well. The band gap is 4.923 eV, much larger than that using the plane-wave-basis set, 2.355 eV. For the basis set (b), the KS orbitals seem to have the floating character, but their band gaps are 3.115 eV, still larger than that calculated by plane-wave-basis set, 2.355 eV. The band gap calculated by the LCAO using the most accurate basis set shows 2.26 eV, which accords with that by plane-wave-basis set. We have found that when we use extremely high-energy atomic orbitals as a basis set, the LCAO calculations reproduce the floating nature. This fact clearly shows that we should go beyond the conventional LCAO picture to reproduce the floating nature.

Furthermore, we have performed LCAO calculations for 2H-diamond. Table 3.5 shows the total energies, $E_{\rm tot}$, calculated by the LCAO basis sets. From the table, larger-cutoff radii and larger number of basis orbitals give more accurate results.

Fig. 3.18 shows the calculated band structures and KS orbitals of the CBM at K point with the larger cutoff radii. From the figures, the valence bands resemble each other, regardless of the number of basis orbitals. In contrast, the conduction bands are changed sensitively depending on the number of basis orbitals.

From the Figure 3.18(a), the CBM is at Γ point, thus showing a direct-gap semiconductor. This result qualitatively contradicts with that of plane-wave-basis set, where this system is a indirect-gap semiconductor. Its band gap is 6.02 eV, which is higher than that of plane-wave-basis set by 2.61 eV, indicating the incompleteness of the atomic-orbital basis. The KS orbital at the CBM has no floating nature. It is understood clearly that the orbital consists of the anti-bonding orbitals of carbon-p or-

Table 3.5: Calculated total energies, $E_{\rm tot}$, calculated by the LCAO basis sets for the $2H$-diamond in unit of eV per molecular unit.

Index	basis sets	$E_{\rm tot}$ (eV)
	larger cutoff radii	
(a)	C-2s, -2p	-316.659
(b)	C-2s, -2p, -3s, -3p, -3d	-317.573
(c)	C-2s, -2p, -3s, -3p, -3d, -4s, -4p, -4d	-317.726
	smaller cutoff radii	
(a)	C-2s, -2p	-314.744
(b)	C-2s, -2p, -3s, -3p, -3d	-317.635
(c)	C-2s, -2p, -3s, -3p, -3d, -4s, -4p, -4d	-317.691

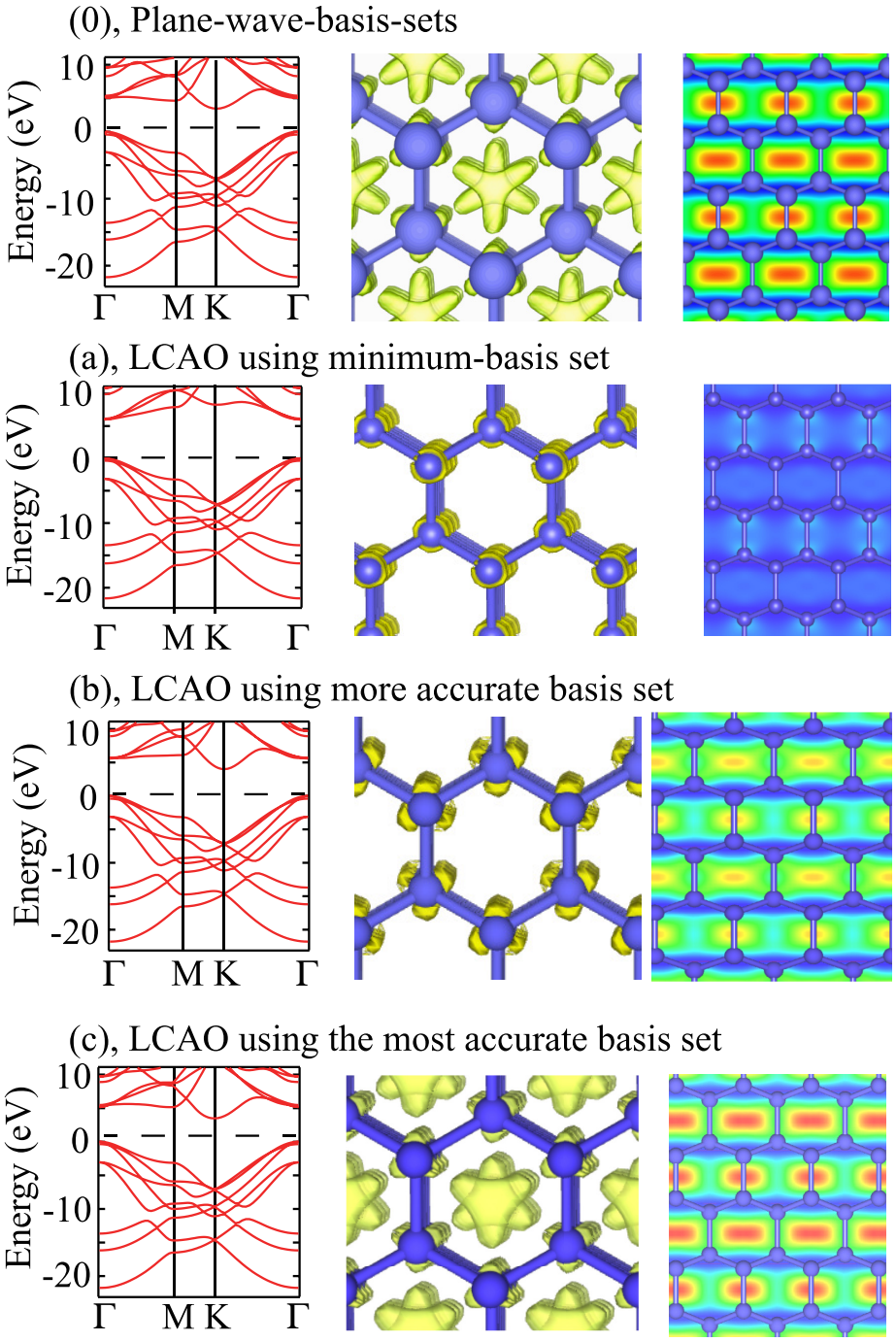

Figure 3.18: Energy bands and squared Kohn-Sham(KS) orbital of the $2H$-diamond calculated in the GGA by plane-wave-basis set Fig.(0) and by the LCAO basis sets (a)(b)(c) with larger cutoff radii (see text). In the central panel, isovalue surface of the KS orbital at the conduction-band minimum viewed from the [0001] direction at its value of 90% of the maximum amplitude, and in the right panel, contour plot of the same orbital on the $(1\bar{1}00)$ plane. The blue balls depict C atoms.

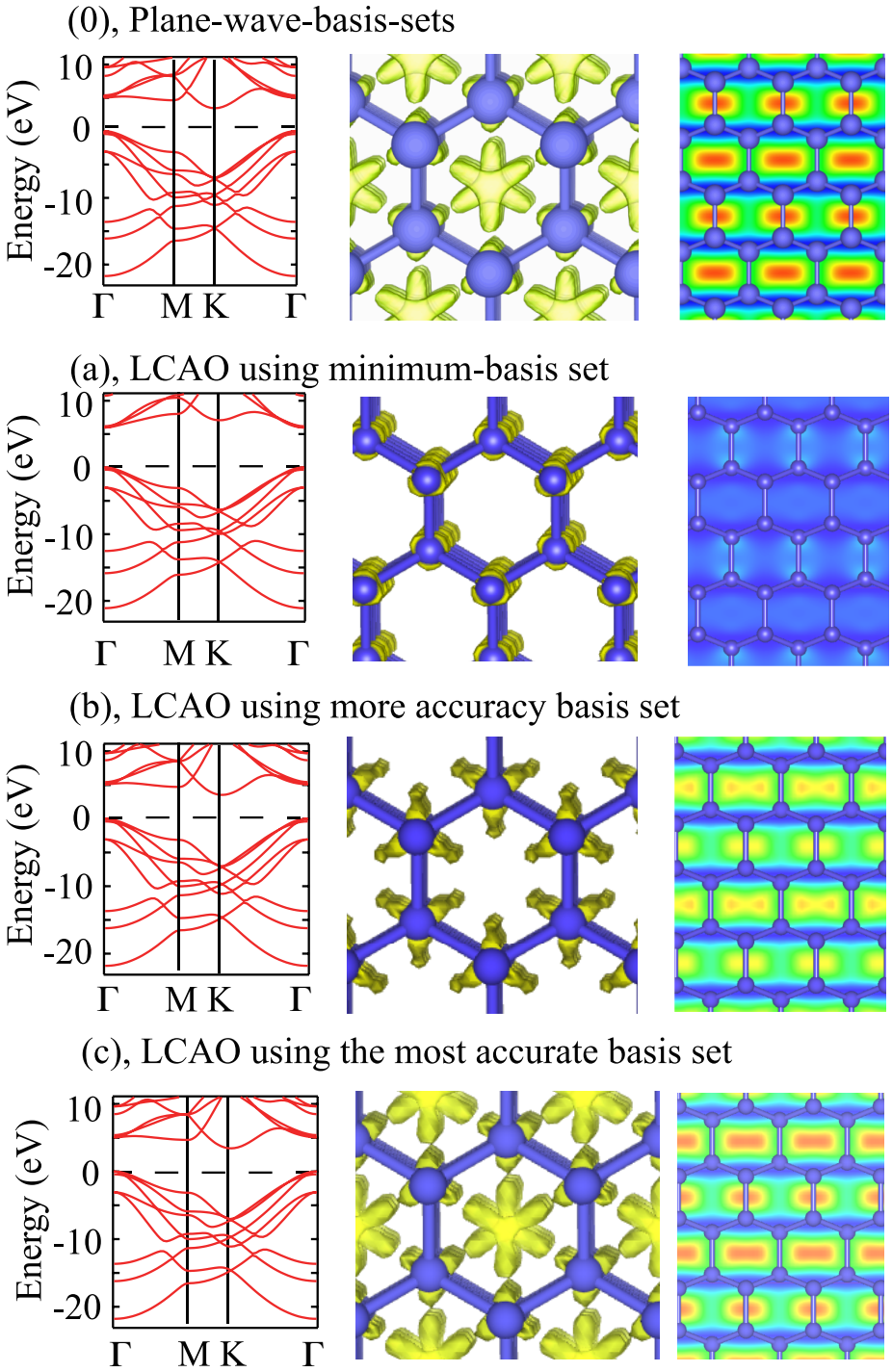

Figure 3.19: Energy bands and squared Kohn-Sham(KS) orbital of the $2H$-diamond calculated in the GGA by plane-wave-basis set Fig.(0) and by the LCAO basis sets (a)(b)(c) with smaller cutoff radii (see text). In the central panel, isovalue surface of the KS orbital at the conduction-band minimum viewed from the [0001] direction at its value of 90% of the maximum amplitude, and in the right panel, contour plot of the same orbital on the $(1\bar{1}00)$ plane. The blue balls depict C atoms.

bitals. Indeed, the maximum amplitude is at the carbon atomic sites in contrast with Fig. 3.18(0) where the maximum amplitude of the state obtained in the plane-wave-basis set is at the axis of the $\langle 0001 \rangle$ (vertical to the a, b-plane) channels. In the LCAO result, the amplitude at the axis of the $\langle 0001 \rangle$ channels is only 7 % of the amplitude at the atomic sites. In addition, this result is consistent with that of tight-binding model.

We also present the LCAO results with increasing the number of basis orbitals in Figs. 3.18(b), and (c). The energy gaps in Fig. 3.18(b), (c) are 4.01 eV, and 3.49 eV, respectively. In the calculation (b), we use carbon-3s, -3p, and -3d orbitals as a basis set in addition to basis set(a), which are energetically higher state than carbon-2p orbitals by 8.48 eV, is still inadequate to describe the conduction bands. The maximum amplitude is still at carbon sites, and shows floating nature a little. The amplitude at the axis of the vertical channels is 78 % of the atomic sites. In the calculation (c), we sum up with atomic orbitals higher 14.16 eV than C-2p orbitals. The results seem to show floating nature of KS orbital. The maximum amplitude is at the axis, thus reproducing the band-gap variations in LCAO calculations.

From the analysis of the component of the wave function in the LCAO calculation, the CBM at K point consists 61.4% of carbon-3d, and 12.6 % of carbon-4d orbitals. It's noteworthy that total percentages of the components of carbon-3s, 3p, 4s, 4p is only 4.6 %. The unnatural fillings are remarkable. To describe the conduction bands in sp^3-bonded materials, we need more basis orbitals than those usually thought to be enough. We have also performed the LCAO calculations with small cutoff radii, in Fig. 3.19. The results show little difference from that of the larger cutoff ones. From the results, we have found the LCAO calculations are difficult to reproduce the floating nature, regardless of the spread of the basis orbitals.

3.6 Intercalated systems

In most cases, floating sate exists in the conduction electron states. Yet, the DFT is not verified in application to the unoccupied electron states. We then have performed electronic-structure calculations for electron-doped SiC polytypes. The doped electrons are thought to occupy the floating sate at the CBM. We have doped 1.59×10^{21} [cm^{-3}] per the 6 pairs of SiC molecule units. First, we have optimized the lattice constants in the hexagonal plane and along the stacking direction, a and c. For the doped 3C-SiC,

the lattice constant a indicates only 0.38 % increase over that of the intrinsic $3C$-SiC. Moreover, the lattice constant a (c) of the doped $2H$-SiC is increased only 0.49 % (0.354%). From these results, the lattice constants are almost unchanged in electron doping.

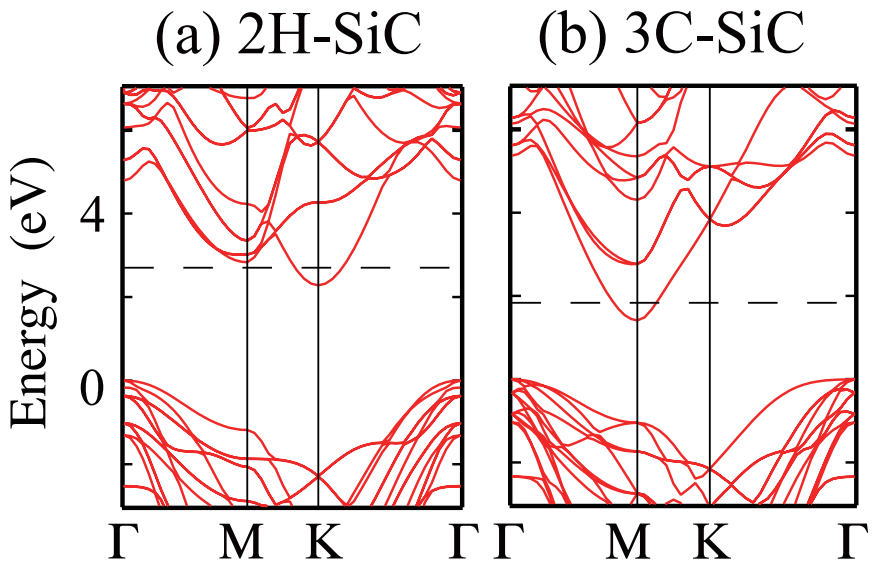

Figure 3.20: Calculated band structures of the electron-doped $2H$-SiC (a) and $3C$-SiC (b). The broken line represents the Fermi energy.

Fig. 3.20 shows the calculated band structures. We have found that the band structures are understood completely by the rigid band model. The KS orbital at the occupied CBM is shown in the Fig. 3.21. The orbitals clearly manifest the floating character. We have found the electron carriers have floating nature in n-doped SiC semiconductors.

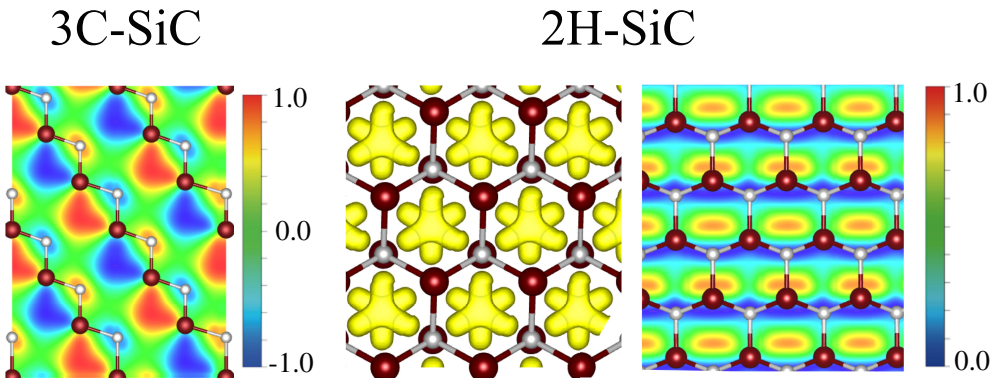

Figure 3.21: Contour plot at the conduction-band minimum (CBM) of the electron-doped $3C$-SiC (left panel), and isosurface and contour plot at the CBM of the $2H$-SiC (right panel). The isosurface of the orbital is its 80 % value of the maximum amplitude.

4

Electrostatic potential in internal space

4.1 Multipole decomposition of electrostatic potential

From the chapter. 3, we have found that floating states are ubiquitous in sp^3-bonded materials. The floating nature is a consequence of the existence of the internal space in the materials. In most covalent semiconductors, the floating states appear at the conduction-band minima whose energy level is lower than the vacuum level: e.g., the vacuum level is higher than the conduction-band minimum (CBM) in the $6H$-SiC by 3.0 eV in the experiment (130). Here one question arises: why the energy level of floating state is lower than the vacuum level? It means that the electrostatic potential in the internal space should be lower than vacuum level substantially. However, the core- and valence-electron cloud distributes near the nucleus, and screens the attractive potential from the nucleus. Due to the Gauss's theorem, the electro-static potential far from the nucleus seems to decay exponentially. Therefore, the electrostatic potential at interstitial sites is thought to not to be so lower than the vacuum level. This expectation looks conflicted with the existence of the floating state at the CBM.

In order to clarify this apparent contradiction, we have first plotted the electro-static potential of an isolated Si atom (Fig. 4.1 (a)). First, it is clearly seen that the electro-static potential from the nucleus and occupied electrons has a spherical symmetry, because the electron distribution has also spherical symmetry in the case of an isolated atom. The electro-static potential at the distance of 1.9 Å from the nucleus

is only -0.6 eV, where the distance of 1.9 Å is the distance between the Si atom and the interstitial site in the $3C$-SiC. In the $3C$-SiC, the tetrahedral interstitial site is surrounded by 4 Si atoms. Therefore, we estimate the electro-static potential at the interstitial site to be $-0.6 \times 4 = -2.4$ eV at most, based on the analysis of the isolated atom. Its absolute value is too small to explain the appearance of the floating state at the level of the 3.0 eV below the vacuum state.

Yet in sp^3-bonded materials, each atom forms four bonds with its neighbors located with tetrahedral symmetry. Hence the electrostatic potential is certainly non-spherical. To mimic the situation, we adopt a simple model in which a point charge of $+4$ is surrounded by four -1 point charges located with tetrahedral symmetry, as shown in Fig. 4.1 (b1). The former charge corresponds to the charge distribution of Si nucleus and core electrons, whereas the latter charge corresponds to valence-electron bond charges. The distance between the positive and the negative charge is set to be a half of the bond length. As is clearly seen in the Fig. 4.1 (b2), the electro-static potential is non-spherical, and the negative part of the potential expands to the tetrahedral interstitial sites, which is marked by the red squares. Thus, the non-spherical-charge distribution makes the potential at the interstitial sites lower, showing the electro-static potential at the interstitial sites 2 eV lower than the vacuum level. By considering that the interstitial sites are surrounded by 4 atoms in the $3C$-SiC, we have estimated the electrostatic potential at the interstitial site to be $2 \times 4 = 8.0$ eV lower than the vacuum level. Significant lowering takes place. This estimated value is roughly consistent with the effective potential in the DFT calculation of the $3C$-SiC: -12.3167 (-9.757) eV at the interstitial sites surrounded by Si (C) atoms. We have found that non-spherical-electron distribution plays important roles in the appearance of the floating state at the CBM. Here we have neglected the effects of the charge transfer in the $3C$-SiC for simplicity.

Next, we discuss the substantial band-gap variation in the $2H$-diamond. In the case of diamond, drastic decrease of 0.84 eV occurs in the $2H$ polytype: i.e. the band gap in the $3C$-diamond is 4.246 eV, while that in the $2H$-diamond is 3.406 eV. As mentioned in the Sec. 3.3.2, the energy-gap variation comes from the structural difference around the interstitial sites between the $3C$ and $2H$ structures: i.e., each interstitial site in the $2H$ structure is surrounded by six nearest neighbor (NN) atoms, and six next NN atoms, and that in the $3C$ polytype is surrounded by four NN, and three next NN atoms.

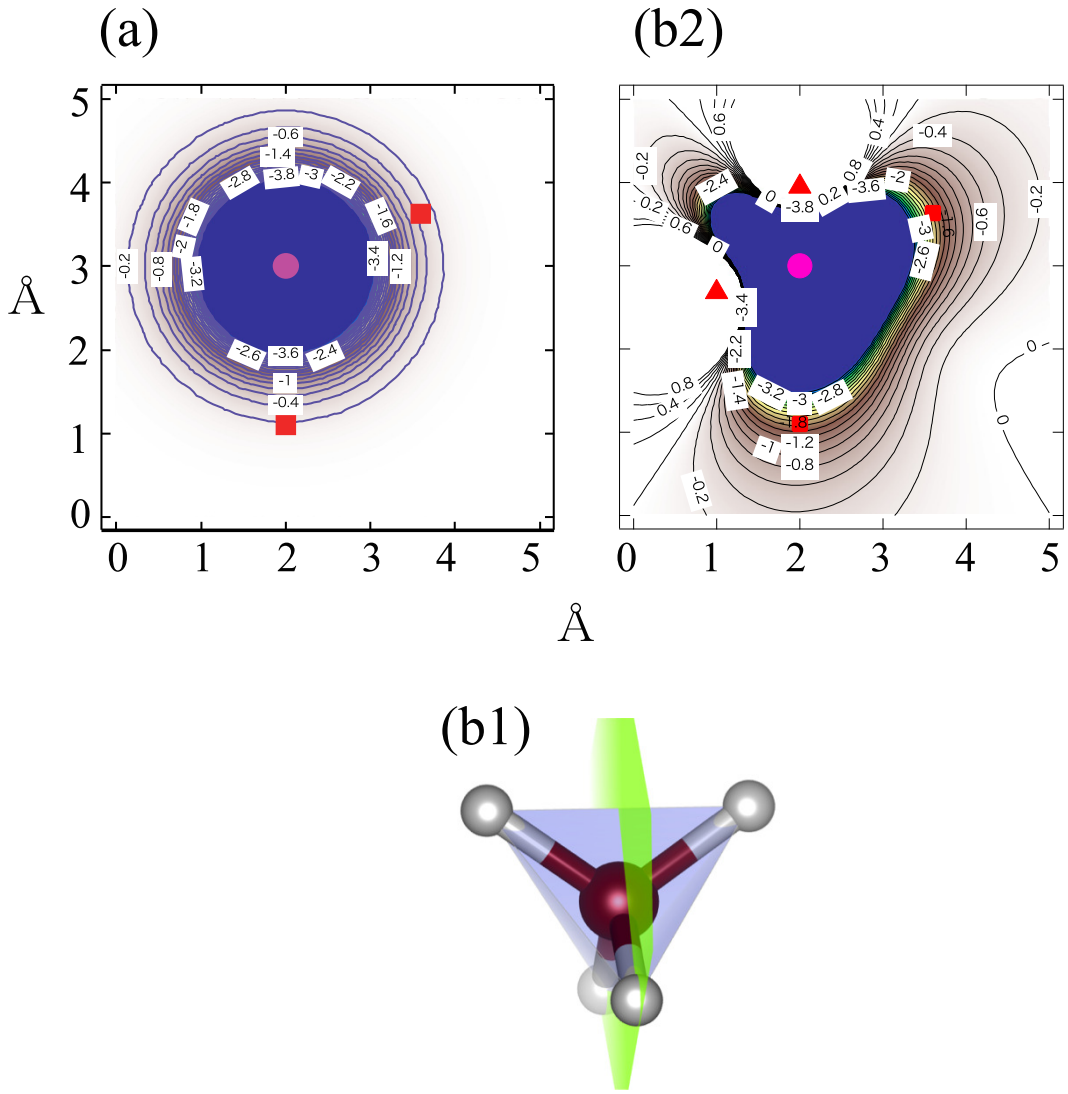

Figure 4.1: Isovalue plots of Coulomb potential from a nucleus and electrons for an isolated silicon atom (a). In (a), the positions of the Si ion and the interstitial sites are represented by a pink dot and red squares. It is apparent that valence electrons distributes around the ion with spherical symmetry, and thus showing spherical-symmetric electrostatic potential. However, in real sp^3-bonded systems, electrons don't distribute around the nucleus with spherical symmetry. Therefore, we consider a more realistic model, which mimics the sp^3-nonspherical electron distribution, to analyze the electrostatic potential at the interstitial sites. In the model, Si ion is replaced by a +4 point charge, and four valence electrons by -1 point charge. Four electrons are located with tetrahedral symmetry, representing valence-electron bond charges. A cutting plane, represented by green plane (b1), and isovalue plots of Coulomb potential from Si ion and four electrons on that plane (b2). In (b2), the positions of the Si ion and the valence electrons are represented by a pink dot and red triangles, respectively. Red squares depict the positions of interstitial sites.

Table 4.1: Structural difference around the interstitial between the $3C$-diamond and the $2H$-diamond. The Kohn-Sham (KS) effective potential at the interstitial site in the DFT calculation is also listed. The electro-static potential of the interstitial site from the nearest neighbor (NN) atoms is calculated by two model, isolated model and sp^3 model (See the text).

	$3C$-diamond	$2H$-diamond
Band gap (eV)	4.246	3.406
Number of nearest neighbor (NN) atoms	4	6
Distance between the NN and interstitial site (Å)	1.540	1.641
Number of 2nd NN atoms	4	6
Distance between the 2nd NN and interstitial site (Å)	1.778	1.943
Effective potential at the interstitial site in the DFT (eV)	−12.349	−12.938
Electro-static potential calculated by the isolated atom model (eV)	−2.456	−2.700
Electro-static potential calculated by the sp^3 model (eV)	−9.061	−10.979

These structural difference causes the electro-static potential at the interstitial sites in the $2H$ structure lower than that in the $3C$ by $-12.349-(-12.938)=0.589$ eV, which corresponds to the band-gap variation in the $2H$ polytype, 0.8 eV [See Table. 4.1].

From the analysis of the isolated carbon atom, the electro-static potential at the distance of 1.54Å, which corresponds to the distance between the interstitial site and the NN atom in the $3C$-diamond, is estimated to be -0.614 eV. Therefore, electro-static potential at the interstitial site is calculated to be $-0.614\times 4=-2.4564$ eV. On the other hand, the potential at the distance of 1.64 Å from the nucleus, which represents the distance between the interstitial site and NN atom in the $2H$-diamond, is -0.450 eV. In the same way as in the $3C$-dimaond, electro-static potential at the interstitial site is $-0.450\times 6=-2.700$ eV, which is lower than that in the $3C$-diamond by 0.245 eV. From the rough estimation, it has been clarified that the potential difference of the two polytypes at the interstitial site comes from its difference in surrounding environments.

The relative difference of the electro-static potential has succeeded to be explained by the above model. The absolute value of the potential, however, is too small, compared with the effective potential in the DFT calculation: the potential at the interstitial site is -12.349 eV in the $3C$ polytype and -12.938 eV in the $2H$. We have calculated the potential again using the sp^3 model. The electro-static potential at the distance of 1.54 (1.64) Å from the nucleus is -2.265 (-1.830) eV, respectively. The estimated potential at the interstitial site is $-2.265\times 4=-9.061$ eV in the $3C$ polytype, and $-1.830\times 6=-10.979$ eV in the $2H$, which are much lower than those in the isolated atom model. The potential at the $2H$ polytype is 1.918 eV lower than that in the $3C$. We have found that non-spherical electron distribution plays important roles in the effective potential.

From both models, it has been clarified that the potential at the interstitial site in the $2H$ is lower than that in the $3C$, because of the difference of the surrounding environments. In addition, we have found that the much lower potential than the vacuum level comes from the non-spherical electron distribution.

4.2 Pressure effects on floating states

In this section, we examine the pressure dependence of floating states. We have focused on the response of the floating state to the isotropic pressure, and we don't consider the

possibility of the structural transition derived from the pressure. First, consider the behavior of the electronic band structures, based on the conventional atomic-orbital picture. Under the pressurized circumstances, atoms are closer to each other, thus making stronger bonds. This fact leads to larger energy gap between the bonding and anti-bonding orbitals. For example, consider the two-site tight-binding model with hopping t. The energy gap is estimated to be $2t$, and each band width is also $2t$. This simple model predicts that the energy gap and the band width become larger with increasing the pressure.

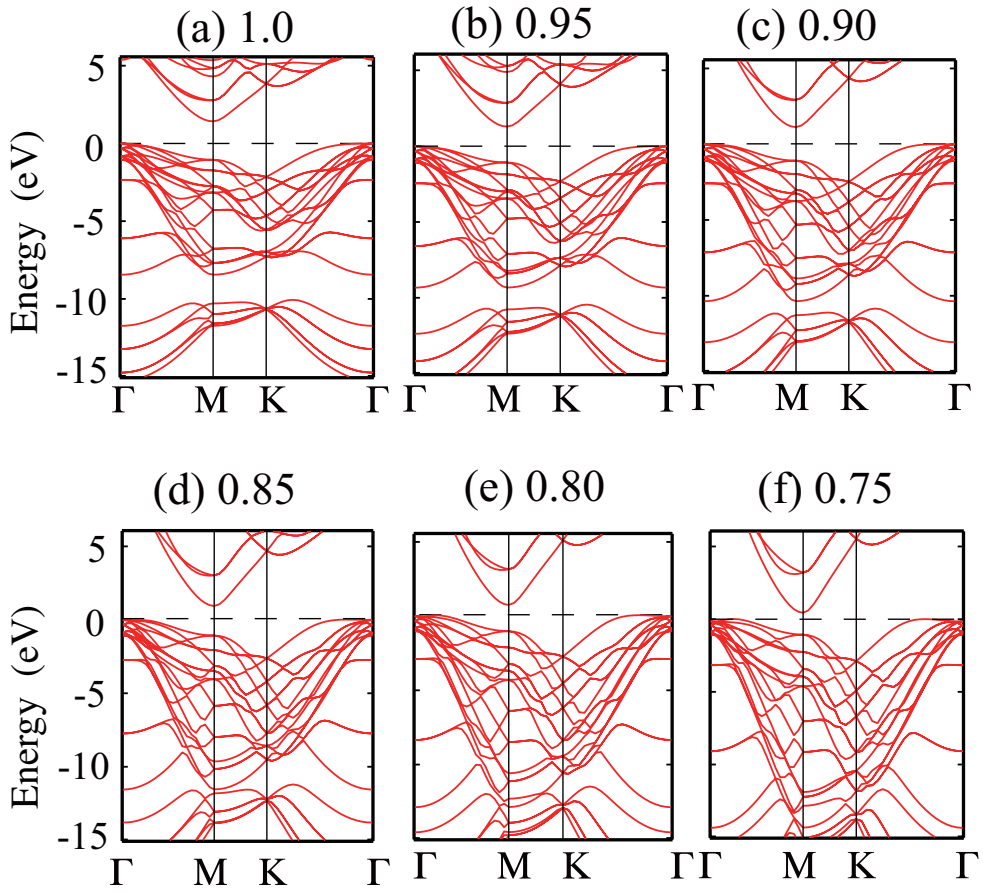

Figure 4.2: Calculated band structures of the 3C-SiC under the pressurized circumstances. Each band structure shows the electron bands with lattice constant scaled from 1.0 to 0.75 with respect to the values in the Table. 3.1. The energy of the valence-band top is set 0. The corresponding pressures are followings: 0 (GPa) for (a), 31.0 (GPa) for (b), 73.7 (GPa) for (c), 128.7 (GPa) for (d), 202.6 (GPa) for (e), and 306.5 (GPa) for (f).

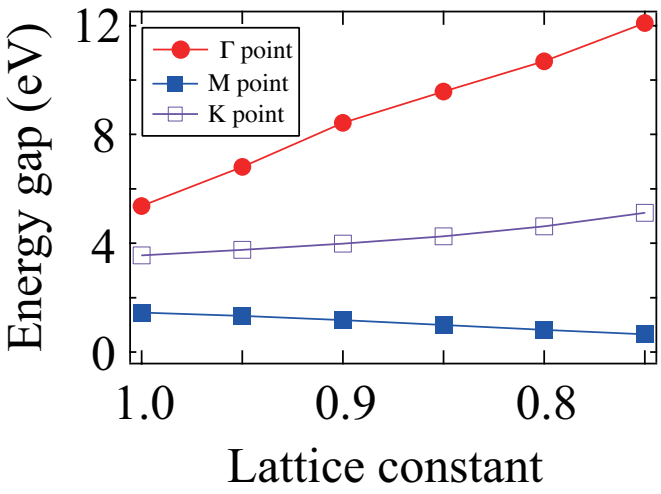

Figure 4.3: Calculated energy levels of the 3C-SiC at several k points with scaling lattice constants. The corresponding pressures are followings: 0 (GPa) for $a = a_0$, 31.0 (GPa) for $a = 0.95a_0$, 73.7 (GPa) for $a = 0.9a_0$, 128.7 (GPa) for $a = 0.85a_0$, 202.6 (GPa) for $a = 0.80a_0$, and 306.5 (GPa) for $a = 0.75a_0$.

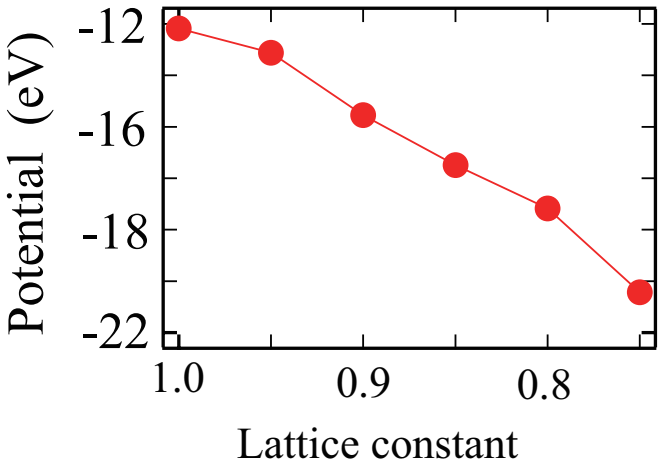

Figure 4.4: Calculated potential energy at the interstitial site of the 3C-SiC with scaling lattice constants. The corresponding pressures are followings: 0 (GPa) for $a = a_0$, 31.0 (GPa) for $a = 0.95a_0$, 73.7 (GPa) for $a = 0.9a_0$, 128.7 (GPa) for $a = 0.85a_0$, 202.6 (GPa) for $a = 0.80a_0$, and 306.5 (GPa) for $a = 0.75a_0$.

Fig. 4.2 shows the calculated band structures of the $3C$-SiC with reducing the lattice constant to 75 % with respect to the values of the Table. 3.1 with 5 % increments. First, it has been found that the band widths of the valence bands get larger with increasing the pressure. The valence-band width in the $a = 0.75a_0$ is 14.358 eV, which is 1.70 times larger than that in the $a = a_0$. This tendency is consistent with what we consider. Yet, it is noteworthy that the band gaps behave in quite different way from the simple consideration. As is clearly seen, the energy level at the CBM shifts downwards, showing narrower band gaps. Fig. 4.3 shows the calculated energy gaps with respect to the valence band top for several high-symmetrical k points. In particular, it has been found that the behavior of the CBM at M point is peculiar than that of other k points. This is thought to be due to the potential energy gain at the interstitial sites. The interstitial sites come closer to the nucleus under the pressurized condition, and the potential at the interstitial sites is lower and lower, as is expected from the Fig. 4.1(b). In fact, Fig. 4.4 shows the electro-static potential at the interstitial sites, and thus potential-energy gain is apparent. Therefore, it is clear that potential-energy gain causes the floating sates shift downwards, thus showing smaller band gaps.

In the $2H$-SiC, the CBM is located at K point, and the wave function manifests the floating character. It is clear also in this case that valence-band width with lattice constant scaled by 0.75 is 14.617 eV, which is 1.70 times larger than that with $a = a_0$(Fig. 4.5). We have found the energy shift of the floating state also in the pressurized $2H$-SiC. Fig. 4.6 and Fig. 4.7 show the energy levels and potential energy at the interstitial site of the $2H$-SiC, thus showing similar behaviors as those in the $3C$-SiC.

We then expect that the energy-level shift of the floating state is common to other polytypes. Here we show some examples: $3C$-GaAs and $2H$-diamond. $3C$-GaAs is a III-V semiconductor, and has a direct band gap, 1.43 eV. GaAs is widely used in the manufacture of devices such as microwave frequency integrated circuits, monolithic microwave integrated circuits, laser diodes, solar cells and optical windows. Yet, the difference in the electro-negativity of component atoms of GaAs is relatively small: That of gallium is 1.81, and arsenic 2.18. This fact does not lead to appearance of floating state at the CBM at X point of the $3C$-GaAs. Yet, surprisingly the floating state appear at the CBM at X point, and shifts downwards under the pressurized condition (See Fig. 4.11), because of the electro-static potential gain at the interstitial sites. Fig. 4.9 shows the result. In particular, it is noteworthy that owing to the competition

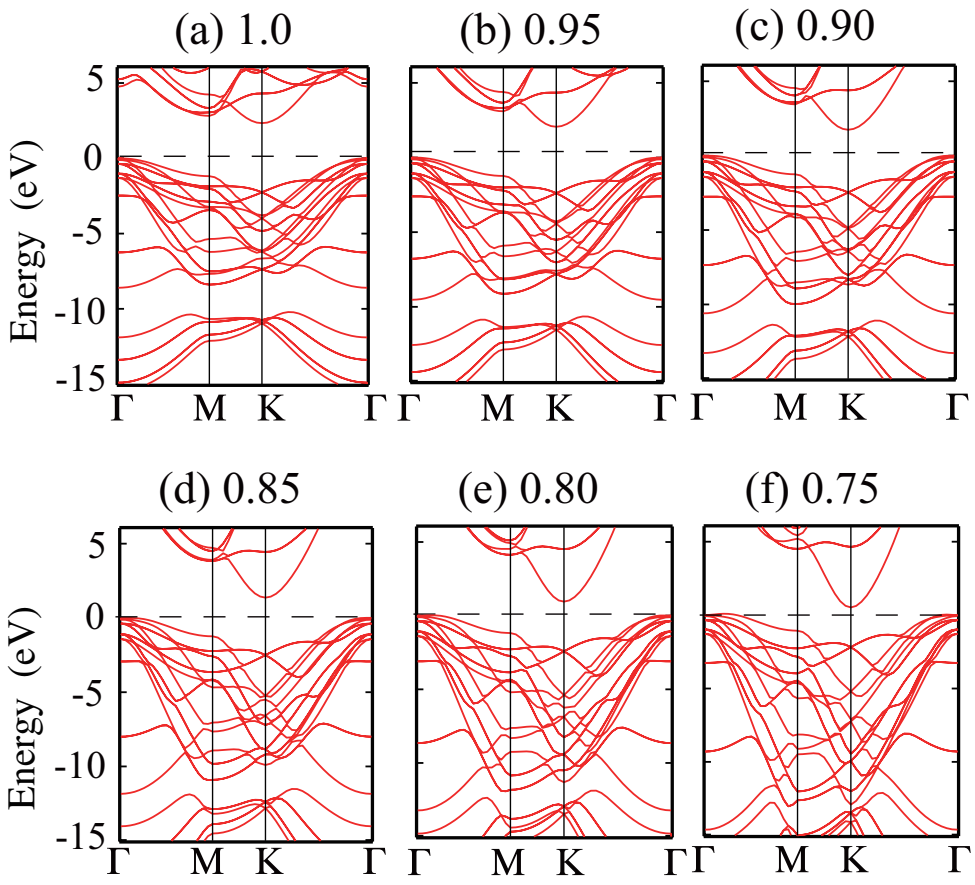

Figure 4.5: Calculated band structure of the 2H-SiC under the pressurized circumstances. Each band structure shows the electron bands with lattice constant scaled from 1.0 to 0.75 with respect to the values in the Table. 3.1. The energy of the valence-band top is set 0. The corresponding pressures are followings: 0 (GPa) for (a), 31.0 (GPa) for (b), 74.2 (GPa) for (c), 129.5 (GPa) for (d), 203.9 (GPa) for (e), and 308.5 (GPa) for (f).

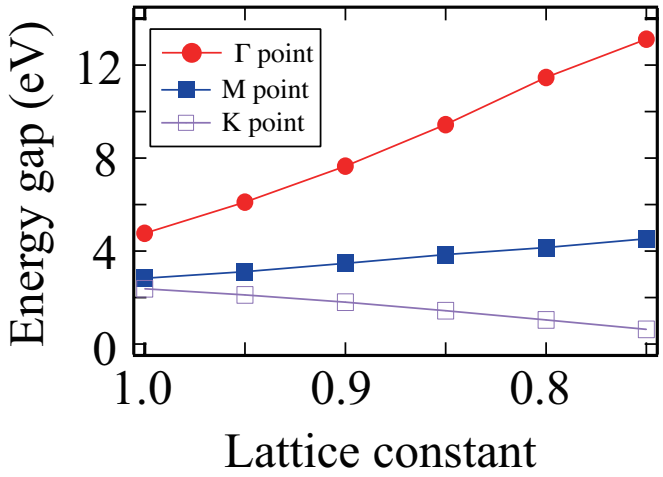

Figure 4.6: Calculated energy levels of the $2H$-SiC at several k points with scaling lattice constants. The corresponding pressures are followings: 0 (GPa) for $a = a_0$, 31.0 (GPa) for $a = 0.95a_0$, 74.2 (GPa) for $a = 0.9a_0$, 129.5 (GPa) for $a = 0.85a_0$, 203.9 (GPa) for $a = 0.80a_0$, and 308.5 (GPa) for $a = 0.75a_0$.

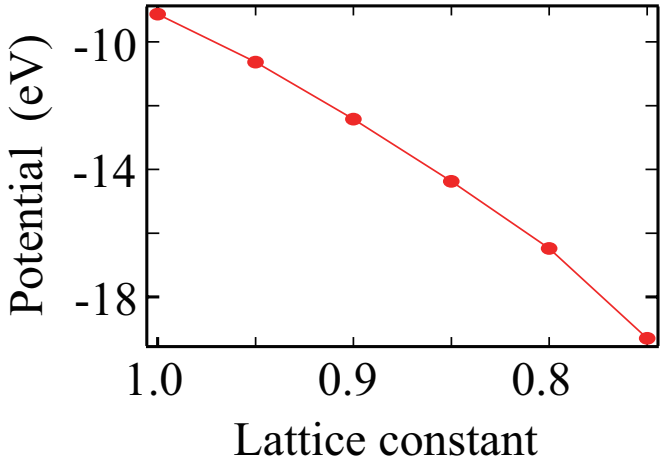

Figure 4.7: Calculated potential energy at the interstitial site of the $2H$-SiC with scaling lattice constants. The corresponding pressures are followings: 0 (GPa) for $a = a_0$, 31.0 (GPa) for $a = 0.95a_0$, 74.2 (GPa) for $a = 0.9a_0$, 129.5 (GPa) for $a = 0.85a_0$, 203.9 (GPa) for $a = 0.80a_0$, and 308.5 (GPa) for $a = 0.75a_0$.

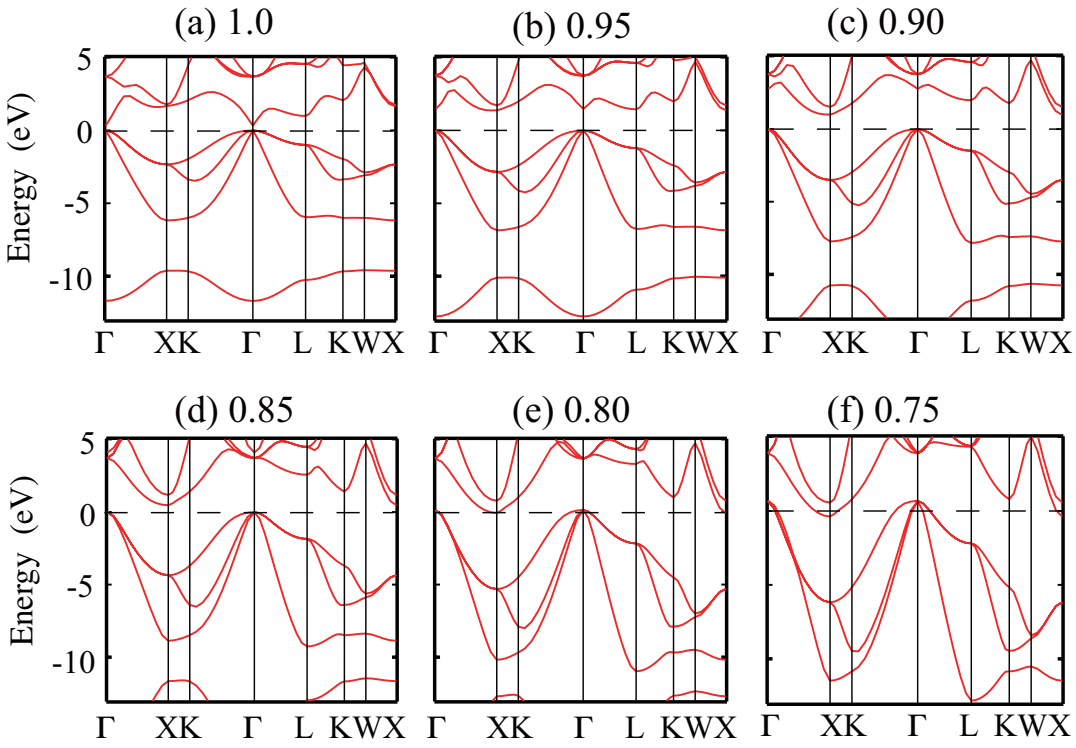

Figure 4.8: Calculated band structures of the 3C-GaAs under the pressurized circumstances. Each band structure shows the electron bands with lattice constant scaled from 1.0 to 0.75 with respect to the optimized values. The energy of the valence-band top is set 0. The X point corresponds to M point in the hexagonal unit cell. The corresponding pressures are followings: 0 (GPa) for (a), 5.9 (GPa) for (b), 12.5 (GPa) for (c), 21.3 (GPa) for (d), 33.6 (GPa) for (e), and 51.5 (GPa) for (f).

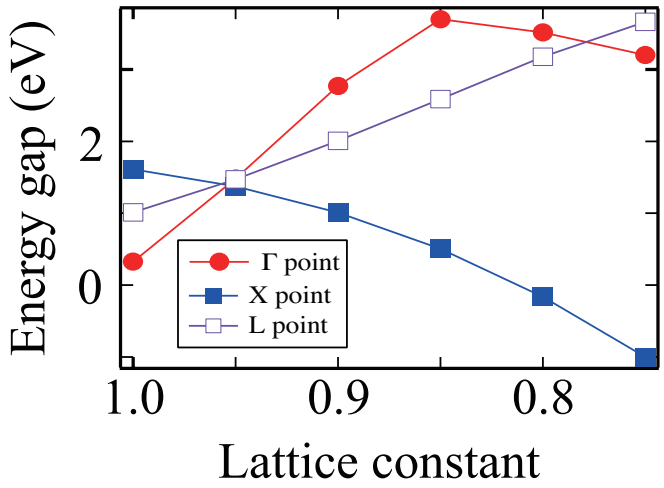

Figure 4.9: Calculated energy levels of the $3C$-GaAs at several k points with scaling lattice constants. The corresponding pressures are followings: 0 (GPa) for $a = a_0$, 5.9 (GPa) for $a = 0.95a_0$, 12.5 (GPa) for $a = 0.9a_0$, 21.3 (GPa) for $a = 0.85a_0$, 33.6 (GPa) for $a = 0.80a_0$, and 51.5 (GPa) for $a = 0.75a_0$.

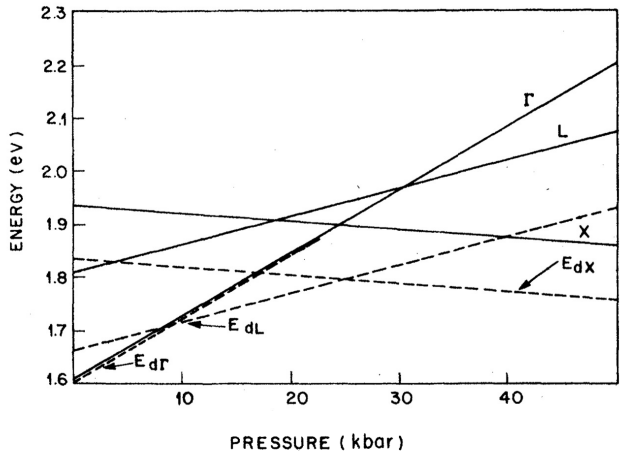

Figure 4.10: The pressure dependence of Γ, L, and X band energies in $Al_{0.15}Ga_{0.85}As$. It is evadent that the direct-indirect crossover occurs near 24.5 bars at this composition. (Ref. (131))

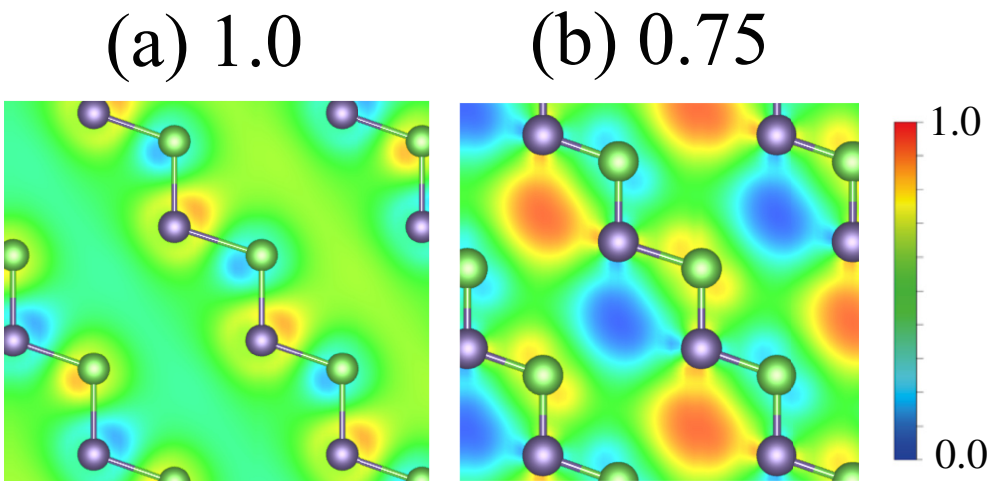

Figure 4.11: (a) Contour plots of the calculated Kohn-Sham (KS) orbital of the conduction band minimum (CBM) at $X = (0, 0, 2\pi/a_0)$ point in the $3C$-GaAs on $(0\bar{1}1)$ plane. (b) Contour plots of the KS orbital of the CBM at X point with the lattice constant being on the scale of 0.75. Floating character is not seen in the figure (a). In the figure (b), floating character is apparent. The gray and green balls depict Ga atoms and As atoms, respectively.

with the electrostatic energy gain from the cation tetrahedron which makes the energy of the floating state at X point low, the transition between the direct gap in the no-pressurized structure and the indirect gap in the pressurized structure takes place. This fact is consistent with experimental facts (131) [Fig. 4.10].

Another interesting system is the pressurized $2H$-diamond. Fig. 4.12 shows the calculated band structures of $2H$-diamond. The floating state at K point shifts downwards substantially and causes a transition from the indirect-gap semiconductor to a semimetal. The Kohn-Sham orbital at the CBM of the $2H$-diamond at the $a = 0.75a_0$ is shown in Fig. 4.13. We have found apparent floating character.

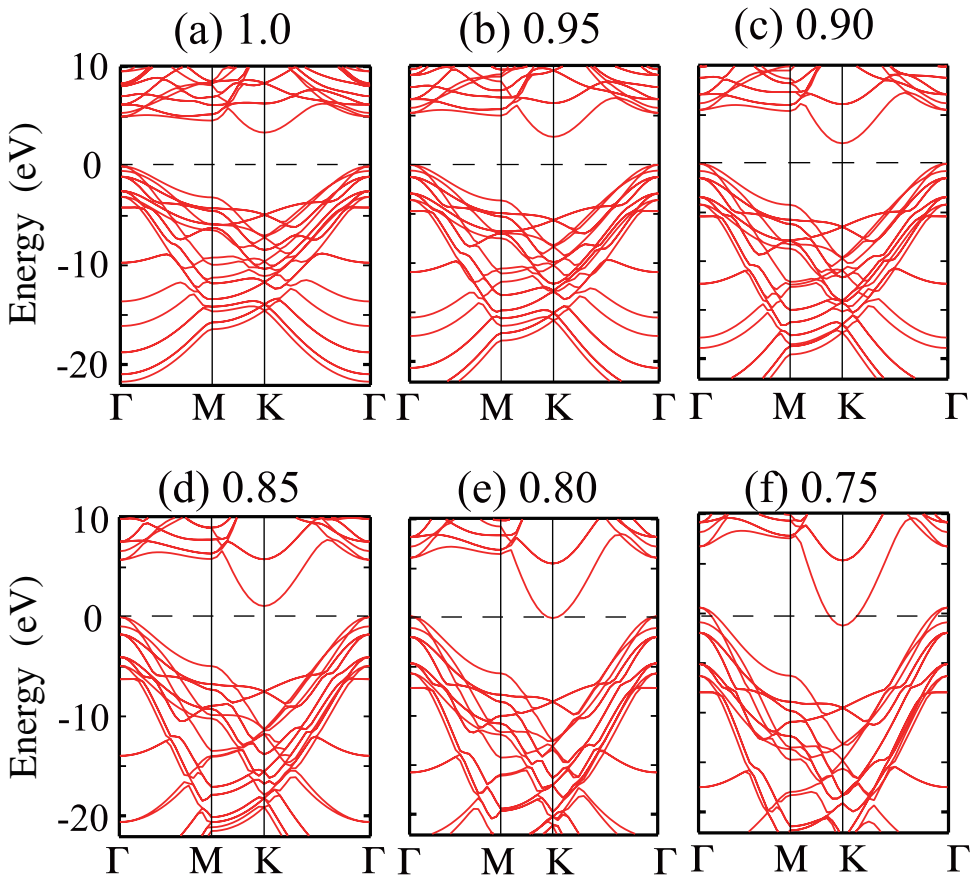

Figure 4.12: Calculated band structure of the $2H$-diamond under the pressurized circumstances. Each band structure shows the electron bands with lattice constant scaled from 1.0 to 0.75 with respect to the values in the Table. 3.1. The energy of the valence-band top is set 0. The corresponding pressures are followings: 0 (GPa) for (a), 34.6 (GPa) for (b), 80.0 (GPa) for (c), 138.2 (GPa) for (d), 214.4 (GPa) for (e), and 319.3 (GPa) for (f).

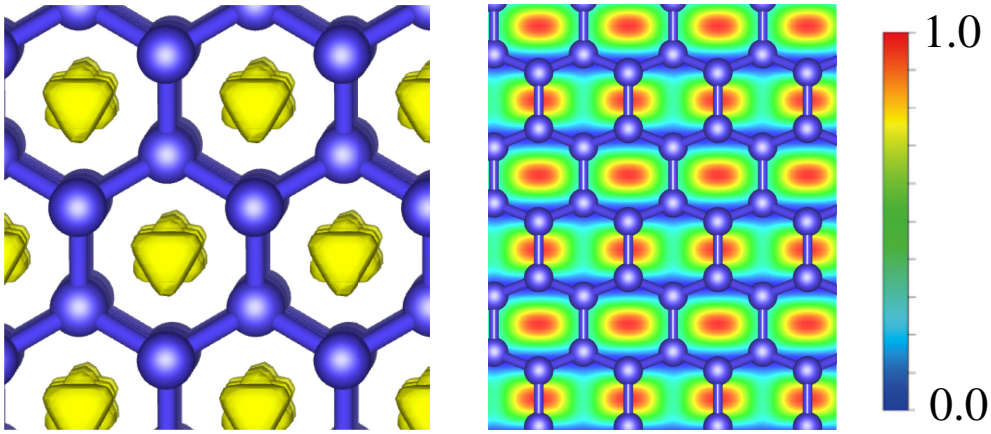

Figure 4.13: Isosurface (a) at its value of 90% of maximum value and contour plots (b) of the calculated Kohn-Sham (KS) orbital at the conduction band minimum (CBM) at K point in the $2H$-diamond on $(1\bar{1}00)$ plane, respectively. The blue balls depict C atoms.

5

Channel length and floating state

5.1 Relations between channel lengths and floating states

As mentioned in the introduction, the band-gap variation in SiC is understood by the analyses using an empirical parameter "hexagonality" for a half century. The band-gap variation has been said to have linear relations with the hexagonality. Yet, the relations between band-gap variation and the hexagonality have not been verified yet. Our purpose in this section is to manifest that the hexagonality is a misleading parameter and that the parameter misses an important point of floating nature in the conduction-electron state for SiC. In addition, we propose an essential parameter in describing the band-gap variation, and show that the analyses using the parameter make it possible to reproduce the band-gap variation even quantitatively.

Above, we have clarified the mechanism of the band-gap variation in SiC polytypes based on the DFT. The key is the appearance of the *floating* states at the conduction-band minima in most sp^3-bonded materials. The floating state has a nearly-free-electron (NFE) like character, extending in channels without atomic-orbital characters. In addition, the difference in the electronegativity between the constituent atoms in the system causes particular T_d interstitial sites to be energetically favorable. In fact, the difference in the electro-negativity makes the energy level of the floating state, extending in the [110] channels, shift downwards, thus causing substantial band-gap decrease in the $3C$-SiC (See Fig. 5.1 (a)). A similar structural feature is observed in the $6H$-SiC. Yet, the hexagonal layers block the channel, and the channel length becomes finite. There is the channels with the length of about $7a_0/2\sqrt{2}$ along the $[2\bar{2}01]$, which

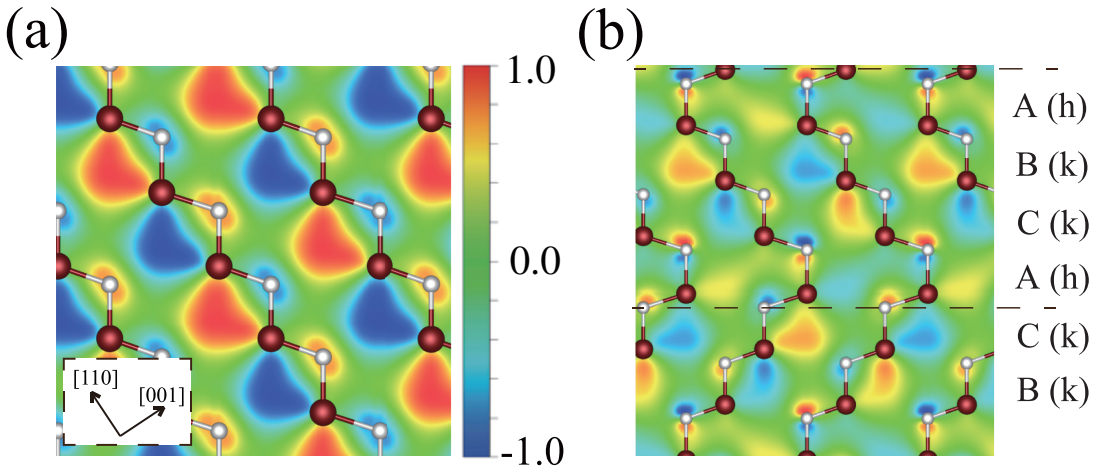

Figure 5.1: Contour plots of the Kohn-Sham (KS) orbitals at the conduction-band minimum for the $3C$-SiC (a), and for the $6H$-SiC (b) on $(1\bar{1}0)$, and $(11\bar{2}0)$ plane, respectively. The value for each contour color is relative to the corresponding maximum absolute value. White and burgundy balls depict C and Si atoms, respectively. In (b), the channel length of the $6H$-SiC is finite, and the broken lines represent the longest channel length. At the broken lines, the hexagonal layers block the channel.

is slanted relative to [0001] direction. We have indeed found that the Kohn-Sham (KS) orbital at the conduction-band minimum (CBM) in $6H$-SiC distributes in this channel (Fig. 5.1 (b)). Due to the limited length in the channel, the kinetic energy gain is smaller than in the $3C$ structure, and the energy gap in the $6H$ structure becomes wider by 0.9 eV. Therefore, one expectation arises that the energy gap is larger with the [110]-channel length decreasing. This means that "*channel length*" is a more essential parameter than the "hexagonality".

Here we have performed the calculations for the SiC polytypes whose periodicity of the stacking sequence is lower than 12-bilayers. Each of the nH polytypes with $2 \leq n \leq 5$ have a unique structure. The $6H$, $8H$, $10H$, and $12H$ polytypes have 2, 6, 18, and 58 structures, respectively (127). The possible hexagonalities in the $10H$ polytype are 20, 40, 60, and 80%. Those in the $12H$ polytype are 16.7, 33.3, 50, 66.7, and 83.3%. We have treated all possible hexagonalities in the $8H$, $10H$, and $12H$ (128). The stacking sequences, which we have treated in this study, are 24 different stacking sequences, listed in the Table 5.1.

Fig. 5.2, and Table 5.1 show the calculated band gaps for the 24 different polytypes.

Table 5.1: Calculated band gaps for 24 different SiC polytypes. The definitions of the "hexagonality" and "channel length" are in the text.

polytypes	band gap (eV)	hexagonality (%)	channel length
	$3C$ structure		
ABC	1.419	0	∞
	$4H$ structure		
ABCB	2.315	50	3
	$5H$ structure		
ABCBC	1.822	40	5
	$6H$ structures		
ABCBCB	2.452	66.7	3
ABCACB	2.077	33.3	4
	$8H$ structures		
ABCABACB	1.853	25	5
ABCABCAB	1.679	25	8
ABCACBAB	2.087	50	4
ABCACBCB	2.104	50	4
ABCBABAB	2.408	75	3
ABCBCBAB	2.324	75	3
	$10H$ structures		
ABCABCABAB	1.593	40	8
ABCABCABCB	1.585	20	9
ABCABCBACB	1.754	20	6
ABCACBCACB	2.071	40	4
ABCBCACBCB	2.436	60	3
ABCBCBCBCB	2.399	80	3
	$12H$ structures		
ABACABCBCACB	2.094	50	4
ABCABACABACB	1.864	33.3	5
ABCABACBCACB	1.911	33.3	5
ABCABCABCACB	1.574	16.7	10
ABCABCACBACB	1.679	16.7	7
ABCACACACACB	1.975	66.7	4
ABCBCBCBABAB	2.402	83.3	3

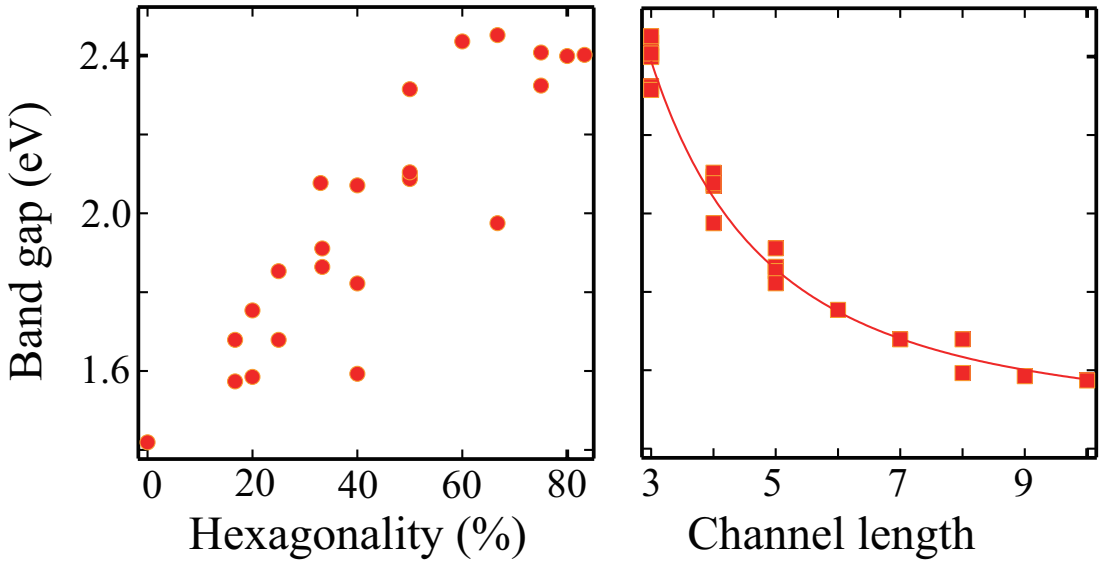

Figure 5.2: Calculated band gaps for SiC polytypes are plotted. (Left panel) The abscissa depicts the hexagonalities and the ordinate depicts the calculated band gaps for SiC polytypes. (Right panel) The abscissa depicts the channel lengths. We draw a fitting function, expressed by the Eq. (5.1) in the text.

Most conduction-band minima are located at M point, except for the $5H$-SiC at L point. This is because of the odd number of the periodicity of the stacking sequences in the $5H$ structure. Floating state at the CBM changes its sign along the [110] direction. By examining the irreducible representation, such phase shift is allowed not at M point, but at L point. Fig. 5.2 shows the relations between the calculated band gaps and the hexagonalities. As a whole, the results seem to reveal some correlation between them. Yet, the dispersion is very large. It is clear that the relation can not be expressed by a simple mathematical function. Next we plots the calculated band gaps as a function of the channel lengths. In the figure and the table, we plot the channel length as the number of the stacking sequence of the longest [110] channels in the unit cell. We have found the clear relations between the channel length and the band gap. The relation is expressed by a following function with beautiful fitting:

$$y = 1.4248 + \frac{17.626}{(x + 1.2678)^2}. \tag{5.1}$$

Next we discuss the verification of the fitting function. Consider an electron, confined in a 1-dimensional quantum well with infinite depth. The energy level of the ground

state, ϵ is

$$\epsilon = \epsilon_0 + \frac{\hbar^2 \pi^2}{2m^* L^2}, \tag{5.2}$$

where ϵ_0, m^*, and L are constant, effective mass, and the width of the well, respectively. Comparing the Eq. 5.1 with the Eq. 5.2, the ϵ_0 represents the band gap in the $3C$, or corresponds to the case of the infinite channel length. It shows good agreement with the calculated band gap of the $3C$, 1.419 (eV). In addition, we have derived an important factor, effective mass, from the comparison with the two equations. The effective mass is $0.326m_0$ with m_0 being an electron mass in vacuum. The effective mass gives the great agreement with the experimental value, $0.363m_0$. The $x + 1.2678$ in the Eq. 5.1 depicts the effective width of the quantum well, because the depth of the well is not infinite in the real system. The figure, 1.2678, shows that the floating state penetrates outside the channel by one-bilayer thickness.

Here we show a prominent result, where two polytypes should have the same band gap from the viewpoint of the hexagonality. The two are ABCABCABAB and ABCACBCACB. Their hexagonalities are the same, 40%, while their channel lengths are different, being 8, and 4, respectively. Their band gaps are 1.593 eV, and 2.071 eV, respectively. It has been apparent that the hexagonality fails to reproduce the band-gap variation. In contrast, the new parameter "channel length" works well also in this case. We easily imagine the distribution of KS orbital at the CBM. The Fig. 5.3 shows the results. The distribution of the orbitals extends in the longest [110] channels in each polytype as is expected.

Here we discuss an interesting system. Consider the system that we cut a bundle of channels with a cutting plane inclined from the channel axis. When the channel has the infinite length, each channel has the same length, and any interesting phenomenon does not occur. When the channels with finite length are cut by the inclined plane, each channel has different length like a xylophone. Then the distribution of the KS orbital at the CBM is spatially gradient: the floating state distributes in longer channels, not in the shorter channels. When we prepare such a surface, an interesting non-uninform distribution of the floating state at the CBM will appear on the surface.

In addition, we refer to another possible model for the situation where electrons extending in channels. Above, we have adopted a 1-dimensional quantum-well model as a fitting function for the relations between channel length and band gap. Yet, the

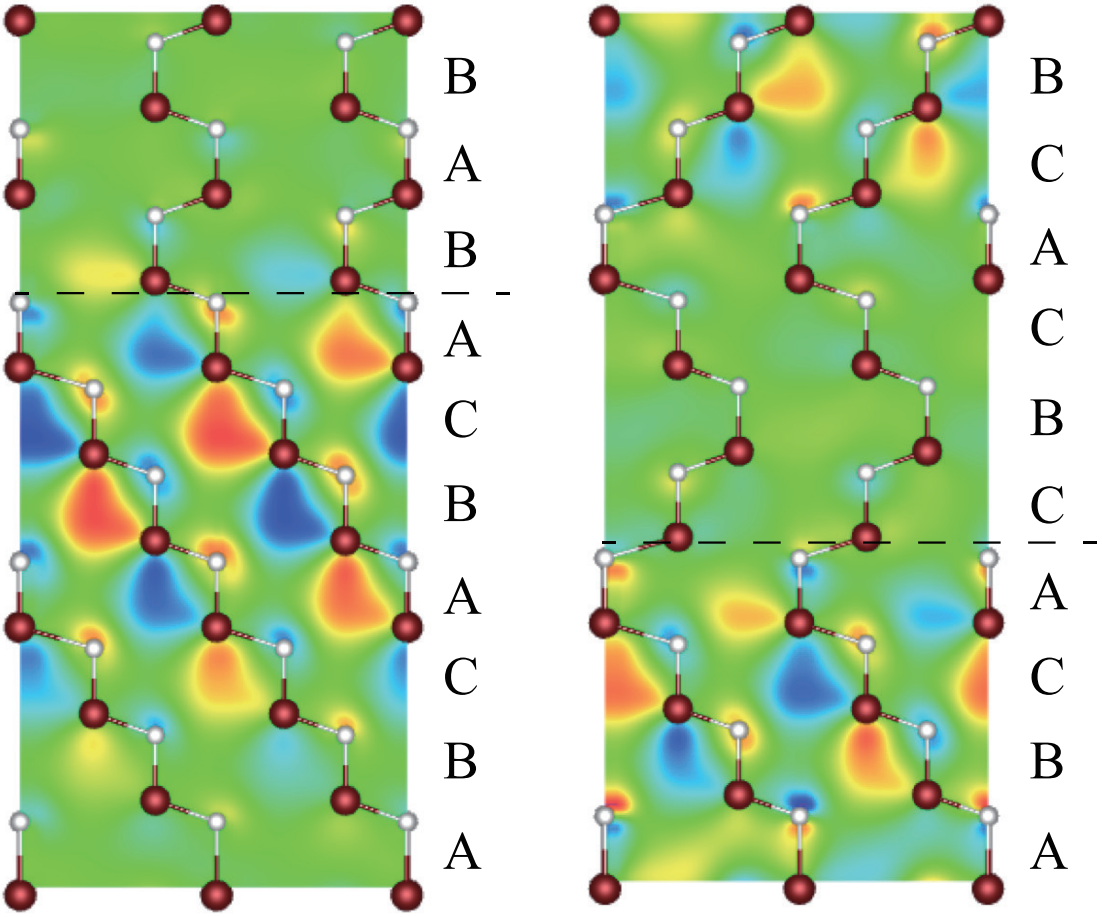

Figure 5.3: Contour plots of the Kohn-Sham (KS) orbitals of the conduction-band minimum at M for the ABCABCABAB stacking (left panel), and for the ABCACBCACB stacking (right panel) on $(11\bar{2}0)$ plane for the $10H$-SiC. The value for each contour color is relative to the corresponding maximum absolute value. White and burgundy balls depict C and Si atoms, respectively. The broken lines represent the interface between the longest channel region and hexagonal region.

situation where electrons extending in tube-like nano space shows that another model, quantum confinement model in a finite-length tube, may be more realistic. The model hamiltonian is,

$$-\frac{1}{2m^*}\nabla^2\phi = \epsilon\phi, \tag{5.3}$$

in the atomic units, with a boundary condition, $\phi(r = a) = 0$, where a represents the radius of the tube. Here, we rewrite the equation on the cylindrical coordinates:

$$-\frac{1}{2m^*}\{\frac{d^2}{dr^2} + \frac{1}{r}\frac{d}{dr} + \frac{1}{r^2}\frac{d^2}{d\theta^2} + \frac{d^2}{dz^2}\}\phi = \epsilon\phi. \tag{5.4}$$

By the separation of variables, we then separate the Eq. (5.4) into two parts, the radial component and the axial component:

$$-\frac{1}{2m^*}\{\frac{d^2}{dr^2} + \frac{1}{r}\frac{d}{dr}\}\phi_r = \epsilon_r\phi_r, \tag{5.5}$$

and

$$-\frac{1}{2m^*}\ \frac{d^2}{dz^2}\phi_z = \epsilon_z\phi_z. \tag{5.6}$$

The eigen function for the ground state of the radial component, Eq. (5.5), is a Bessel function, and the eigenvalue is

$$\epsilon_r = \frac{Z_0^2}{2m^*a^2}, \tag{5.7}$$

where Z_0 represents a zero of the Bessel function, 2.40483. In contrast, as for the axial component, Eq. (5.6), this is the same problem as the 1-dimensional quantum well, and we know the answer

$$\epsilon_z = \frac{\pi^2}{2m^*L^2}. \tag{5.8}$$

Therefore, the eigen value ϵ of the Eq. (5.3) is given as $\epsilon = \epsilon_r + \epsilon_z$, as follow:

$$\epsilon = \frac{Z_0^2}{2m^*a^2} + \frac{\pi^2}{2m^*L^2}. \tag{5.9}$$

Compared with Eq. (5.2), the effect of the tube-like boundary is included in the ϵ_0 in the Eq. 5.2. Suppose that the effective mass in the radial equation m^* is the same as that in the axial equation, the derived confined radius a is estimated to be 6.527 Å. The radius of the [110] channel in the $3C$-SiC is about 1.171 Å. The estimated confined radius is 3.8 times of the [110] channel. We have found that the above two models gives the same solution.

Table 5.2: Comparison of effective masses in SiC polytypes.

Properties	3C-SiC	4H-SiC	6H-SiC
Stacking sequence	ABC	ABCB	ABCACB
Experimental effective mass (Ref. (16))	$m_{\|\|X-\Gamma}$: 0.67 $m_{\perp X-\Gamma}$: 0.22 − 0.25	$m_{M-\Gamma}$: 0.30 − 0.58 m_{M-L} : 0.33 − 0.48	$m_{M-\Gamma}$: 0.24 − 0.42 m_{M-L} : .1.7 − 2.0
Calculated effective mass (present work)	$m_{M-\Gamma}$: 0.41 m_{M-L} : 0.29	$m_{M-\Gamma}$: 0.53 m_{M-L} : 0.3	$m_{M-\Gamma}$: 0.26 m_{M-L} : .1.6

In conclusion, our GGA calculations have clarified that the parameter "hexagonality" is a misleading parameter in describing the substantial band-gap variations in SiC. In contrast, we have found that a new parameter "channel length" is an essential parameter. We have found that the energy level of the floating state, confined in a channel with finite length, shifts upwards due to the electron confinement. Therefore, the parameter "channel length" represents the spatial extension of the floating state, and has clear physical validity. We have also found that the analysis by using the parameter "channel length" makes it possible to reproduce the band-gap variation quantitatively. The results not only clarify the mechanism of the band-gap variation, but also provide a guideline for designing electronic properties by controlling the shapes of internal nanospace in matter.

5.2 Anisotropy of effective mass

In this section, we consider the anisotropy in effective masses of electrons. As we mentioned in the Sec. 1.2, an anisotropy in effective mass in the 6H structure along the c-direction is reported in experiments (Table 5.2). We have also calculated the effective masses in the 6H-SiC. Our calculations have given a good agreement with the experimental values in the 6H-SiC: The effective mass perpendicular to the c-axis, $M-\Gamma$ direction, is estimated to be $0.264m_0$, while that along the c-axis to be $1.605m_0$, where m_0 represents electron mass in vacuum. Furthermore, it is known that the anisotropy in effective masses depends on the structural polytypes substantially in experiments. There are no such peculiar anisotropy in the 4H, and 3C structures.

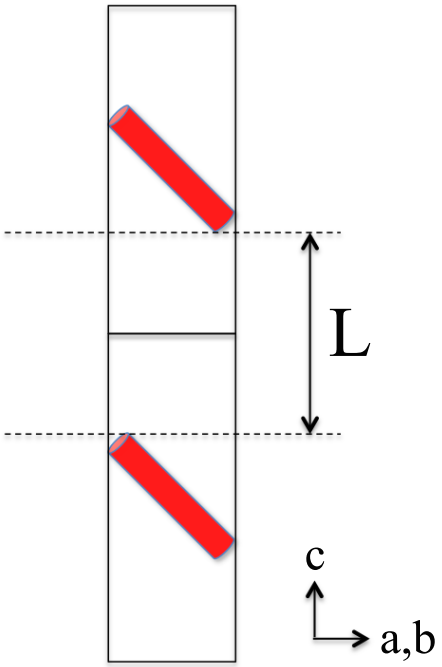

Figure 5.4: Square boxes represent the unit cells. The red tubes represent the finite-length [110] channels along the c-direction. Remark that the wave function of the conduction-band-minimum distributes only in the channels, which are colored region by the red. The region without any color in the unit cell represent the hexagonal stacking region. The barrier width between the two channel regions, or in other words channel distance, along the c-axis is L.

In fact, our calculations for the effective masses in the $3C$-SiC along the c-axis and the perpendicular to the c-axis shows no peculiar anisotropy: $0.41059m_0$ along the M-Γ direction, and $0.2934m_0$ along c-axis. As we have mentioned in this thesis, we have clarified that the wave function at the CBM in SiC polytype has a *floating* character, extending in interstitial channels. Furthermore, we have found that when channel lengths are finite, floating states distribute or are localized in the finite region of the channels. In particular, the $6H$ structure has finite length channels along the c-direction, which suggests a possibility of the deep relations among the floating states, channel length, and the anisotropy in effective masses. We have investigated the relation in this section.

Let me consider a simple model of finite-length channel along the c-direction (Fig. 5.4), where each channel is separated one another by distance, L. Remark that the KS orbital

Table 5.3: Calculated effective mass for the 7 different SiC polytypes. The $3C$-SiC is also listed for reference. The corresponding channel distances, channel length, and band gap are also listed.

polytypes	channel length	Barrier width L	effective mass (ab-plane)	effective mass (c-axis)	band gap (eV)
$3C$ (ABC)	∞	–	0.41059	0.2934	1.419
$5H$ (ABCAB)	5	0	0.519	0.497	1.888
$7H$ (ABCABAB)	5	2	0.739	6.264	1.852
$9H$ (ABCABABAB)	5	4	0.677	1.511	1.815
$11H$ (ABCABABABAB)	5	6	0.665	2.655	1.802
$13H$ (ABCABABABABAB)	5	8	0.665	9.011	1.780
$15H$ (ABCABABABABABAB)	5	10	0.669	40.081	1.764
$17H$ (ABCABABABABABABAB)	5	12	0.668	159.86	1.747

at the CBM distributes solely in the finite-length interstitial channels. If the distance L is very large, the electron transport probability along the c-axis is expected to be very small, because the hopping from one channel to another is quite small. Remark that there are infinite-length channels perpendicular to the c-axis. (In the cubic structure, the [110] channel has equivalent six channels: [110], [101], [011], [$\bar{1}$10], [10$\bar{1}$], and [0$\bar{1}$1] channels. Even if the [110]-channel length, which is "slanted" to the a, b-plane, is finite, other equivalent channels, [1$\bar{1}$0], [0$\bar{1}$1], and [10$\bar{1}$] channels exist, which are "parallel" to the a, b-plane.) Therefore, the electron transport in the ab-plane is expected not to show such peculiar behaviors.

At first, we have investigated the relations between the channel distance and the effective mass with channel length fixed. We have examined the following polytypes:

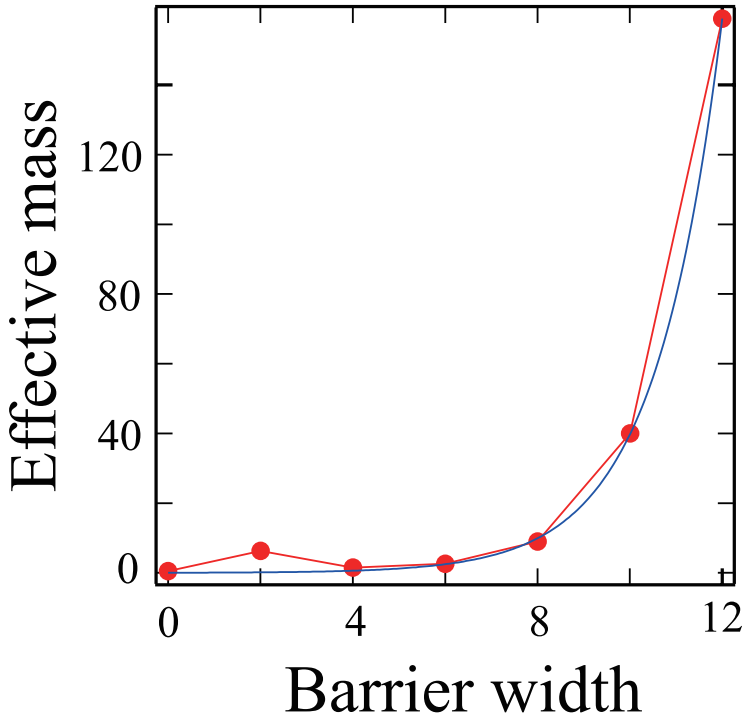

Figure 5.5: Calculated effective masses of the conduction-band minimum (CBM) along the c-axis as a function of barrier widths. Blue curve represents the fitting function (See text). The plotted points represent $5H$, $7H$, $9H$, $11H$, $13H$, $15H$, and $17H$ polytypes listed in Table 5.3.

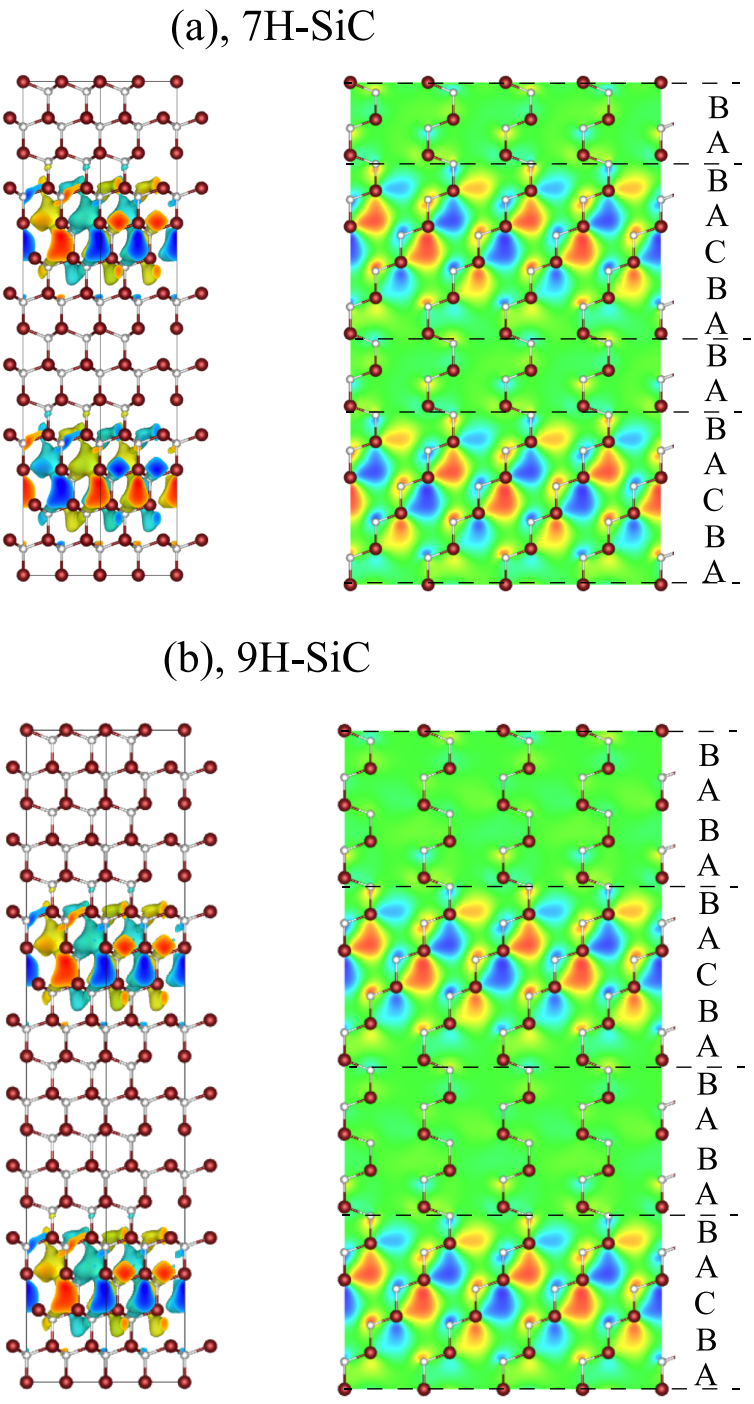

Figure 5.6: Isosurface of 60 % of maximum amplitude and contour plot on $(11\bar{2}0)$ plane of the Kohn-Sham (KS) orbital at the conduction-band minimum (CBM) for the $7H$ polytype (a) and $9H$ polytype (b). The $7H$ ($9H$) polytype has 5-bilayer channel length and 2-bilayer (4-bilayer) barrier width. In each polytype, the KS orbital is localized at the channel regions. Yellow and blue surfaces depict the positive and negative sign of the KS orbital at the CBM, respectively.

$5H$ (ABCAB), $7H$(ABCABAB), $9H$(ABCABABAB), $11H$(ABCABABABAB), $13H$(ABCABABABABAB), $15H$(ABCABABABABABAB), and $17H$(ABCABABABABABABAB). Each polytype has 5-bilayer-length [110] channels, slanted to the a, b-plane, and we have separated the channels away by adding hexagonal layers, AB-stacking layers, between the channels up to 12 bilayers. The filling hexagonal layers work as a Barrier for the electron at the CBM. Table. 5.3 shows the effective masses in the ab-plane, and along the c-axis. From the table, it has been found that the effective mass in the ab-plane shows no anisotropy, and almost no changes with increasing the barrier width, L. On the other hand, the effective mass along the c-direction shows surprising dependence on the channel distance, or barrier width. In particular, as for the $17H$ polytype, the effective mass along the c-axis is 240 times larger than that in the $a, b-$plane. Fig. 5.5 shows the effective mass along the c-axis as a function of the barrier width. From the figure, the enhancement of the effective mass is increasing exponentially with increasing the barrier width. The fitting function is $y = 0.040 \times \exp(0.693 \times x)$. The reason of the exponential enhancement is followings: the wave function of the CBM is confined in the finite-length-channel region, and penetrates outside the channel region with exponential decay. In the barrier region, or hexagonal region, two localized wave functions have overlap with each other at the tail of the exponential decay. Therefore, the hopping from one channel region to another is thought to be exponential decay as a function of the barrier width. We have found the shapes of channels are decisive in determining the anisotropy in the effective mass of electrons substantially. Fig. 5.6 shows the KS orbitals at the CBM with the 2-bilayer barrier width (a), and 4-bilayer barrier width (b). It is clearly seen that each orbital is localized in the channel regions.

The calculated band gaps are also listed in the Table. 5.3, showing almost the same values within the range of 0.15 eV, as is expected, because their channel length is fixed at 5 bilayers.

We also have calculated another case where the channel length is fixed at 8 bilayers. The Table. 5.4 and Fig. 5.7 shows the results. A similar anisotropy in effective masses is seen as those with channel length fixed at 5. The anisotropy with the channel length fixed at 8, however, appears more significantly. This difference comes from that increasing channel length leads to electrons being confined strongly in channel, because

Table 5.4: Calculated effective mass for the 7 different SiC polytypes. The $3C$-SiC is also listed for reference. The corresponding channel distances, channel length, and band gap are also listed.

polytypes	channel length	Barrier width L	effective mass (ab-plane)	effective mass (c-axis)	band gap (eV)
$3C$ (ABC)	∞	–	0.41059	0.2934	1.419
$8H$ (ABCABCAB)	8	0	0.487	0.566	1.597
$10H$ (ABCABCABAB)	8	2	0.618	14.443	1.560
$12H$ (ABCABCABABAB)	8	4	0.589	2.667	1.495
$14H$ (ABCABCABABABAB)	8	6	0.587	4.593	1.451
$16H$ (ABCABCABABABABAB)	8	8	0.589	19.251	1.415
$18H$ (ABCABCABABABABABAB)	8	10	0.585	30.782	1.385
$20H$ (ABCABCABABABABABABAB)	8	12	0.591	305.236	1.359

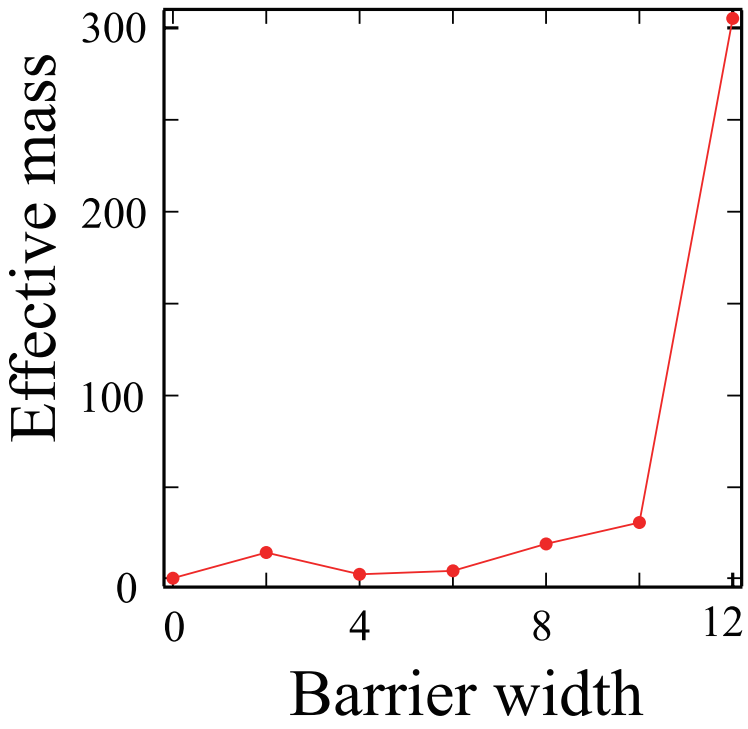

Figure 5.7: Calculated effective masses of the conduction-band minimum (CBM) along the *c*-axis as a function of barrier width.

the energy level of the floating state is lower. As for the $20H$ polytype, the effective mass in the a, b-plane is 516 times larger than that along the c-axis.

6

Spontaneous polarization

6.1 Spontaneous polarization effects on band gap

As we have shown in Table 5.3, and Table 5.4 in Sec. 5.2, the band gaps are decreasing monotonically with increasing the barrier width. Fig. 6.1 and Fig. 6.2 show the results. In particular, the $20H$-SiC with 12-bilayer-barrier width gives band gap, 1.359 eV, which is narrower than in the bulk $3C$ polytype, 1.419 eV. It shows clearly that another factor should be taken into account.

The symmetry of the $3C$ structure is T_d including six mirror symmetries. On the other hand, the symmetry of the $2H$ structure is C_{6v}, which does not include the mirror symmetries perpendicular to the c-axis (horizontal mirror symmetry, σ_h). Whether each structure has the horizontal mirror symmetries or not has great effects on the occurrence of the spontaneous polarization along the c-axis. The $2H$ has spontaneous polarization along the c-axis, while the $3C$ structure does not. We have found the band-gap narrower is related to the spontaneous polarization. In this section, we clarify the influence of the spontaneous polarization on the energy bands.

Local density of states (LDOS), $D(\varepsilon, z)$, is useful to identify the region where carriers are confined and clarify effects of the spontaneous polarization. Using the obtained Kohn-Sham (KS) eigenvalue $\epsilon_{n\mathbf{k}}$ and the orbital $\varphi_{n\mathbf{k}}$, it is defined by

$$D(\epsilon, z) = \int d\mathbf{r}_\perp \sum_{n\mathbf{k}} \delta(\epsilon - \epsilon_{n\mathbf{k}}) |\varphi_{n\mathbf{k}}(\mathbf{r})|^2 \tag{6.1}$$

where z is the coordinate along the stacking direction of polytypes and $\mathbf{r}_\perp$ is a two dimensional vector on the perpendicular plane in a unit cell. Figure 6.3 shows calculated

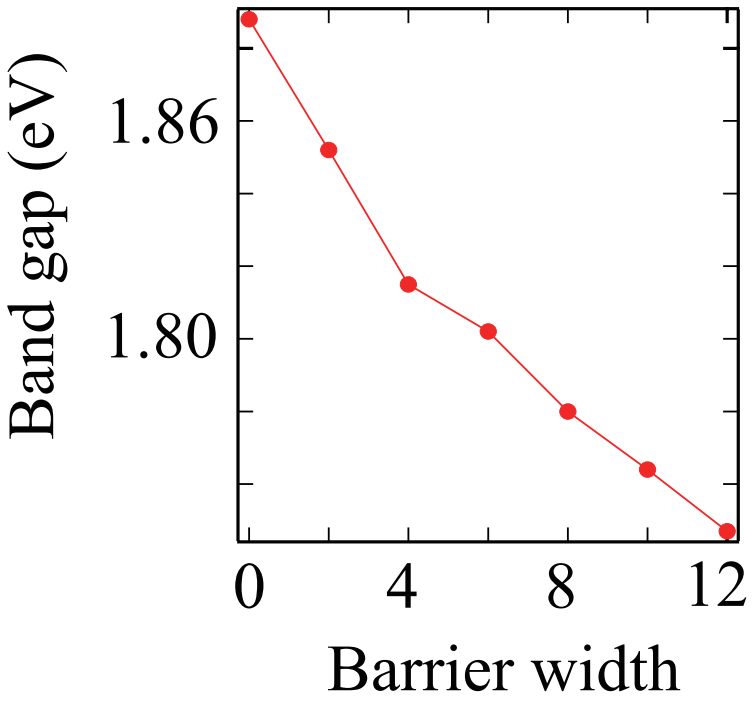

Figure 6.1: Calculated band gaps with respect to the barrier width with channel length being fixed at 5-bilayer. These values are listed in Table 5.3.

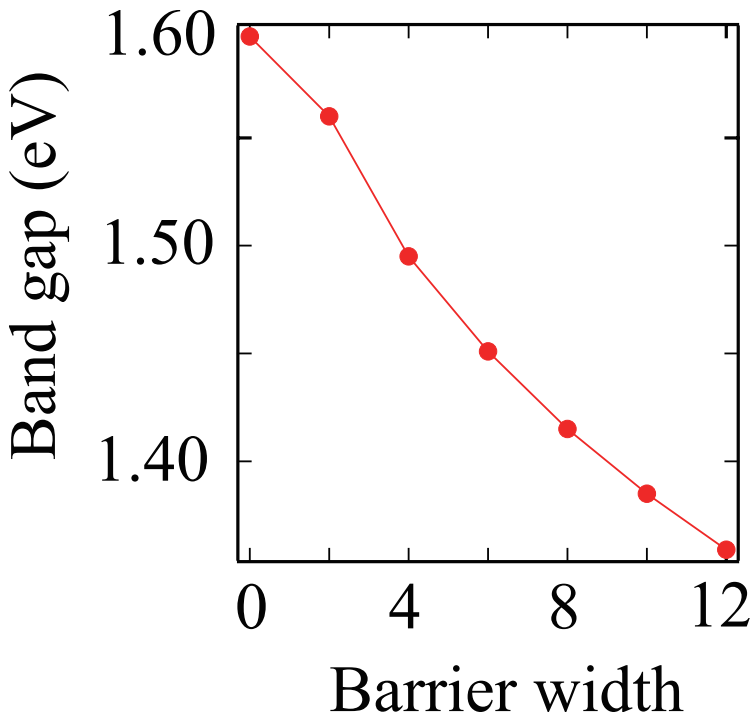

Figure 6.2: Calculated band gaps with respect to the barrier width with channel length being fixed at 8-bilayer. These values are listed in Table 5.4.

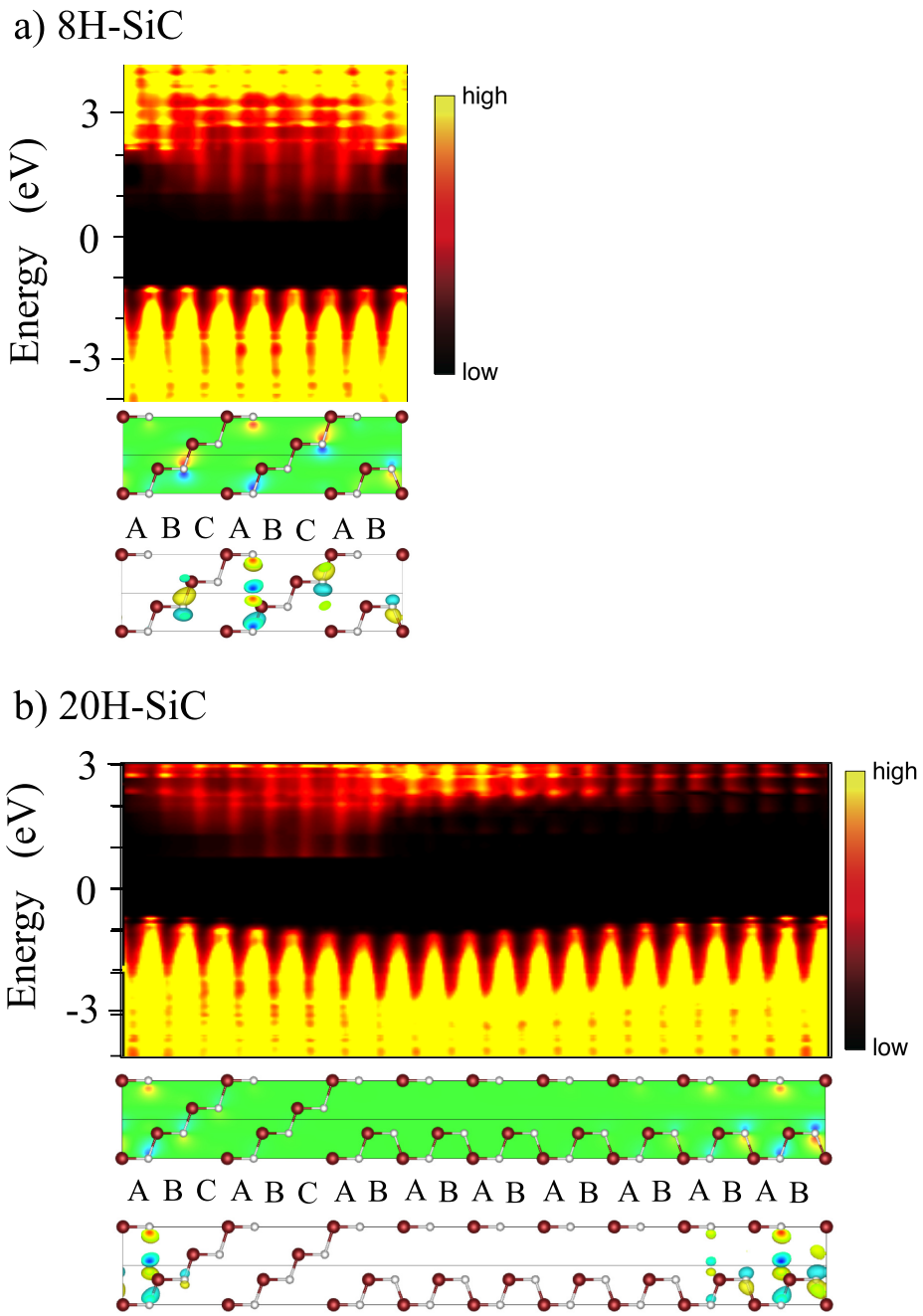

Figure 6.3: Contour plots of the calculated local density of states (LDOS) $D(\varepsilon, z)$ for the 8H (ABCABCAB) polytype (a) and the 20H (ABCABCABABABABABABAB) polytype (b) listed in Table 5.4. Horizontal direction is the stacking direction (c-axis) and corresponds to z coordinate. Contour plot and isosurface of the 30 % of the maximum values of the Kohn-Sham (KS) orbital at the valence-band top (VBT).

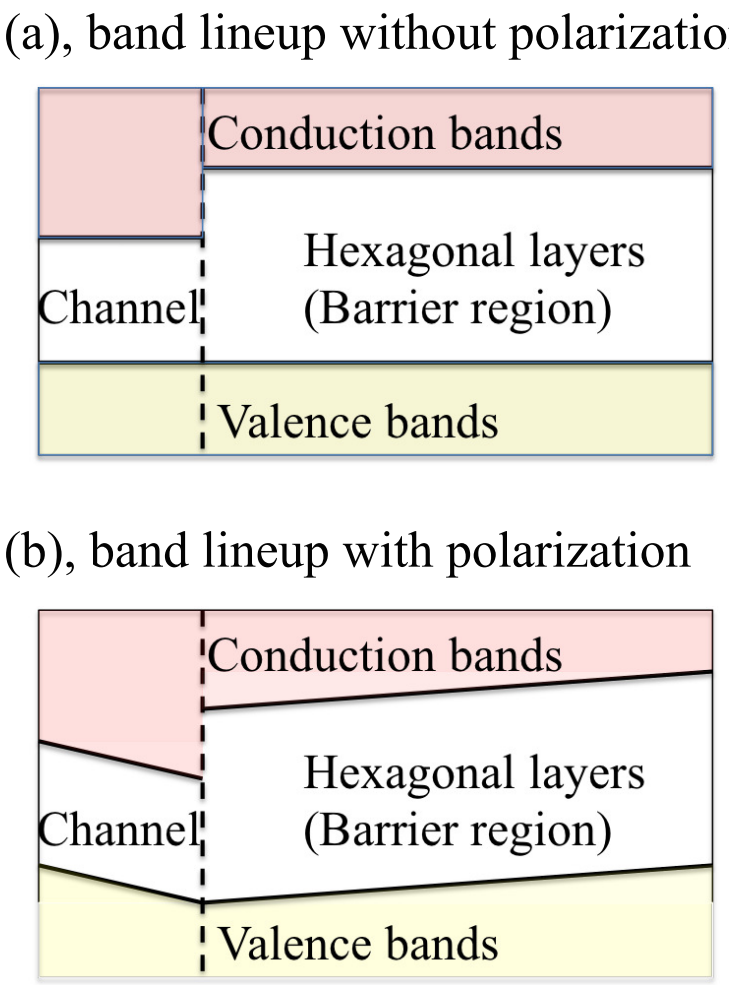

Figure 6.4: Sketches of band lineup of the 20H-SiC in Fig. 6.3. (a): Sketches of band lineup of an imaginary 20H-SiC polytype without spontaneous polarization. In reality, however, the spontaneous polarization in the barrier region renders the band lineup slanted in real space along the stacking direction, and further the counter polarization in the channel region (b).

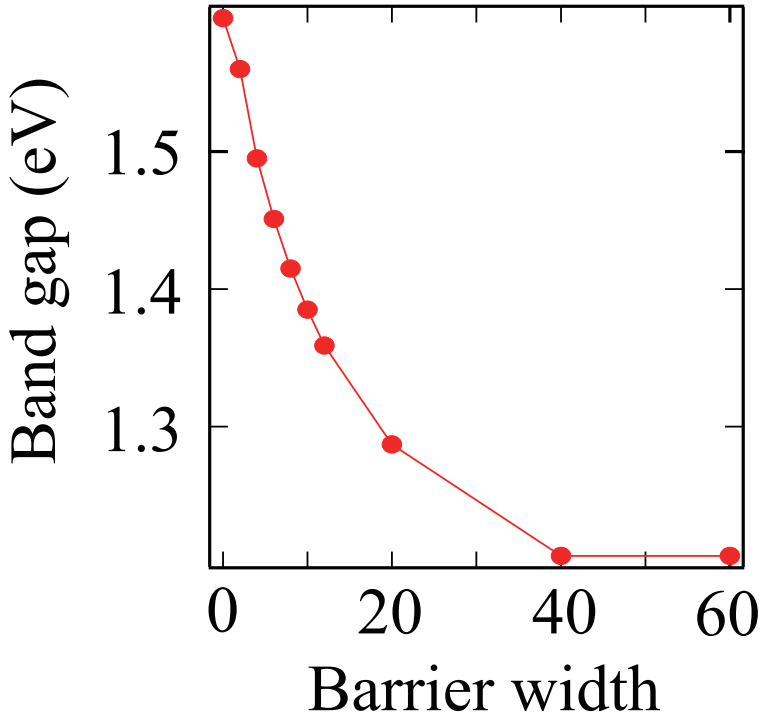

Figure 6.5: Calculated band gaps as a function of barrier width with the channel length being fixed at 8 bilayers.

LDOS for the SiC-polytypes giving the largest and smallest band gap in the Table 5.4. Spiky contrasts represent atomic positions along the z axis. It is clearly shown that the conduction bands in channel region is located at lower positions in energy than in the barrier region: i.e., electrons are confined in channel region. The valence-band offset is unclear in these polytypes than the conduction bands. Fig. 6.4 shows the sketches of the band lineup. The spontaneous polarization in the barrier region renders the band lineup slanted in real space along the stacking direction, and further the counter polarization in the channel region makes it slanted in reverse direction. We have found that the slanted band lineup causes downward (upward) shift of the conduction (valence) band edge and the band gap becomes narrower.

Then, we have investigated the band gaps with increasing the barrier width with the channel length being fixed at 8 bilayers. Fig. 6.5 shows the calculated band gaps as a function of barrier width. The calculated band gaps are decreasing monotonically until the barrier width reaches 40 bilayers. Yet, over the 40 bilayers of the barrier

Table 6.1: Calculated effective mass for hole of the 7 different SiC polytypes. The corresponding channel distances, channel length, and band gap are also listed.

polytypes	channel length	Barrier width L	effective mass (ab-plane)	effective mass (c-axis)	band gap (eV)
$5H$ (ABCAB)	5	0	1.662	1.687	1.888
$7H$ (ABCABAB)	5	2	2.007	1.959	1.852
$9H$ (ABCABABAB)	5	4	2.255	2.923	1.815
$11H$ (ABCABABABAB)	5	6	2.357	5.237	1.802
$13H$ (ABCABABABABAB)	5	8	2.391	11.701	1.780
$15H$ (ABCABABABABABAB)	5	10	2.389	29.532	1.764
$17H$ (ABCABABABABABABAB)	5	12	2.384	76.626	1.747

width, the band gaps are constant, 1.206 eV.

6.2 Spontaneous polarization effects on effective mass of hole

The effects of the spontaneous polarization on the electronic structure is not limited to the band-gap. We have found that the effective mass of the hole in SiC-polytypes is also considerably affected by the spontaneous polarization. Fig. 6.3 in the above section also shows the KS orbitals of the valence-band top (VBT). For the $8H$ polytype, the KS orbital at the VBT is delocalized in the system. In contrast, the corresponding orbital in the $20H$ polytype is localized at the interface between the channel region and barrier region, because of the slanted band lineup due to the spontaneous polarization. We have investigated the effective masses of holes with increasing the barrier width.

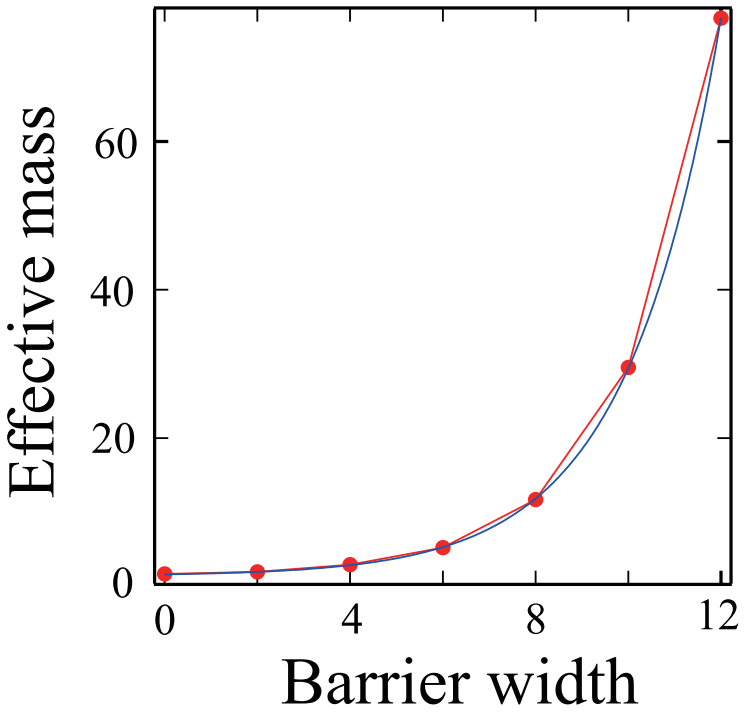

Figure 6.6: Calculated effective masses of the valence-band top (VBT) along the *c*-axis as a function of barrier widths.

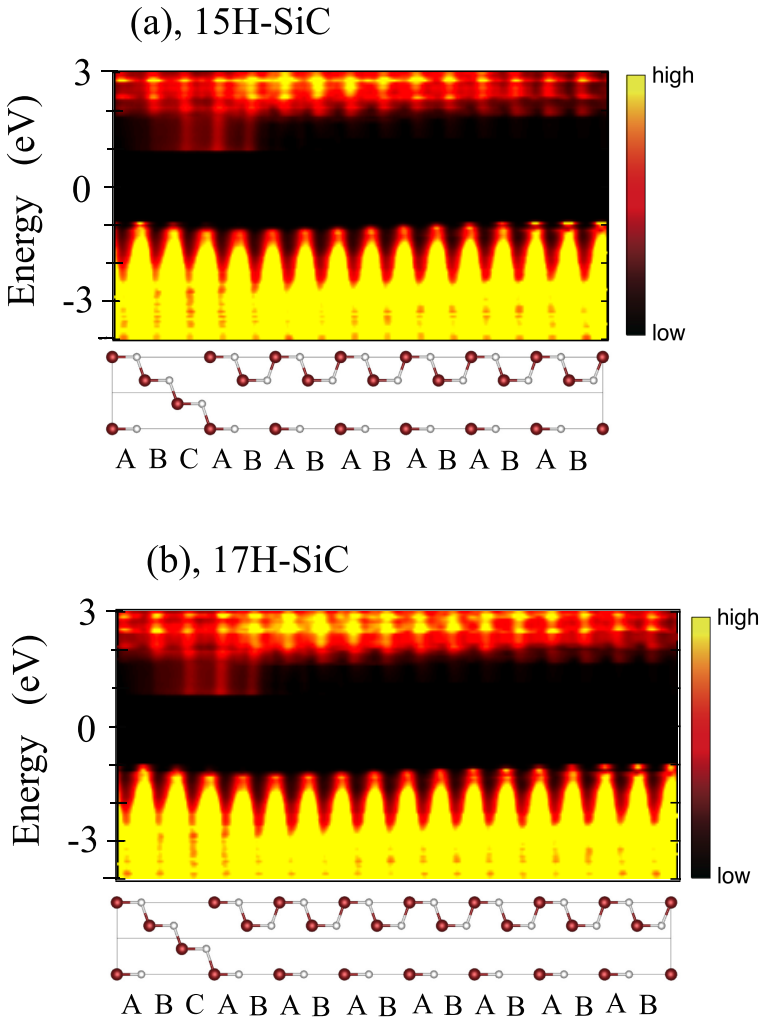

Figure 6.7: Contour plots of the calculated local density of states (LDOS) $D(\varepsilon, z)$ for the 15H (ABCABABABABABAB) polytype (a) and the 17H (ABCABABABABABABAB) polytype (b) listed in Table 6.1. Horizontal direction is the stacking direction (c-axis) and corresponds to z coordinate.

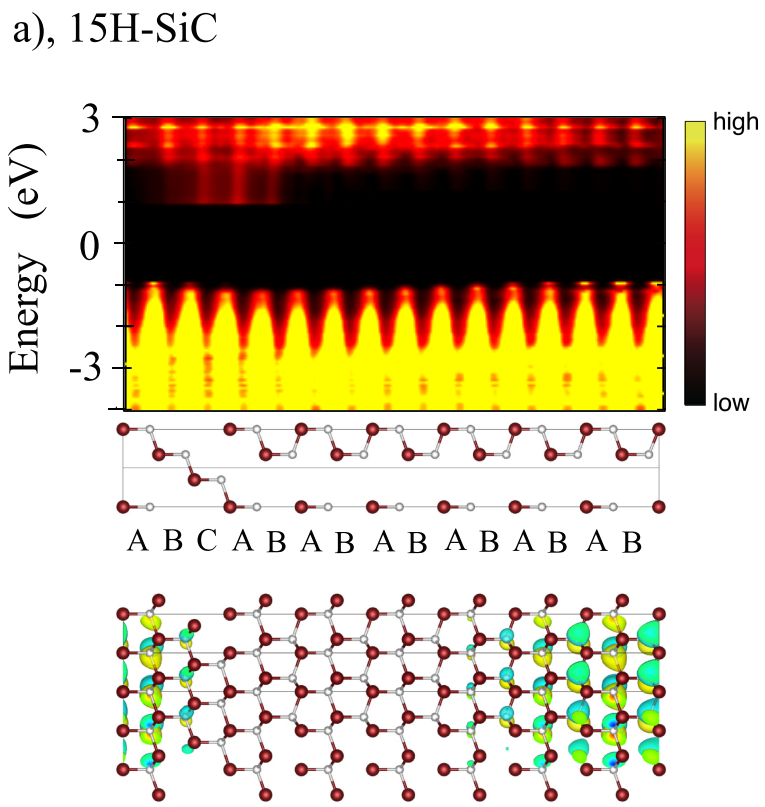

Figure 6.8: Contour plots of the calculated local density of states (LDOS) $D(\varepsilon, z)$ for the $15H$ (ABCABABABABABAB) polytype listed in Table 6.1. Horizontal direction is the stacking direction (c-axis) and corresponds to z coordinate. Contour plot and isosurface of the 20 % of the maximum values of the Kohn-Sham (KS) orbital at the valence band top (VBT).

We have first investigated the effective masses of holes depending on the barrier width. Table 6.1 shows the calculated effective masses with the channel length fixed at 5 bilayers. Drastic change in effective masses in the a, b-plane is not observed, but the effective masses along the c-axis clearly show exponential increase with increasing the barrier width. Figure. 6.6 shows the effective masses for holes along c-axis. In particular, in the case of the $17H$, the effective masses along the c-axis is 32 times greater than that in a, b-plane. This anisotropy in effective mass apparently comes from the localized KS orbitals of holes. Figures. 6.7 and 6.8 show the calculated LDOS and contour plot of KS orbital at VBT. The orbital is localized at the interface between channel region and barrier region. We have found that spontaneous polarization causes the localization of holes, thus showing anisotropy of effective masses of holes.

7

Summary and Conclusions

7.1 Summary and Conclusions

We have performed electronic-structure calculations within the generalized-gradient approximation (GGA) in the density-functional theory (DFT) to clarify the mechanism of substantial band-gap variation and anisotropy in effective masses depending on polytypes of sp^3-bonded materials. Our GGA calculations clarify that several conduction band states do not distribute near atomic sites but float in the interstitial channels in covalent semiconductors.

We have found that the electrostatic potential in an interstitial channel varies substantially in polytypes, depending on the morphology of the interstitial channel. Therefore, the changes of the channel shape makes a drastic changes of the energy level of the floating states. In compound semiconductors such as AlN, BN, and also SiC, the difference in the electronegativity between the constituent atoms causes particular tetrahedral (T_d) interstitial sites to be energetically favorable. This makes the energy level of the floating state distributing solely around the particular T_d sites shift downwards. Such distribution is possible in the $3C$ polytype. This explains the observed substantial band-gap decrease in the $3C$ polytypes of the compound semiconductors. In contrast, for elementary semiconductor such as diamond, such difference in elsctronegativity is absent. Instead, in the $2H$ polytypes the number of neighbor atoms around the interstitial sites is large compared with other polytypes. This causes the band-gap decrease in the $2H$ polytype, in accord with the experiment.

We have clarified that the appearance of the floating states unrecognized in the past

are related to the following two factors: The low packing efficiency in sp^3-bonded materials, and the non-spherical-charge distribution. The appearance of the floating states is a consequence of the existence of the internal space, and the low packing efficiency is therefore advantageous for floating states. We have found that non-shperical-charge distribution makes the potential in the interstitial channels lower substantially than the vacuum level. For these reasons, floating states are ubiquitous in sp^3-bonded materials.

Next, we have investigated the capability of the linear-combination-of-atomic-orbital (LCAO) calculations in describing the floating nature. We have found that the description of the floating nature with atomic orbitals is quite difficult. It is found that unexpectedly high-energy-atomic orbitals are needed to describe the floating nature, while LCAO calculations reproduce valence bands efficiently. For example, floating nature in SiC can not be seen in the LCAO calculations using the minimum basis set: $3s$ and $3p$ of Si, and $2s$ and $2p$ of C. Furthermore, including Si-$3d$ atomic orbital as a basis set in LCAO calculation is still insufficient to describe the floating nature. Therefore, we have shown that the floating nature is difficult to describe in conventional LCAO picture.

We have also investigated the validity of the "hexagonality" to describe the band-gap variation in SiC polytypes. The substantial band-gap variation has been analyzed by an empirical parameter hexagonality for a half century. Yet, we have clarified that the parameter hexagonality is misleading. Instead, we have found that a new quantity "channel length" is essential in describing the band-gap variation. The channel length has a clear physical meaning: This represents the spatial extension of the floating state. It is clearly seen that the smaller the channel length is, the energy level of the conduction-band minimum shift higher due to the electron confinement.

We have found a clear relation between floating states and the anisotropy in the effective mass of the electron. When channel lengths are finite, floating states distribute or are localized in the finite region of the channels. Then, it is clearly seen that effective mass along the direction from one channel region to another increases exponentially with the distance between the two channel regions being larger. We have found the shapes of channels are decisive in determining the anisotropy in the effective mass of electrons substantially.

We have clarified the spontaneous polarization effects on the band gap in SiC polytypes. Calculated local density of states (LDOS) unequivocally reveals substantial

effects of spontaneous polarization in the hexagonal polytypes: The polarization in the hexagonal region renders the band lineup slanted in real space along the stacking direction, and further the counter polarization in the cubic region makes it slanted in the reverse direction. We have found that the slanted band lineup causes downward (upward) shift of the conduction (valence) band edge and the band gap becomes narrower. In addition, the slanted band lineup makes the wave function of the hole localized at the interface between the channel region and the hexagonal region, thus showing anisotropy of effective mass.

7.2 Possibility of observation

In this section, we discuss how to verify the existence of the floating states directly and indirectly in experiments. We have found that the existence of the floating states at the conduction-band minima in sp^3-bonded materials plays important roles in the band-gap variation in polytypes. Therefore, the band-gap variation in polytypes is one of the verifications for the existence of such peculiar electron states. In addition, if the exponential increase of electron-effective masses, mentioned in Sec. 5.2, is observed experimentally, the existence of the floating states is reinforced.

However, the above experimental measurements are indirect techniques. Here, we discuss another perspective of the direct observation of the floating states by experiments. We first focus on the experimental technique by using positron annihilation for investigating floating nature. The positron is the antiparticle or the antimatter counterpart of the electron. The positron has an electric charge of +1e, a spin of 1/2, and has the same mass as an electron. When a positron collides with an electron, annihilation occurs, resulting in the production of two γ-ray photons (electronpositron annihilation). By detecting the energy spectrum of the γ-ray, we can estimate the momentum of the electron and the lifetime of the positron.The lifetime of the positron is a quantity related to the electron density at the position where the annihilation occurs. Larger the electron density is, more often the electron-positron annihilation occurs, thus showing shorter lifetime of the positron. In addition, the positron has a positive charge, and distributes mainly in interstitial sites, because the nuclei have large positive charge. Therefore, electron-positron annihilation is one of the most efficient techniques to measure the electron density at the interstitial space.

7. SUMMARY AND CONCLUSIONS

We propose, here, that an electron-positron-annihilation measurement in electron-doped SiC reveals floating nature of the conduction-band minimum. In particular, we predict that comparative study of electron-positron-annihilation measurement for the intrinsic and electron-doped SiC clearly shows the floating electron nature.

Bibliography

[1] Y. M. Tairov and V. F. Tsvetkov, J. Cryst. Growth, **43** 209 (1978).

[2] N. Kuroda, K. Shibahara, W.S. Yoo, S. Nishino, and H. Matsunami, Ext. Abstr. of the 19th Conf. on Solid State Devices and Materials, Tokyo, 227 (1987).

[3] H. Matsunami and T. Kimoto, Mat. Sci. and Eng. R**20**, 125 (1997).

[4] D. Nakamura, I. Gunjishima, S. Yamaguchi, T. Ito, A. Okamoto, H. Kondo, S. Onda and K. Takatori, Nature, **430**, 1009 (2004).

[5] W. A. Harrison, *ElectronicStructureandPropertiesofSolids*, Dover Pub., Inc, New York (1989), p. 176.

[6] W. von Muench, and I. Pfaffeneder, J. Appl. Phys., **48**, 4831 (1977).

[7] D.W. Feldman, J.H. Parker Jr., W.J. Choyke, L. Patrick, Phys. Rev., **173**, 787 (1968).

[8] W. von Muench, E. Pettenpaul, J. Appl. Phys., **48**, 4823 (1977).

[9] G.A. Slack, J. Appl. Phys., **35**, 3460 (1964).

[10] A. R. Verma and Krishna, Polymorphism and Polytypism in Crystals (Wiley, New York, 1966).

[11] Yu. M. Tairov and V. F. Tsvetkov, J. Cryst. Growth **43**, 209 (1976).

[12] D. Nakamura, I. Gunjishima, S. Yamaguchi, T. Ito, A. Okamoto, H. Kondo, S.Onda, and K. Takatori, Nature **430**, 1009 (2004).

[13] Yu. M. Tairov and V. F. Tsvetkov, J. Cryst. Growth **52**, 146 (1981).

[14] S. Nishizawa and M. Pons, Microelectronic Engineering **83**, 100 (2006).

[15] K. Kojima, S. Nishizawa, S. Kuroda, H. Okumura, and K. Arai, J. Cryst. Growth **275**, e549 (2005).

[16] G. Wellenhofer and U. Rossler, Phys. Stat. Sol. (b) **202**, 107 (1997).

[17] B. Wenzien, P. Kackell, and F. Bechstedt, Phys. Rev. B, **52**, 10897 (1995).

[18] W. J. Schaffer, G.H. Negley, K. G. Irvine, and J. W. Palmour, Mat. Res. Soc. Proc., **339**, 595 (1994).

[19] R. G. Humphreys, D. Bimberg, and W. J. Choyke, Solid State Comm., **39**, 163 (1981).

[20] L. Patrick, D. R. Hamilton, and W. J. Choyke, Phys. Rev. **143**, 526 (1966).

[21] W.J. Choyke, D. R. Hamilton, L. Patrick, Phys. Rev. **133**, A1163 (1964).

[22] G. N. Violina, Sov. Phys.-Solid State **5**, 2500 (1964).

[23] G. A. Lomakina and Y. A. Vodakov, Sov. Phys.-Solid State**15**, 83 (1973).

[24] B. W. Wessels and J. C. Gatos, J. Phys. Chem. Solid, **38**, 345 (1977).

[25] L. S. Aivazova, Sov. Phys.-Semicond., **11**, 1069 (1978).

[26] B. Ellis and T. S. Moss, Proc. R. Soc. Lond A, **299**, 383 (1967).

[27] P. J. Dean, J. Lum., **15**, 299 (1977).

[28] R. Kaplan, Solid State Commun., **55**, 67 (1985).

[29] N. T. Son, O. Kordina, A. O. Konstantinov, W. M. Chen, E. Sorman, B. Monemar, and E. Janzen, Appl. Phys. Lett., **65**, 3209 (1994).

[30] M. A. Il'in, Sov. Phys.-Solid State, **13**, 2078 (1972).

[31] S. A. Geidur, Sov. Phys.-Solid State, **20**, 1654 (1978).

[32] J.-C. Charlier, X. Gonze and J.-P. Michenaud, Phys. Rev. B. **43**, 4579 (1991).

[33] M. Posternak, A. Baldereschi, A. J. Freeman, E. Wimmer, and M. Weinert, Phys. Rev. Lett. **50**, 761 (1983).

[34] S. Okada, A. Oshiyama, and S. Saito, Phys. Rev. B **62**, 7634 (2000).

[35] M. Posternak, A. Baldereschi, A. J. Freeman, and E. Wimmer, Phys. Rev. Lett. **52**, 863 (1984).

[36] Th. Fauster, F. J. Himpsel, J. E. Fischer, and E. W. Plummer, Phys. Rev. Lett. **51**, 430 (1983).

[37] A. Oshiyama and S. Okada, *The Oxford Handbook of Nanoscience and Technology* edited by A. V. Narlikar and Y. Y. Fu (Oxford University Press, 2010) vol. II, pp94.

[38] S. Saito and A. Oshiyama, Phys. Rev. Lett. **71**, 121 (1993).

[39] Y. Miyamoto, A. Rubio, X. Blase, M. L. Cohen, and S. G. Louie, Phys. Rev. Lett. **74**, 2993 (1995).

[40] W. Kohn and L. J. Sham, Phys. Rev. **140**, A1133 (1965).

[41] P. Hohenberg and W. Kohn, Phys. Rev. **136**, B864 (1964).

[42] J. E. Harriman, Phys. Rev. A, **24**, 680 (1981).

[43] Gilbert, Phys. Rev. B, **12**, 2111 (1975).

[44] J. Perdew and A. Zunger, Phys. Rev. B, **23** 5048 (1981).

[45] D. C. Langreth and M. J. Mehl, Phys. Rev. B, **28**, 1809 (1983).

[46] D. M. Ceperley and B. J. Alder, Phys. Rev. Lett., **45** 566 (1980).

[47] J. P. Perdew, K. Burke and M. Ernzerhof, Phys. Rev. Lett. **77**, 3865; *ibid.* **78**, 1396(E) (1997).

[48] J. P. Perdew, M. Ernzerhof and K. Burke, J. Chem. Phys. **105**, 9982 (1996).

[49] N. Troullier and J. L. Martins, Phys. Rev. B **43**, 1993 (1991).

[50] V. Heine, Solid State Phys. **24**, 1(1970).

[51] D. R. Hamann, M. Schluter and C. Chiang, Phys. Rev. Lett., **43**, 1494 (1979).

[52] G. B. Bachelet, D. R. Hamann, and M. Schluter, Phys. Rev. B, **26**, 4199 (1982).

[53] J. P. Perdew and A. Zunger, Phys. Rev. B**23**, 5048 (1981).

[54] A. J. Cohen, P. Mori-Sánchez, W. Yang, Science **321**, 721 (2008).

[55] O. A. Vydrov and G. E. Scuseria, J. Chem. Phys. **121**, 8187 (2004).

[56] A. Ruzsinszky, J. P. Perdew, G. I. Csonka, O. A. Vydrov, and G. E. Scuseria, J. Chem. Phys. **125**, 194112 (2006).

[57] A. Ruzsinszky, J. P. Perdew, G. I. Csonka, O. A. Vydrov, and G. E. Scuseria, J. Chem. Phys. **126**, 104102 (2007).

[58] J. P. Perdew, A. Ruzsinszky, G. I. Csonka, O. A. Vydrov, G. E. Scuseria, V. N. Staroverov, and J. Tao, Phys. Rev. A **76**, 040501 (2007).

[59] J. P. Perdew, R. G. Parr, M. Levy and J. L Balduz Jr., Phys. Rev. Lett. **49**, 1691 (1982).

[60] J. P. Perdew, M. Levy, Phys. Rev. Lett. **51**, 1884 (1983).

[61] L. J. Sham and M. Schlüter, Phys. Rev. Lett. **51**, 1888 (1983).

[62] L. J. Sham and M. Schlüter, Phys. Rev. B**32**, 3883 (1985).

[63] J. F. Janak, Phys. rev. B**18**, 7165 (1978).

[64] P. Mori-Sánchez, A. J. Cohen and W. Yang, Phys. Rev. Lett. **100**, 146401 (2008).

[65] A. J. Cohen, P. Mori-Sánchez and W. Yang, Phys. Rev. B **77**, 115123 (2008).

[66] J. Heyd, G. E. Scuseria, and M. Ernzerhof, J. Chem. Phys. **118**, 8207 (2003).

[67] H. Stoll and A. Savin, *Density Functional Methods in Physics* (Plenum, New York, 1985), pp. 177.

[68] H. Iikura, T. Tsuneda, T. Yanai, and K. Hirao, J. Chem. Phys. **115**, 3540 (2001).

[69] Y. -i. Matsushita, K. Nakamura, and A. Oshiyama, Phys. Rev. B **84**, 075205 (2011).

[70] O. Sugino and A. Oshiyama, Phys. Rev. Lett. **68**, 1858 (1992).

[71] J. Yamauchi, M. Tsukada, S. Watanabe and O. Sugino, Phys. Rev. B **54**, 5586 (1996).

[72] H. Kageshima and K. Shiraishi, Phys. Rev. B **56**, 14985 (1997).

[73] T. Ozaki, Phys. Rev. B **67**, 155108 (2003).

[74] T. Ozaki, and H. Kino, Phys. Rev. B **69**, 195113 (2004).

[75] H. Schulz and K. H. Thiemann, Solid State Commun. **32**, 783 (1979).

[76] *Physics of Group IV and III-V Compounds*, ed. O. Madelung, M. Schulz, and M. Weiss (Springer-Verlag, Berlin, 1982) LandoltBornstein, New Series, Group III, Vol. 17, Part A.

[77] A. H. Gomes de Mesquita, Acta Crystallogr. **23**, 610 (1967).

[78] H. Schulz and K. H. Thiemann, Solid State Commun. **23**, 815 (1977).

[79] *Properties of Group III Nitrides*, ed. J. H. Edgar (IEE, London, 1994) EMIS Datareviews Series.

[80] O. Mishima and K. Era: in *Electric Refractory Materials*, ed. Y. Kumashiro (Marcel Dekker, New York, 2000) pp. 495-556, and references therein.

[81] S. Komatsu, K. Kobayashi, et. al., J. Phys. Chem. C, **114**, 13176 (2010).

[82] H. P. Maruska, and J. J. Tietjen, Appl. Phys. Lett., **15**, 327 (1969).

[83] I. Vurgaftman, J. R. Meyer, and L. R. Ram-Mohan, J. Appl. Phys.**89**, 5815 (2001).

[84] M. S. Hybertsen and S. G. Louie, Phys. Rev. B **34**, 5390 (1986).

[85] F. Aryasetiawan and O. Gunnarsson, Rep. Prog. Phys. **61**, 237 (1998).

[86] For discussion on several ambiguities in the GW approximation, see M. L. Tiago, S. Ismail-Beigi and S. G. Louie, Phys. Rev. B **69**, 125212 (2004); M. van Schilfgaarde, T. Kotani and S.V. Faleev, Phys. Rev. B **74**, 245125 (2006), and references therein.

[87] J. Heyd and G. E. Scuseria, J. Chem. Phys. **120**, 7274 (2004).

[88] J. Heyd and G. E. Scuseria, J. Chem. Phys. **121**, 1187 (2004).

[89] J. Heyd, G. E. Scuseria and M. Ernzerhof, J. Chem. Phys. **124**, 219906 (2006).

[90] J. Heyd, J. E. Peralta, G. E. Scuseria, and R. L. Martin, J. Chem. Phys. **123**, 174101 (2005).

[91] J. Heyd and G. E. Scuseria, J. Chem. Phys. **121**, 1187 (2004).

[92] For a review, *Properties of Silicon Carbide*, edited by G. L. Harris (INSPEC, London, 1995).

[93] H. Yamashita, K. Fukui, S. Misawa, and S. Yoshida, J. Appl. Phys.**50**, 896 (1979).

[94] P. T. Margarita, W. A. Gregory, S. Z. Tsvetanka, A. J. Kenneth, J. S. Steven, and J. N. Hilfiker, J. Appl. Phys.**89**, 3331 (2001).

[95] R. M. Chrenko, Solid State Comm., **14**, 511 (1974).

[96] N. Troullier and J.L. Martins, Phys. Rev. B **43**, 1993 (1991).

[97] M. Bhatnagar and B. J. Baliga, *IEEE Trans. Electron Devices* ED-40, 545 (1993).

[98] W. J. Choyke et al., Silicon Carbide I, II, Akademie Verlag (1997).

[99] W. J. Choyke et al., Silicon Carbide-Recent Major Advances, Springer (2003).

[100] H. Amano, et al., Jpn. J. Appl. Phys. **28**, L2112 (1989).

[101] J. A. Van Vechten et al., Jpn. J. Appl. Phys. **31**, 3662 (1992).

[102] O. Madelung ed., Data in Science and Technology, Semiconductors, Group IV Elements and III-V Compounds (Springer-Verlag, Berlin, 1991).

[103] W. J. Choyke, H. Matsunami and G. Pensl, eds., Silicon Carbide, A Review of Fundamental Questions and Applications to Current Device Technology, Vol. I & II (Akademie Verlag, Berlin, 1997).

[104] S. Nakamura et al., Jpn. J. Appl. Phys. **31**, 1258 (1992).

[105] S. Furuya, Y. -i. Matsushita, and A. Oshiyama, Phys. Rev. B

[106] Y. -i. Matsushita, S. Furuya, and A. Oshiyama, Phys. Rev. Lett. **108**, 246404 (2012).

[107] Landolt-Bornstein, Vol. III, (Springer, New York, 1982)

[108] S. H. Wemple, Phys. Rev. B **2**, 2679 (1970).

[109] S. Adachi, Optical Properties of Crystalline and Amorphous Semiconductors: Numerical Data and Graphical Information (Kluwer Academic, Dordrecht, 1999).

[110] R. T. Poole, J. Liesegang, R. C. G. Leckey, and J. G. Jenkin, Phys. Rev. B **11**, 5190 (1975).

[111] R. J. Magyar, A. Fleszar and E. K. U. Gross, Phys. Rev. B **69**, 045111 (2004).

[112] M. Rohlfing and S. G. Louie, Phys. Rev. B **62**, 4927 (2000).

[113] A. L. Wachs, T. Miller, T. C. Hsieh, A. P. Shapiro, T. C. Chiang, Phys. Rev. B **32**, 2326 (1985).

[114] F. R. McFeely et al., Phys. Rev. B **9**, 5268 (1974).

[115] F. J. Himpsel, J. F. van der Veen and D. E. Eastman, Phys. Rev. B **22**, 1967 (1980).

[116] S. Piskunov, , a, E. Heifetsb, R. I. Eglitisa and G. Borstel, Compt. Mater. Sci. **29**, 165 (2004).

[117] K.H. Hellwege and A.M. Hellwege, Editors, Ferroelectrics and Related SubstancesNew Series vol. 3, Landolt-Bornstein, Springer Verlag, Berlin (1969) group III .

[118] P. Varotsos, K. Alexopoulos, Phys. Rev. B **15**, 4111 (1977).

[119] A. R. Jivani, P. N. Gajjar, and A.R. Jani, Semicond. Phys, Quantum. bf 5, 243 (2002).

[120] H. Yorikawa J. Elec. Spectro. Ph. **184**, 379 (2011).

[121] For a review, *PropertiesofSiliconCarbide*, edited by G. L. Harris (INSPEC, London, 1995).

[122] J. P. Perdew, K. Burke, and M. Ernzerhof, Phys. Rev. Lett. **77**, 3865 (1996).

[123] P. Hohenberg and W. Kohn, Phys. Rev. **136**, B864 (1964); W. Kohn and L. J. Sham, Phys. Rev. **140**, A1133 (1965).

[124] L. Kleinman and D.M. Bylander, Phys. Rev. Lett. **48**, 1425 (1982).

[125] Y. -i. Matsushita, S. Furuya, and A. Oshiyama, Phys. Rev. Lett. **108**, 246404 (2012).

[126] Y. -i. Matsushita, K. Nakamura, and A. Oshiyama, Phys. Rev. B **84**, 075205 (2011).

[127] J. E. Iglesias, Acta Crystallogr. A **62**, 178 (2006).

[128] K. Kobayashi, and S. Komatsu, J. Phys. Soc. Jpn., **81**, 024714 (2012).

[129] W. Saito, I. Omura, T. Ogura, and H. Ohashi, Solid State Electron., **48**, 1555 (2004).

[130] J. Pelletier, D. Gervais, and C. Pomot, J. Appl. Phys. **55**, 994 (1984).

[131] N. Lifshitz, A. Jayaraman, R. A. Logan, and H. C. Card, Phys. Rev. B, **21**, 670 (1980).